UC Merced
UC Merced Electronic Theses and Dissertations

Title

True Atomic-Resolution Imaging under Ambient Conditions via Conductive Atomic Force Microscopy

Permalink

https://escholarship.org/uc/item/0195t10c

Author

Sumaiya, Saima Aktar

Publication Date

2022

Peer reviewed|Thesis/dissertation

eScholarship.org Powered by the California Digital Library
University of California

True Atomic-Resolution Imaging under Ambient Conditions via Conductive Atomic Force Microscopy

by

Saima Aktar Sumaiya

A dissertation submitted in partial satisfaction of the

requirements for the degree of

Doctor of Philosophy

in

Mechanical Engineering

in the

Graduate Division

of the

University of California, Merced

Committee in charge:

Professor Roberto C. Andresen Eguiluz, Chair
Professor Ashlie Martini
Professor Min Hwan Lee
Professor Mehmet Z. Baykara

Fall 2022

Portion of Chapter 2 © 2022 ACS Publications

Portion of Chapter 3 © 2022 ACS Publications

Portion of Chapter 4 © 2022 ACS Publications

Portion of Chapter 5 © 2022 ACS Publications

All other chapters

© Saima Aktar Sumaiya, 2022

All rights are reserved.

The dissertation of Saima Aktar Sumaiya, titled True Atomic-Resolution Imaging under Ambient Conditions via Conductive Atomic Force Microscopy, is approved and it is acceptable in quality and form for publication on microfilm and electronically:

Professor Mehmet Z. Baykara	Date
Professor Ashlie Martini	Date
Professor Min Hwan Lee	Date
Professor Roberto C. Andresen Eguiluz, Chair	Date

University of California, Merced
2022

To Monomonjil, the place that I have called home for more than half of my life

Contents

Contents ii

List of Figures iv

1 Introduction 1
1.1 Scanning Tunneling Microscopy . . . 2
1.2 Atomic Force Microscopy . . . 6
1.3 Research Objectives . . . 12
1.4 Thesis Outline . . . 14
1.5 References . . . 16

2 Demonstration of True Atomic-Resolution Surface Imaging under Ambient Conditions 19
2.1 Conductive Atomic Force Microscopy . . . 19
2.2 History of Atomic Resolution Imaging via C-AFM . . . 21
2.3 Methods . . . 23
2.4 Demonstration of True Atomic-Resolution Surface Imaging . . . 24
2.5 Effect of Different Tip Materials . . . 27
2.6 Speed Dependence . . . 27
2.7 Load Dependence . . . 29
2.8 Effect of Applied Bias . . . 32
2.9 Robustness and Repeatability . . . 32
2.10 Potential Mechanisms of True Atomic-Resolution Imaging . . . 34
2.11 Conclusions . . . 39
2.12 References . . . 40

3 Imaging Surfaces of Different Materials under Ambient Conditions with Atomic Resolution 43
3.1 Introduction . . . 43
3.2 Two-Dimensional Transition Metal Dichalcogenide Semiconductors . 44
3.3 Two-Dimensional Elemental Semiconductor . . . 46

3.4 Two-Dimensional Semimetal 47
3.5 Metal 50
3.6 Conclusions 53
3.7 References 54

4 Atomically-Resolved Defects and Disorder 58
4.1 Introduction 58
4.2 A Variety of Defects on Different TMD Surfaces 59
4.3 Charge State Manipulation 61
4.4 Imaging Disorder on HOPG 63
4.5 Conclusions 66
4.6 References 67

5 Atomically-Resolved Study of Thin Crystals of a Transition Metal Carbide (MXene): α–Mo_2C 69
5.1 Introduction 69
5.2 Thin Crystals of CVD-Grown α–Mo_2C 69
5.3 Atomically-Resolved Structure of α–Mo_2C 71
5.4 Imaging A Variety of Defects on α–Mo_2C 74
5.5 Room Temperature Charge Ordering on α–Mo_2C 78
5.6 Conclusions 80
5.7 References 81

6 Summary and Future Prospects 83
6.1 References 85

List of Figures

1.1 Schematic describing the operating principle of a typical STM. 3
1.2 Seminal results obtained via STM: (a) First atomic resolution STM image revealing the 7 × 7 reconstruction of Si(111) surface. (b) 48 Fe atoms are arranged on Cu(111) surface resulting in confinement of electrons. (c) Atomic resolution STM image of a cleaved 2H-TaS_2 surface with a single atom vacancy in the highlighted region. Images (a), (b), and (c) taken from Ref. [8], [11], and [12], respectively. 5
1.3 Schematic describing the operating principle of a typical AFM. 7
1.4 Schematic of tip-sample interaction force (F) as a function of separation distance (s). 9
1.5 Different operational modes of AFM: (a) contact mode, (b) intermittent contact (*i.e.* tapping) mode and (c) non-contact mode. 9
1.6 (a) Atomically sharp tip before contact is established with the surface. (b) Tip apex losing sharpness after contact is established with the surface. . 10
1.7 Seminal results obtained via NC-AFM: (a) NC-AFM topographic image of a Sn/Si alloy surface distinguishing atoms of different chemical identity. (b) Constant height AFM image of pentacene acquired with a tip functionalized with CO at the apex. (c) Ball and stick model of the pentacene molecule imaged in (b). Image (a) is taken from Ref. [27], and images (b) and (c) are taken from Ref. [28] 13
1.8 Challenges of NC-AFM imaging under ambient conditions: tip can be oscillating (a) above or (b) within the contamination layer on surface, leading to complications for atomic-resolution measurements. 13

2.1 Schematic describing the operation of a typical C-AFM set-up. 20
2.2 High resolution conductivity mapping through contact microscopy as opposed to STM under controlled environments. (a) Lattice resolution current map obtained on HOPG via PCM under UHV. (b) High resolution current map obtained on TiO_2 via C-AFM under UHV. (c) Atomic-resolution current map obtained on WS_2 via C-AFM under inert N_2 environment with a S vacancy indicated by the white arrow. Images (a), (b), and (c) taken from Refs. [17], [18], and, [19] respectively. 22

2.3 Schematic of the sample configuration used for C-AFM measurements on TMD samples. 24
2.4 A representative force-distance (F-z) curve obtained with a conductive diamond coated tip on HOPG. The curve yields a snap-in force of ~1.5 nN. 25
2.5 Resolving the true crystal structure of HOPG under ambient conditions via C-AFM. (a) Atomic model of the HOPG (0001) surface with red and blue spheres representing two types of carbon atoms, and the gray spheres representing carbon atoms in the layer below. (b) Current image obtained on HOPG showing three types of atomic sites characterized by low, high, and intermediate current (see the corresponding green, pink, and blue circles, respectively). The simultaneously recorded topography map (height range: 0–3.1 Å is shown in the inset, exhibiting no atomic-scale features.The current image was obtained with an applied normal load of 0.0 nN and at a scanning frequency of 15.62 Hz. Bias voltages: (b) 0.04 V. 26
2.6 Demonstration of true atomic-resolution imaging under ambient conditions via C-AFM. (a) Atomic model of the MoS_2 (001) surface. (b) Current image obtained on MoS_2 showing well-defined protrusions separated by ~3.2 Å. The simultaneously obtained topography map, with a stripe-like pattern, is shown in the inset (height range: 0–6.8 Å). (c) Current image obtained on MoS_2 showing multiple atomic-scale defects. The simultaneously obtained topography map is shown in the inset, with no trace of the defects (height range: 0–3.4 Å). (d) Current image obtained on MoS_2 exhibiting three types of atomic sites characterized by low, high, and intermediate current (see the corresponding green, purple, and pink circles, respectively). This image clearly captures a single atomic defect, as indicated by the white arrow. The corresponding topography map is shown in the inset (height range: 0–5.4 Å). All images were obtained with an applied normal load of 0.0 nN and at a scanning frequency of 15.62 Hz. Bias voltages: (b) 0.1 V; (c) 1.8 V; (d) -1.2 V. 28
2.7 Effect of different tip materials on C-AFM imaging. (a) Representative current image obtained on HOPG with a PtSi tip. This image features a periodicity of ~2.5 Å, indicating that it is not a true atomic-resolution image; it rather represents lattice resolution. (b) Representative current image obtained on MoS_2 with a Ti/Ir coated tip. Even though this image features atomic resolution, we typically do not observe true atomic resolution with this category of tip in a robust and reproducible manner. All images were obtained with an applied normal load of 0.0 nN, and at a scanning frequency of 15.62 Hz. Bias voltages: (a) 1.5 V, (b) 2.5 V. . . . 29

2.8 Speed dependence of atomic-resolution C-AFM imaging, with decreasing scanning speed. A series of images recorded on MoS_2 with decreasing scanning frequency (from 15.62 Hz to 0.50 Hz) showing a degradation in spatial resolution. 30
2.9 Speed dependence of atomic-resolution C-AFM imaging, with increasing scanning speed. A series of images obtained on MoS_2 with the same conductive tip used in Fig. 2.8, with increasing scanning frequency (from 0.25 Hz to 15.62 Hz), showing that atomic resolution emerges at higher scanning speeds. 31
2.10 Load dependence of atomic-resolution C-AFM imaging. A series of images recorded on MoS_2 where the applied normal load varied from 0 to 60 nN during scanning. These images show that the capability of atomic-resolution imaging via C-AFM is not lost due to changes in normal load at the tip-sample junction. 33
2.11 Reproducibility of defect imaging. (a) Current image obtained on MoS_2 featuring two extended defects. (b) Current image obtained upon continuous/repeated imaging of the same area shown in (a). The defect structures in both (a) and (b) appear similar, despite the presence of noticeable thermal drift. There were 15 images recorded between (a) and (b) by way of continuous scanning, corresponding to $\sim$4.3 minutes. All images were obtained with an applied normal load of 0.0 nN, and at a scanning frequency of 15.62 Hz. Bias voltages: (a) -1.2 V, (b) -1.2 V. 34
2.12 Schematic showing the discrepancy between the physical and electrical contact formed between the tip and the sample, as one of the possible explanations that can enable atomic-resolution C-AFM imaging. 35
2.13 Schematic of models used to estimate physical and electrical contact areas. (a) A schematic showing the difference between the Hertz and DMT contact mechanics models. As opposed to the Hertz model, the DMT model takes into account the adhesion between the surfaces. (b) A schematic of the Sharvin model used to estimate electrical contact area for ballistic electron transport. 36

2.14 Discrepancy between physical and electrical contact areas at the tip-sample junction. (a) A representative force-distance (F-z) curve obtained with a conductive diamond tip on HOPG. The curve yields an adhesion force of ~9.0 nN, which was plugged into the DMT contact model to estimate the physical contact radius between the tip and HOPG sample. (b) A histogram showing the distribution of the estimated physical contact radius between the tip and the HOPG sample, utilizing 189 F-d curves. (c) A representative current vs. voltage (I-V) curve (solid blue) recorded with a conductive diamond tip on HOPG. The slope of the I-V curve was extracted by a linear fit (dotted orange) of the data. (d) A histogram showing the distribution of electrical contact radius formed between the conductive diamond tip and HOPG, calculated from 1076 I-V curves using Sharvin's equation. 37
2.15 Schematic showing tunneling happening through hydrodynamic lift between tip and sample at high speed scanning, as another potential explanation behind atomic-resolution imaging capability of C-AFM. 38

3.1 (a) Atomic model of the WSe_2 (001) surface. (b) Current image recorded on WSe_2 via C-AFM under ambient conditions showing the atomic-scale crystal structure. (c) The Fourier Transform (FT) of the current map shown in (b) that corresponds to an average periodicity of 3.2 Å. 46
3.2 (a) Atomic model of the WS_2 (001) surface. (b) Current image recorded on WS_2 via C-AFM under ambient conditions showing the atomic level crystal structure. (c) The FT of the current map in (b) that corresponds to an average periodicity of 3.1 Å. 48
3.3 (a) Atomic model of the black phosphorus (BP) (001) surface. (b) Isometric projection of the puckered crystal structure of BP. (c) Current image recorded on BP via C-AFM under N_2 flow that was initiated after the sample was inserted inside the AFM chamber, following the exfoliation in air. The current image shows alternate columns of crests and troughs in the form of current maxima and minima. Two defective regions, at the edges of the image, are also observed. (d) The corresponding FT of the current map shown in (c). The periodicities calculated from the FT verify that the current map captures the atomic arrangement of the top most phosphorus atoms of the puckered BP lattice as represented by the dark blue spheres in the atomic models (a) and (b). 49
3.4 (a) Atomic model of the $PtSe_2$ (001) surface. (b) Current image recorded on $PtSe_2$ via C-AFM under ambient conditions showing the atomic-scale crystal structure. (c) The FT of the current map in (b) that corresponds to an average periodicity of 3.5 Å. 50

3.5 (a) A micron-scale topographic image recorded on the Au(111) surface showing the rough and grainy structure of the surface. The root mean square (RMS) roughness of the area highlighted by the blue rectangle is ∼6 Å. (b) Line profile drawn along the direction A shown in (a) by blue arrow. The cyan arrows point towards accumulation of contamination on the Au(111) surface upon extended exposure to ambient conditions. . . . 51
3.6 (a) Atomic model of the Au(111) surface.(b) Current image recorded on Au via C-AFM under ambient conditions showing the atomic level crystal structure. (c) The FT of the current map shown in (b) that corresponds to an average periodicity of 2.8 Å. 51
3.7 (a) A relatively large scale topography map recorded on the Au(111) surface showing stripe-like features. (b) Line profile drawn along the direction A shown in (a). The line profile assigns a height of ∼1 Å to the stripe-like features in (a). (c) The corresponding current map recorded simultaneously with (a). The current map also exhibit similar features as that of (a) but with better resolution. 52

4.1 Imaging of different types of defects on MoS_2 (001) under ambient conditions via C-AFM. (a) Current image featuring dark, concentrated defects (blue arrow) as well as diffuse, large-area bright (pink and white arrows) and dark (green arrow) defects. (b) Enlarged current image on the diffuse defects in (a). (c) Current image exhibiting a faint, atomic-scale dark defect (pink circle) and a regular, atomic- scale dark defect (blue circle). (d) Current image showing an extended defect, with a central, bright region (enhanced conductivity) surrounded by a dark region (attenuated conductivity). All images were obtained with an applied normal load of 0.0 nN and at a scanning frequency of 15.62 Hz. Bias voltages: (a) 1.8 V; (b) 1.8 V; (c) 0.7 V; (d) 0.9 V. 60
4.2 Imaging defects on different TMDs.(a) Current image recorded on WSe_2, a 2D TMD semiconductor, showing a diffuse bright defect overlaid on a continuous atomic lattice. (b) Current image recorded on WS_2, another 2D TMD semiconductor, showing a single top surface S vacancy (white arrow). (c) Current image recorded on $PtSe_2$, a 2D TMD semimetal, showing several atomic-scale defects (white arrows) and frequent contrast changes. All images were obtained with an applied normal load of 0.0 nN and at a scanning frequency of 15.62 Hz. Bias voltages: (a) -1.8 V; (b) -1.8 V; (c) -0.014 V. 61

4.3 Electronic manipulation of a defect on MoS_2 via C-AFM under ambient conditions. (a) Large-scale current image showing two defects. (b) Enlarged current image on the defect highlighted by the blue dashed square in (a). The defect features enhanced conductivity compared to its surroundings. (c) I–V curves recorded on top of the defect location marked with the red dot in (b). (d) Current image of area (a) after the I–V sweeps. (e) Current image capturing the same defect in (b) after the I–V sweeps. The defect now features a slightly lower conductivity compared to its surroundings, with the uninterrupted atomic lattice overlaid on top of it. (f–i) Corresponding topographic images for (a), (b), (d), and (e), respectively. All images were obtained with an applied normal load of 0.0 nN and at a scanning speed 15.62 Hz. Bias voltages: (a) -1.0 V; (b) -1.3 V; (d) -0.8 V; (e) -0.8 V. 63
4.4 Reversible manipulation of a defect on MoS_2. (a) Current image recorded on MoS_2 showing a defective area in the form of two halos. (b) I–V curves recorded on top of the defect location marked with the red dot in (a). (c) Current image of area (a) after the I–V sweeps. (d-h) A series of current images showing the gradual re-emergence of the original defect structure. Due to noticeable thermal drift observed between (d) to (f), the area of scanning was adjusted in (g), and then again in (h) to have the defect structure within the imaging frame. All images were obtained with an applied normal load of 0.0 nN and at a scanning speed 15.62 Hz. Bias voltages: (a) -1.2 V; (c-f) -1.2 V; (g) -1.7 V; (h) -1.3 V. 64
4.5 Imaging step-edge of HOPG. (a) Topographic image recorded on a cleaved HOPG surface showing vaguely the presence of a step-edge. (b) Height profile recorded along the arrow A in (a). The height profile shows a height difference of ~8-10 Å. (c) The corresponding current image reveals more details of the step-edge with well-defined boundaries, showing potentially multiple graphite layers torn during the cleaving process. Scanning speed: 15.62 Hz. Bias voltages: (c) 0.01 V. 65
4.6 Superstructure imaged on HOPG. (a) Current image recorded on cleaved HOPG surface revealing the presence of a superstructure along with the atomically-resolved crystal structure. (b) The corresponding FT of the current image in (a). The bright spots highlighted by cyan circles represent the superstructure with a periodicity of ~1.5 nm. Scanning speed: 15.62 Hz. Bias voltages: (a) 0.013 V. 65

5.1 Large-scale AFM imaging of an α–Mo_2C crystal. (a) A large-scale topographical image acquired on a α–Mo_2C crystal on copper foil. (b) Phase image acquired simultaneously with the topographical image in (a). Two regions with distinct phase contrast are visible on the surface, indicative of different materials (I and II). (c) A zoomed-in topographical image on the region highlighted in (b), showing material II is "draped" over material I. (d) Height profiles recorded along the arrows A and B in (c). The profile along A shows a height difference of ∼8 Å between materials I and II, consistent with a monolayer of graphene. The profile along B shows two terraces separated by a step of height ∼5 Å on I, consistent with a single unit cell of α–Mo_2C. 72

5.2 Atomic-resolution imaging of the α–Mo_2C (100) surface under ambient conditions via C-AFM. (a) Current map recorded on top of the α–Mo_2C crystal via C-AFM under ambient conditions by focusing on a small area similar to the one represented by the blue circle in 5.1(a). (b) FT corresponding to the current map shown in (a). The bright spots highlighted by white circles represent the lattice structure of α–Mo_2C (100) with a periodicity of ∼2.2 Å. (d) Atomic model of the α–Mo_2C (100) surface. All images were obtained with an applied normal load of 0.0 nN, and at a scanning frequency of 15.62 Hz. Bias voltages: (a) 0.01 V. 73

5.3 Imaging defects on α–Mo_2C under ambient conditions via C-AFM. (a) Current image showing different types of defects on α–Mo_2C, featuring relatively "compact" bright (maroon circles) and dark (green circles) defects, as well as elongated (cyan ovals) bright and dark defects. (b) The corresponding topographic image for the current map in (a) that shows no sign of the defects. (c) Zoomed-in current image on the compact defects reveal that they laterally extend ∼2-5 nm. (d) The corresponding topographic image for the current image shown in (c). All images were obtained with an applied normal load of 0.0 nN, and at a scanning frequency of 15.62 Hz. Bias voltages: (a) 0.5 V, (c) 0.7 V. 75

5.4 Atomic-resolution imaging of compact defects on α–Mo_2C under ambient conditions via C-AFM. (a) Current image showing the atomically-resolved surface structure along with multiple, compact bright defects. (b) A smaller current image featuring two compact bright defects. Note that the symmetry of the lattice appears to be disturbed near the defects. (c) Current image showing a compact, dark defect. Unlike the bright defects in (a) and (b), the lattice structure is uninterrupted over the dark, defective area. All images were obtained with an applied normal load of 0.0 nN, and at a scanning frequency of 15.62 Hz. Bias voltages: (a) 0.01 V, (b) 0.5 V, (c) 0.2 V. 76

5.5 Atomic-resolution imaging of elongated defects on α–Mo_2C under ambient conditions via C-AFM. (a) Current map recorded on α–Mo_2C showing an elongated bright defect that extends up to ∼11 nm. (b) Current map recorded on α–Mo_2C showing another elongated bright defect that extends up to ∼12 nm. Yellow dotted lines indicate the crystallographic directions of symmetry of the underlying lattice, whereas the blue dotted lines indicate the longitudinal directions of the defects. All images were obtained with an applied normal load of 0.0 nN, and at a scanning speed 15.62 Hz. Bias voltages: (a) 0.2 V, (b) 0.5 V. 77
5.6 Current image recorded on α–Mo_2C, showing a concentrated dark defect surrounded by enhanced charge density. Scanning speed 15.62 Hz. Bias voltage: 0.05 V. 78
5.7 Observation of room-temperature charge ordering on α–Mo_2C via C-AFM. (a) Current image recorded on α–Mo_2C, showing periodic modulation of charge, along with two defects. (b) The corresponding FT of the image shown in (a). The bright spots highlighted by red circles represent the lattice structure of α–Mo_2C with a periodicity of ∼2.2 Å, while the bright spots highlighted by green circles represent the charge modulation with a periodicity of ∼11.4 Å. (c) Another current image recorded on α–Mo_2C exhibiting charge ordering. (d) The corresponding FT of the image shown in (c). The bright spots highlighted by red and green circles represent lattice structure of α–Mo_2C (periodicity ∼2.2 Å) and periodic modulation of charge (periodicity ∼11.1 Å), respectively. (e) Enlarged current image of the area highlighted by the white dotted square in (c), showing an ordering of charge superimposed on the atomic surface lattice. All images were obtained with an applied normal load of 0.0 nN and at a scanning frequency of 15.62 Hz. Bias voltages: (a) 0.1 V; (c) 1.3 V; (e) 1.3 V. . . . 79

Acknowledgments

I express my sincere gratitude to my advisor, Prof. Mehmet Baykara for his continued support and guidance. In last four and half years, I have come a long way to become an independent researcher. In retrospect, Prof. Baykara's mentorship has been imperative to this critical training that has shaped me to a confident researcher. His recommendations and insightful comments have helped me develop my research outlook and scientific communication skills. His patient guidance and feedback have helped me overcome critical research hurdles. Other than research and writing, he has also facilitated numerous professional development opportunities for me. I feel extremely privileged to work with such a kind and supportive mentor.

I am also thankful to Prof. Ashlie Martini, Prof. Roberto Andresen Eguiluz and Prof. Min Hwan Lee for being in my thesis committee and their support.

My sincere thanks go to the Air Force Office of Scientific Research (Award No. FA9550-19-1-0035) and University of California Merced for supporting my research. I have also been fortunate to work with talented collaborators such as Prof. Goknur C. Buke and her team at TOBB University of Economics and Technology. Many thanks to Prof. Buke and her team for providing the amazing Mo_2C samples and the Air Force Office of Scientific Research (Award Number FA9550-19-1-7048 and FA9550-22-1-0358) for supporting the associated work at Prof. Buke's lab. I also thank Prof. Jun Liu for insightful discussions.

I would also like to extend my appreciation to my fellow Baykara Lab members, namely Wai H. Oo, Gokay Adabasi and Kutay Ozyurt for their support and help. I feel extremely fortunate to work with such friendly and respectful lab members. I am also thankful to all my friends and colleagues at UC Merced for their help and support.

I am indebted to my parents for their steadfast belief in me, respecting my decisions in critical stages of my life and raising me as an independent woman. Last but not the least, I am grateful to my partner, Shiekh Zia Uddin who has always been there when I needed help the most. I highly appreciate our scientific discussions as well. I look forward to many more scientific discussions and life adventures with him.

Curriculum Vita

Saima Aktar Sumaiya

Research Interests

Scanning probe microscopy, 2D materials, surface electronic structure and defects of low-dimensional materials, dynamic surface processes, nanotribology.

Education

Ph.D. Mechanical Engineering 2018-2022
University of California, Merced
CGPA: 3.94/4.00

M.S. Mechanical Engineering 2018-2020
University of California, Merced
CGPA: 3.94/4.00

B.S Mechanical Engineering 2010-2015
Bangladesh University of Engineering and Technology (BUET)
CGPA: 3.92/4.00

Employment and Professional Experience

Graduate Research Assistant
University of California, Merced 2019-Present

R&D Applications Intern
Plasmatreat USA, Inc. 2022 (Jun-Aug)

Facility User
Molecular Foundry,Lawrence Berkeley National Laboratory 2019-2020

Graduate Teaching Assistant
University of California, Merced 2018-2019

Lecturer
Sonargaon University, Dhaka, Bangladesh 2016-2017

Research Milestones

- Demonstrated true atomic-resolution surface imaging under ambient conditions via conductive atomic force microscopy (C-AFM).

- Imaged a variety of defects on multiple samples with atomic resolution via C-AFM.
- Demonstrated the versatility of the C-AFM technique by imaging different classes of materials with atomic resolution.

Awards and Honors

- AVS 2022 National Student Award, 2022
- Graduate Dean's Dissertation Fellowship, UC Merced, 2022
- Accepted as a Speaker at the First Annual Materials Innovators Workshop, Cornell University, 2022
- Accepted to CONDESA SEES Incubator Program, UC Merced, 2022
- 1st Place at NCCAVS 2022 Technical Symposium Poster Competition, 2022
- STLE Northern California Section Research Award, 2021
- Bobcat Fellowship, UC Merced, 2019-2021
- GSA Travel Fellowship, UC Merced, 2020
- Fields Family Fellowship, UC Merced, 2018-2019
- Dean's List, BUET, 2011-2015
- University Merit List, BUET, 2011-2015

Teaching Experience

- Teaching Assistant for Heat Transfer:
  Mean teaching evaluation grade from 33 students: 6.0/7.0
- Teaching Assistant for Finite Element Analysis:
  Mean teaching evaluation grade from 42 students: 6.2/7.0

Journal Publications

1. **Sumaiya, S.A.**, Liu, J., Baykara, M.Z., True Atomic-Resolution Surface Imaging and Manipulation under Ambient Conditions, ACS Nano, doi: 10.1021/acsnano.2c08321 (2022).

2. Vazirisereshk, M.R., **Sumaiya, S.A.**, Chen, R., Baykara, M.Z., Martini, A., Time-Dependent Electrical Contact Resistance at the Nanoscale, Tribology Letters 69, 50 (2021).

3. **Sumaiya, S.A.**, Martini, A., Baykara, M.Z., Improving the Reliability of Conductive Atomic Force Microscopy-based Electrical Contact Resistance Measurements, Nano Express 1, 030023 (2020).

4. **Sumaiya, S.A.**, Vazirisereshk, M.R., Martini, A., Baykara, M.Z., Measurement of Electrical Contact Resistance at Nanoscale Gold-Graphite Interfaces, Applied Physics Letters 115, 091602 (2019).

In Preparation

1. **Sumaiya, S.A.**, Demiroglu, I., Caylan, O.R., Buke, G.C., Sevik, C., Baykara, M.Z., Atomically- Resolved Defects on Thin Crystals of a Transition Metal Carbide (MXene): α-Mo_2C.

Invited Talks

1. **Sumaiya, S.A.**, True Atomic-Resolution Imaging under Ambient Conditions via Conductive Atomic Force Microscopy, Materials Innovators Workshop, Cornell University, May 2022.

2. **Sumaiya, S.A.**, Electrical Contact Resistance on the Nanoscale Investigated via Conductive Atomic Force Microscopy, STLE Northern California Section Meeting, May 2021.

Conference and Poster Presentations

1. **Sumaiya, S.A.**, Baykara, M.Z., Imaging and Manipulating Surface Electronic Landscapes under Ambient Conditions, 2022 MRS Fall Meeting & Exhibit, Boston, USA, November 2022.

2. **Sumaiya, S.A.**, Baykara, M.Z., True Atomic-Resolution Surface Imaging and Manipulation under Ambient Conditions via Conductive Atomic Force Microscopy, AVS 68th International Symposium and Exhibition, Pittsburgh, USA, November 2022.

3. **Sumaiya, S.A.**, Baykara, M.Z., True Atomic-Resolution Imaging under Ambient Conditions via Conductive Atomic Force Microscopy, 2022 MRS Spring Meeting & Exhibit, Hawaii, USA, May 2022.

4. **Sumaiya, S.A.**, Baykara, M.Z., True Atomic-Resolution Imaging under Ambient Conditions via Conductive Atomic Force Microscopy, NCCAVS 2022 Technical Symposium, Fremont, USA, February 2022.

5. **Sumaiya, S.A.**, Caylan, O.R., Buke, G.C., Baykara, M.Z., Atomically Resolved Imaging of Electronic Defects in a CVD Grown Transition Metal Carbide: α-Mo_2C, 2021 MRS Fall Meeting & Exhibit, Boston, USA, November 2021.

6. **Sumaiya, S.A.**, Vazirisereshk, Chen, R., M.R., Martini, A., Baykara, M.Z., Temporal Evolution of Electrical Contact Resistance Observed via Improved Conductive Atomic Force Microscopy, AVS 67 Virtual Symposium, October 2021.

7. **Sumaiya, S.A.**, Vazirisereshk, M.R., Martini, A., Baykara, M.Z., Measurement of Electrical Contact Resistance at Nanoscale Gold-Graphite Interfaces, 2020 Virtual MRS Spring/Fall Meeting & Exhibit, November 2020.

8. **Sumaiya, S.A.**, Vazirisereshk, M.R., Martini, A., Baykara, M.Z., Measurement of Electrical Contact Resistance at Nanoscale Gold-Graphite Interfaces, Molecular Foundry 2020 User Meeting, Virtual, August, 2020.

9. **Sumaiya, S.A.**, Vazirisereshk, M.R., Martini, A., Baykara, M.Z., Measurement of Electrical Contact Resistance at Nanoscale Gold-Graphite Interfaces, 2019 STLE Tribology Frontiers Conference, Chicago, USA, October, 2019.

Conference Proceedings

1. **Sumaiya, S.A.**, Talukder, M. M., Morshed, A. K. M. M., Forced Convection Heat Transfer in a Microchannel with Nanofluid Incorporating Different Geometry, 11th International Conference on Mechanical Engineering in Dhaka, Bangladesh (2015).

Journal Reviewer Appointments

- Surface Topography: Metrology and Properties.

Leadership and Synergistic Activities

- **Chancellor's Advisory Committee on the Status of Women**, UC Merced
  Organizing the "WomXn in the Spotlight" speaker series

- **Graduate Student Association**, UC Merced
  Communicating graduate students' concerns and issues to the school administration
- **MACES Summer Undergraduate Research Program**, UC Merced
  Showcasing research achievements to encourage undergraduate students towards STEM careers

Abstract

True Atomic-Resolution Imaging under Ambient Conditions via Conductive Atomic Force Microscopy

by

Saima Aktar Sumaiya

Doctor of Philosophy in Mechanical Engineering

University of California, Merced

A great number of chemical and mechanical phenomena, ranging from catalysis to friction, are dictated by the atomic-scale structure and properties of material surfaces. Despite such enormous significance, the principal tools utilized to characterize surfaces at the atomic level rely heavily on strict environmental conditions such as ultrahigh vacuum and low temperature. Results obtained under such well-controlled, pristine conditions bear limited relevance to the great majority of processes and applications that often occur under ambient conditions. In this thesis, we report true atomic-resolution surface imaging via conductive atomic force microscopy (C-AFM) under ambient conditions, performed at high scanning speeds. We hypothesize that atomic resolution can be enabled by either (i) a confined, electrically conductive pathway at the tip–sample contact, or (ii) tunneling through a confined water layer accumulated on the sample surface under ambient conditions. Our approach delivers atomic-resolution maps on a variety of material surfaces that comprise defects including single atomic vacancies. Using our method, we also report the capability of *in situ* charge state manipulation of defects on MoS_2. Finally, we employ the high-speed C-AFM methodology to study a thin transition metal carbide crystal (*i.e.*, an MXene), α–Mo_2C. Along with a variety of atomically-resolved defect structures, we observe an exotic electronic effect: room-temperature charge ordering. Our findings demonstrate that C-AFM can be utilized as a powerful tool for atomic-resolution imaging and manipulation of surface structure and electronics under ambient conditions, with wide-ranging applicability.

Chapter 1

Introduction

Structure and properties of different classes of materials on the atomic scale play a crucial role in understanding their fundamental physical and chemical behavior, as well as in synthesizing materials with desired properties and fabricating functional, small-scale devices. Atomic-scale structural knowledge provides information about crystal symmetry, presence of structural defects, strain etc. With the recent emergence of nanoscale devices, it is also important to be able to probe electrical, optical and magnetic properties of the materials employed in such devices on the atomic scale. Furthermore, with the advent of state-of-the-art synthesis techniques, atomic scale information about material structure and properties has the potential to provide crucial feedback for fine-tuning of synthesis parameters to achieve desired functionalities. Complementary to this practical point of view, atomic-scale investigations also deliver the capability to explore fundamental physical phenomena such as charge density waves, quantum hall effect, topological behavior, atomic collapse, atomic hopping etc. As such, atomic-resolution imaging (as well as spectroscopy) has been a focus of cutting-edge research for several decades and many techniques have been developed to perform them. Observing features on the atomic or molecular level via conventional optical microscopy is out of the realm of possibility, as such an approach would be limited by the wavelength of optical light which is about three orders of magnitude larger than atomic features. On the other hand, while some information about surface structures can be obtained from advanced variations of electron microscopy and global diffraction measurements etc., these approaches come with several drawbacks such as the necessity of extensive sample preparation, low throughput and the inability to extract local information with atomic resolution. Consequently, a direct, real-space method for the imaging of surface structures with atomic resolution was still lacking until the 1980s. The invention of scanning probe microscopy (SPM) in that decade opened that elusive door to scientists. SPM allows the study of surfaces with unprecedented resolution, down to the atomic scale. Along with atomic resolution imaging of surfaces, SPM is also capable of recording multiple surface properties

(such as elasticity, reactivity, and electron density) simultaneously. The two most common classes of SPM include Scanning Tunneling Microscopy (STM) and Atomic Force Microscopy (AFM). Details of the two methods are discussed in the rest of this chapter, followed by an outline of research objectives and a summary of the remaining chapters of the thesis.

1.1 Scanning Tunneling Microscopy

In 1981, Binnig and Rohrer invented the first STM which earned them the Nobel Prize in Physics in 1986, in record time [1]. The key factor that led to this achievement is the fact that STM can provide direct, real-space information about surface structures with atomic resolution. STM was developed based on the concept of quantum tunneling [2]. In particular, a very (ideally, atomically) sharp, conductive *tip* is brought into very close proximity (∼1 nm or below) of the sample surface to be studied, typically under ultrahigh vacuum (UHV) conditions. Upon the application of a bias voltage (V) electrons tunnel through the vacuum, resulting in a tunneling current (I) which is a function of tip-sample distance, bias voltage and local density of states (LDOS) of the sample. Under the application of a positive bias to the sample, electrons tunnel from the tip to the empty electronic states in the sample and vice versa under the application of a negative sample bias.

As the tip scans over the sample surface in a raster fashion, it records a 3-dimensional (3D) topographic map of the sample surface which is based on the tunneling current signal. The strong dependence of the tunneling current on tip-sample separation enables the high vertical resolution achievable via STM. A schematic diagram illustrating the operating principle of a typical STM is shown in Fig. 1.1. STM can be operated either in constant current or constant height mode. Constant current imaging record contours of constant tunneling current using a feedback system that modulates the tip-sample distance during scanning, and is usually employed on surfaces that feature a significant degree of structural roughness / discontinuities such as step edges and defects. On the other hand, constant height mode imaging can be used on areas of samples that are atomically flat and largely free of defects, which results in fast scanning due to the elimination of the feedback loop [3]. This allows to study processes with higher temporal resolution, although the approach is prone to thermal drift effects in the surface normal direction.

Tersoff and Hamann first discussed the interpretation of STM images based on tunneling current [4, 5]. They derived an expression of tunneling current, I assuming unperturbed sample and tip wave functions and then using Bardeen's formalism for perturbation. For small bias voltage and at low temperature, the expression for I resulted in

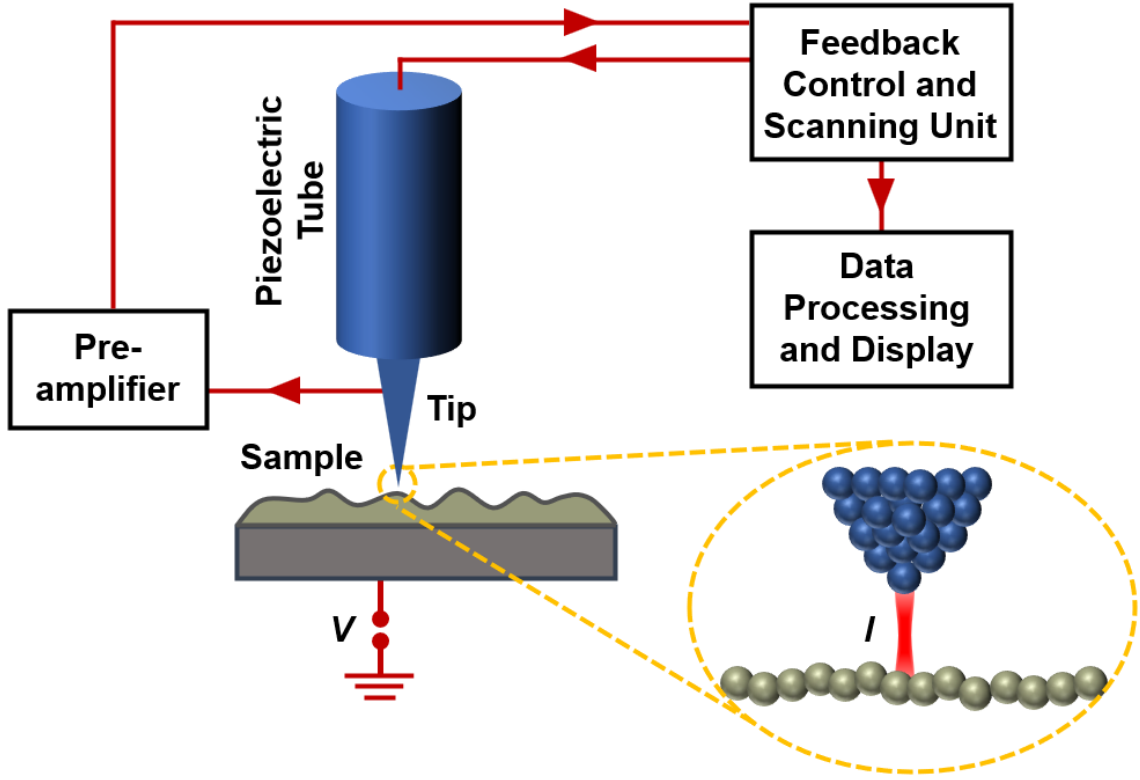

Figure 1.1: Schematic describing the operating principle of a typical STM.

$$I = \frac{2\pi}{\hbar} e^2 V \sum |M_{st}^2| \delta(E_s - E_F) \delta(E_t - E_F) \tag{1.1}$$

where M_{st} is the tunneling Matrix element between tip and sample wave functions, $\hbar$ is the reduced Planck's constant, e is the charge of an electron, and δ is the delta function. E_t, E_s, and E_F are the tip, sample, and Fermi energies, respectively. M_{st} is an integral over a surface, S between the tip and sample. According to Bardeen's formalism, the tunneling matrix can be expressed as

$$M_{st} = \frac{\hbar^2}{2m_e} \int (\varphi_t^* \nabla \varphi_s - \varphi_s \nabla \varphi_t^*) dS \tag{1.2}$$

where m_e is the mass of electron, ∇ is the differential operator, and φ_t and φ_s are the wave functions of the tip and sample, respectively.

Tersoff and Hamann further assumed the tip as spherically symmetric with only an s-wave function which yields the following expression for tunneling current.

$$I \propto \sum_{s} |\varphi_s(r_c)|^2 \delta(E_s - E_F) \tag{1.3}$$

where r_c is the center of curvature of the tip. The above summation corresponds to the local density of sample electronic states $\rho(r_c, E)$. Therefore, constant current images acquired via STM correspond to contours of constant density of sample electronic states. The assumption of a spherically symmetric tip is considered reasonable because even if the tip is asymmetric globally, the dominant portion of tunneling current results from the most protruding atom at the tip apex. However, the approximation of the s-wave function for the tip cannot explain experimental results in many cases. Instead of the s-wave function, Chen approximated the tip wave function as a p_z or d_z^2 dangling bond state that could explain atomic resolution images of close packed metal surfaces [6].

To explore the dependence of tunneling current, I on different parameters such as tip-sample separation (s), and bias voltage (V); Equation 1.3 can be rewritten as [7]

$$I \propto \sum_{s} |\varphi_s|^2 exp[-2\kappa(r+s)]\delta(E_s - E_F) \tag{1.4}$$

where r is the radius of tip and κ is the decay parameter,

$$\kappa = \sqrt{\frac{2m_e\phi}{\hbar^2} + k^2} \tag{1.5}$$

where ϕ is the average wave function and k is the parallel wave vector component of φ_s. For tunneling between planar, free-electron, metal electrodes at small biases ($V << \phi$), Equation 1.4 can be written as

$$I \propto \frac{V}{s} exp(-2\kappa s) \tag{1.6}$$

where κ can be approximated as

$$\kappa = 1.025\sqrt{\phi} \tag{1.7}$$

Therefore, the tunneling current is exponentially dependent on tip-sample separation and typically changes by an order of magnitude with a change of just 1 Å in tip-sample separation, thus providing a highly sensitive surface probe.

Soon after its invention, STM was used in many groundbreaking studies. STM unambiguously revealed the 7×7 reconstruction of Si(111) (see, Fig. 1.2(a)) which has been an unresolved problem in surface science for $\sim$20 years [8]. This study also reported the first true atomic resolution imaging of a surface. Next, STM was employed to perform spatially resolved surface tunneling spectroscopy *i.e.* to record images corresponding to the electronic distribution of surface states [9]. Later on,

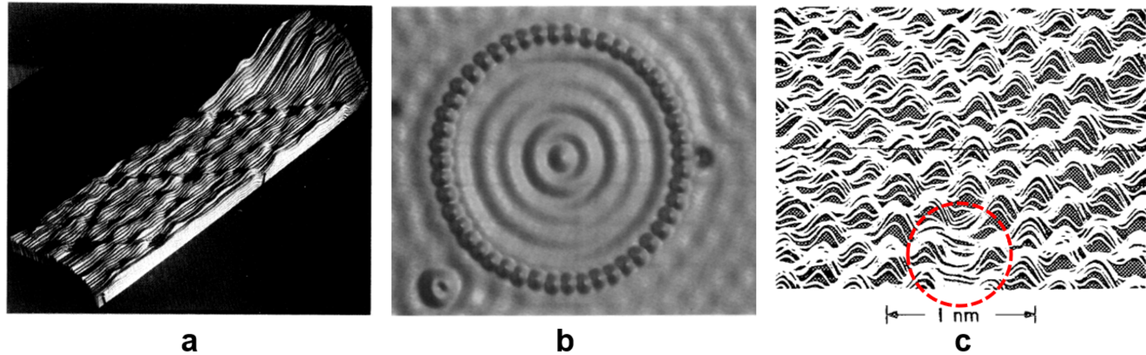

Figure 1.2: Seminal results obtained via STM: (a) First atomic resolution STM image revealing the 7×7 reconstruction of Si(111) surface. (b) 48 Fe atoms are arranged on Cu(111) surface resulting in confinement of electrons. (c) Atomic resolution STM image of a cleaved 2H-TaS_2 surface with a single atom vacancy in the highlighted region. Images (a), (b), and (c) taken from Ref. [8], [11], and [12], respectively.

this technique was named scanning tunneling spectroscopy (STS). Since tunneling has been utilized to study superconducting states, with this new tunneling microscope, STM paved the way for studying spatial variation of superconducting properties at the microscopic level [10]. The first demonstration of electron confinement to a quantum corral was performed via STM by arranging 48 Fe atoms on Cu(111) surface, as shown in Fig. 1.2(b) [11]. Soon STM was employed to image atomic scale defects. As shown in Fig. 1.2(c), a single atom vacancy was imaged on a 2H-TaS_2 surface [12]. With all these impactful results, STM became an enormously powerful surface science technique. Nowadays, STM is routinely used for atomic resolution structural imaging and recording electronic information on surfaces [13–15]. STM is also frequently used to measure LDOS of a given sample and to electronically manipulate surfaces [16, 17]. Finally, large scale STM images can provide important topographic information such as surface roughness on the microscopic scale.

Despite all of its success, a major drawback associated with STM is the requirement of an electrically conductive sample, which excludes a lot of scientifically and technologically important materials from being studied. Another important drawback of STM is that the topographic and electronic information are convoluted in STM data (as both purely topographic and electronic irregularities manifest in the same fashion in recorded images), which at times makes it harder to distinguish between structural and electrical phenomena. STM also typically requires UHV conditions, extremely clean surfaces, and very sharp tips for good resolution and stable imaging. These limitations render STM an expensive and non-ideal tool for a large number of studies and material systems.

1.2 Atomic Force Microscopy

The invention of AFM in 1986 not only overcame many of the drawbacks associated with STM, but also led to the emergence of a much more versatile surface imaging technique. While raster scanning of a sharp tip on top of the surface to be studied is still the main principle, AFM operates based on the detection of interaction forces acting between the tip and the sample surface [18]. Therefore, it does not require the sample to be electrically conductive. As a result, AFM allows the study of a large number of material surfaces with very high spatial resolution, from the nano to the atomic-scale. As indicated above, the AFM tip scans over the sample surface in a raster fashion similar to an STM tip and can record topographic, mechanical, electrical, chemical and magnetic force signals with high spatial resolution. While scanning an area as small as 5 nm $\times$ 5 nm with AFM under appropriate conditions and using appropriate modes can reveal the atomic structure of a material [19], the method can, for instance, also be used to for diverse purposes such as probing the nanomechanical properties of samples such as human cells [20]. AFM also has the capability to operate in a wide variety of environmental conditions such as ambient, UHV, and liquid medium. Another important feature of AFM is that it can be easily integrated with other instruments for multiple analyses. All these flexibilities have made AFM a very powerful and widely used research tool in many branches of science and technology including physics, chemistry, materials science, and nanoscale engineering.

1.2.1 General Operating Principle of AFM

AFM is a unique type of microscope in the sense that it does not generate an image through optical and electronic means; instead, it's a mechanical microscope that 'touches' the sample with a very sharp tip and generates a 3D image that contains topographical information regarding the surface down to sub-nanometer resolution. The main components of an AFM are a piezo scanner, a cantilever with a very sharp tip at the end that acts as the force sensor, and control electronics. The piezo scanner made of piezoelectric material is used to move the tip at the end of the cantilever relative to the sample. The scanning speed of an AFM is limited by the resonant frequency of the piezo electric scanner; in general, the higher the resonant frequency, the faster the scanning speed. Most modern AFM cantilevers are microfabricated with a reflective coating on the top side and a very sharp tip at the end. As the tip rasters over the sample, the cantilever bends due to the changes in the interatomic forces between the tip and the sample caused by topographic variations. A laser beam is focused on the top side of the cantilever and the reflection of the laser beam on a photodiode records the deflection signal of the cantilever. A schematic showing some of the main components of an AFM is shown in Fig. 1.3. In typical operation, the

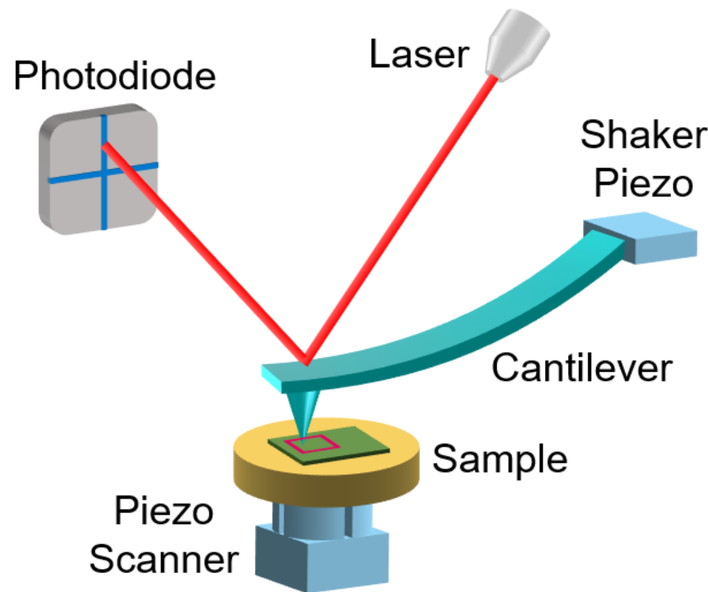

Figure 1.3: Schematic describing the operating principle of a typical AFM.

electronics (i) record the cantilever deflection signal, (ii) generate signals for the piezo scanner movement using a feedback loop with a PID controller that typically aims to keep the interaction force (as inferred from the cantilever deflection) constant during scanning, and (iii) display/save the recorded topography signal (as inferred from the piezo scanner movement in the vertical direction) in the desired format. An optical microscope is also usually integrated with the AFM to help locate areas of interest on the sample surface and position the laser beam precisely on the backside of the cantilever.

An AFM can be operated in a variety of modes. These modes not only differ in the experimental procedure but also record different types of information. Suitability of a mode also greatly depends on the nature of the sample. Some common modes of operation of an AFM, together with their relevance to atomic-resolution imaging, are discussed below.

1.2.2 Contact Mode AFM

In order to understand contact mode operation of AFM, it is important to think about the nature of tip-sample interaction forces as shown in Fig. 1.4. When the tip is far away from the sample surface, it does not interact with the sample surface and therefore the cantilever is at the zero-deflection state. As the tip approaches

the sample surface, it first experiences attractive forces (*e.g.*, due to van der Waals interactions) and the cantilever bends towards the sample. This is the so-called attractive regime. As the distance between the tip and the sample decreases, the attractive force increases and eventually the tip snaps into the surface when the rate of change of the attractive force with distance is higher than the deflection stiffness of the cantilever. If the tip is further pushed towards the surface, the cantilever experiences repulsive forces and bends in the opposite direction (*i.e.* away from the surface). Contact mode AFM is typically operated in this repulsive regime and is the most straightforward of all topographic imaging modes since the deflection of the cantilever is directly correlated to the topography of the sample. A schematic of contact mode AFM is shown in Fig. 1.5(a). A feedback loop adjusts the position of the cantilever base with respect to the sample by moving the piezo scanner in the vertical (z) direction so that the cantilever deflection is at a constant value during scanning. Even though contact mode is capable of generating topographical images with nm-scale lateral resolution, it has several disadvantages; for instance, since the tip operates in the repulsive regime, it can damage soft samples during imaging as there is a shearing (*i.e.* lateral) force between the tip and the sample at all times. Furthermore, in contact mode, the tip apex can easily become blunt which prevents atomic resolution imaging. Essentially, when the tip makes contact with the sample surface at the onset of scanning, its apex (which may have been initially atomically sharp) becomes blunt, undergoing structural rearrangement which takes place via interaction forces through effects such as atomic attrition and contact aging [21, 22]. This means that a cluster of multiple atoms, rather than a single atom at the apex is in contact with the sample surface during scanning. A corresponding schematic showing an AFM tip losing its sharpness after coming into contact with a surface is shown in Fig. 1.6. Under such conditions, as the tip scans over the sample surface, the interaction of the tip with the sample is effectively averaged over a rather broad area (*i.e.* over the cluster of tip atoms in contact with the surface) and as such, true atomic resolution imaging (as signified by the ability to image a single atomic vacancy) via contact mode AFM leaves the realm of possibility, while "lattice periodicity" can still be occasionally obtained with sufficiently sharp apex clusters [23].

1.2.3 Dynamic Modes of AFM

To overcome some of the limitations associated with contact mode AFM, dynamic modes of AFM have been developed. In dynamic mode AFM, the cantilever is oscillated at/near its resonant frequency by way of a shaker piezo (see, Fig. 1.3) at a very close proximity to the sample (with average separations on the order of $\sim$1 nm). As the oscillating cantilever scans over the sample surface, the oscillation amplitude and frequency change due to the changes in the tip-sample interaction forces, which may be induced by topographical features, as well as difference in *e.g.*, mechanical

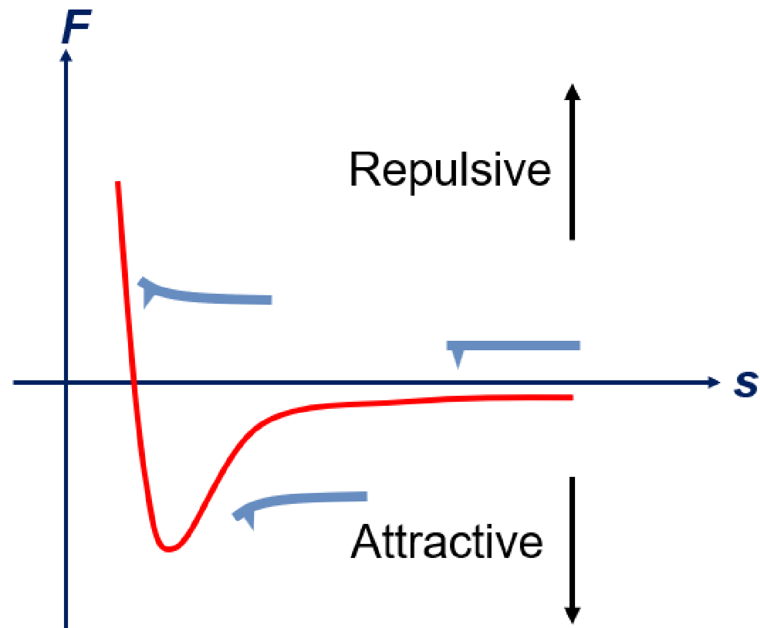

Figure 1.4: Schematic of tip-sample interaction force (F) as a function of separation distance (s).

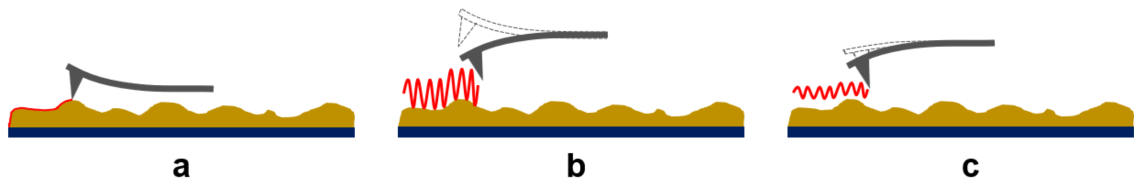

Figure 1.5: Different operational modes of AFM: (a) contact mode, (b) intermittent contact (*i.e.* tapping) mode and (c) non-contact mode.

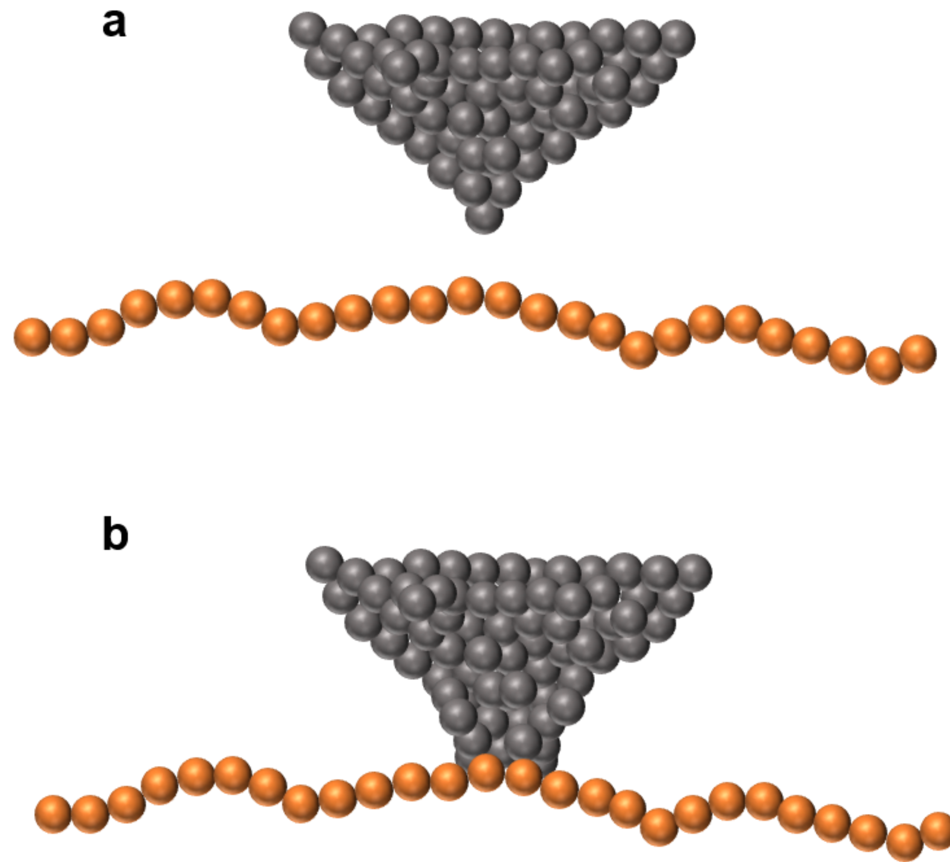

Figure 1.6: (a) Atomically sharp tip before contact is established with the surface. (b) Tip apex losing sharpness after contact is established with the surface.

and electrical characteristics. As in contact mode, a feedback loop is used to adjust the z height of the cantilever base such that either the amplitude or the frequency of the oscillation is kept constant. Depending on which interaction regime the tip is operated in, dynamic mode can be classified either as intermittent contact (*i.e.* tapping) mode or non-contact mode. In the intermittent contact mode, a relatively larger oscillation amplitude is employed such that for each oscillation cycle the tip comes into contact with the sample (*i.e.* "taps on it") and then goes back, rapidly modulating between the attractive and repulsive interaction regimes. On the other hand, in non-contact (NC) mode, a small oscillation amplitude is applied to the tip so that it is always in the attractive regime. NC-AFM is frequently employed to study surface structures with atomic resolution, due to the possibility of maintaining the atomic sharpness of tips during entire scans. Schematics of intermittent contact and

NC-AFM are shown in Fig. 1.5(b) and (c), respectively. The primary advantages of dynamic mode AFM are decreased tip and sample damage due to the absence of lateral forces and increased spatial resolution (for NC-AFM). More details about the NC-AFM are discussed below.

1.2.3.1 Non-contact Atomic Force Microscopy

In NC-AFM, the cantilever is oscillated at its resonance frequency (typically with small amplitudes on the order of 1 nm and below) while the tip remains in the attractive interaction regime. As the tip scans over the sample surface, changes in the oscillation frequency due to the interaction between the tip apex and sample surface are detected while keeping the oscillation amplitude fixed via a feedback loop. That's why NC-AFM is also referred to as frequency modulation (FM) operation. The change in the oscillation frequency is used as a second feedback signal to control the vertical position of the cantilever base. Since the tip does not come into contact with the surface (*i.e.* does not enter the repulsive interaction regime), the sharpness of the tip is conserved in this mode of operation. For stable and reliable data acquisition, most atomic-resolution NC-AFM imaging is performed under UHV conditions, and occasionally at low (*i.e.* liquid helium or nitrogen) temperatures, even though there have been experiments that could be performed under ambient conditions and at room temperatures [24].

The tip-sample interactions that cause the changes in the oscillation frequency of the cantilever in NC-AFM can be classified either as long-range or short-range. The ubiquitous van der Waals interactions fall into the long-range category and conventionally thought not to contribute to atomic resolution imaging. On the other hand, short-range chemical interactions are more relevant in achieving atomic resolution.

The first true atomic resolution imaging via NC-AFM was demonstrated in 1995 by imaging the 7×7 reconstructed surface of Si(111) [25]. Soon, NC-AFM was employed to image atomic scale defects in InP [26]. NC-AFM is also able to distinguish between atoms of different chemical identity (see, Fig. 1.7(a)) [27]. While NC-AFM is primarily performed in the attractive regime, it has been demonstrated that by partially operating in the repulsive regime with a chemically functionalized tip apex, it is possible to image individual bonds and atoms inside a molecule (see, Fig. 1.7(b, c)) [28, 29]. All these results emphasized NC-AFM's role as a powerful tool for the atomic resolution imaging of a large variety of materials including metals, semiconductors and insulators.

Although NC-AFM is a very powerful tool for atomic resolution imaging of surfaces, it also comes with certain severe limitations. First of all, in order to achieve good resolution with NC-AFM, operation under UHV conditions is typically a must (with the exception of some studies performed in liquids [30]) due to the fact that under ambient conditions, sample surfaces are usually covered with a layer of contam-

ination adsorbed from the environment. Therefore, when the cantilever oscillates at a very close proximity to the sample surface, it could very well be oscillating above or within the contamination layer as depicted in Fig. 1.8. When the cantilever oscillates above the contamination layer (Fig. 1.8(a)), the tip-sample interaction forces are mostly screened by this layer. Imaging under such conditions results in data that are not truly representative of the actual sample surface and have low resolution. On the other hand, when the cantilever oscillates within the contamination layer as shown in Fig. 1.8(b), it is possible to achieve good resolution at extremely small tip-sample distances and with small oscillation amplitudes, but this comes at the cost of frequent tip crashes with the sample that are mostly unavoidable, making it next to impossible to record reliable data [31]. To avoid these issues, atomic resolution NC-AFM is typically performed under UHV conditions to suppress the adsorption of contaminants onto the sample surface. Another limitation associated with NC-AFM is that it often requires imaging at low temperatures to minimize thermal fluctuations and increase the signal-to-noise ratio [24]. Last but not least, mastering the skill to reliably operate multiple simultaneous feedback loops takes years to develop. This fact, together with the necessity of additional, often custom equipment to operate under UHV and at low temperature, makes the atomic-resolution NC-AFM technique available to only a handful of research groups in the world.

1.3 Research Objectives

As discussed above, the two main surface science techniques that can directly image a sample surface with true atomic resolution are STM and NC-AFM. STM works based on the tunneling current between the tip and sample which is relatively easy to detect and features good signal to noise ratio in well-designed/built setups. However, since topographic information in this case is extracted from the tunneling current signal, convolution with electronic features is unavoidable. The method is also strictly restricted to conductive samples. On the other hand, NC-AFM works based on measuring interaction forces between the tip and sample manifesting as changes in the oscillation frequency signal of the AFM cantilever. This, however, requires sophisticated electronics that control multiple feedback loops, experienced operators, excellent instrumentation and a stable environment. A critical limitation associated with both STM and NC-AFM is that they typically cannot be performed under ambient conditions for atomic-resolution imaging. Exceptions include certain reports of atomic-resolution STM imaging under ambient conditions [32, 33]. It should also be noted that great progress has been made in recording true atomic-resolution images of a wide variety of surfaces under a liquid environment, without restrictions of sample conductivity [34, 30]. Finally, there has been one isolated report of true atomic-resolution imaging via NC-AFM on a calcite surface in air, [35] despite mul-

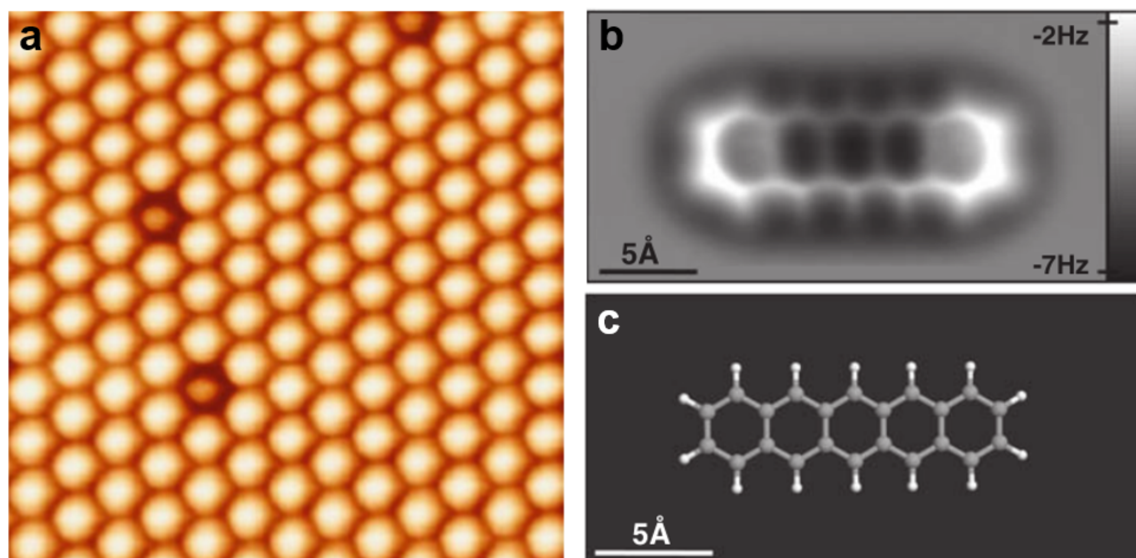

Figure 1.7: Seminal results obtained via NC-AFM: (a) NC-AFM topographic image of a Sn/Si alloy surface distinguishing atoms of different chemical identity. (b) Constant height AFM image of pentacene acquired with a tip functionalized with CO at the apex. (c) Ball and stick model of the pentacene molecule imaged in (b). Image (a) is taken from Ref. [27], and images (b) and (c) are taken from Ref. [28]

Figure 1.8: Challenges of NC-AFM imaging under ambient conditions: tip can be oscillating (a) above or (b) within the contamination layer on surface, leading to complications for atomic-resolution measurements.

tiple attempts at imaging other surfaces [36]. Therefore, to suppress the adsorption of contaminants and for reliable atomic resolution data acquisition, both STM and NC-AFM require additional equipment for example, to maintain UHV or very low temperatures. As indicated earlier, all of these limitations have rendered atomic resolution imaging a rare capability that only a handful of research groups around the world are able to perform. On the other hand, adsorption/contamination in realistic environments can lead to important changes in chemical, mechanical, and electronic surface characteristics, which can have critical implications for functionality [37, 38]. Moreover, processes observed under the ideal yet unrealistic UHV environment bear limited relevance to technological applications such as heterogeneous catalysis, which often take place at elevated pressures. This leads to longstanding critical issues in surface science such as the *pressure gap* [39].

Based on the discussion above, a technique that can reliably provide true atomic resolution images of a sample surface under ambient conditions and at room temperature would be ideal. Motivated by this line of thought, we demonstrate in this thesis that true atomic resolution imaging can be performed under ambient conditions via a technique known as conductive atomic force microscopy (C-AFM). We show that the methodology robustly delivers atomic-resolution maps on a variety of sample surfaces. We further demonstrate that this methodology has huge potential to be employed to study and even electronically manipulate defects of two-dimensional (2D) materials. Furthermore, we gather clues regarding the mechanism that enables the true atomic-resolution capability of C-AFM under ambient conditions from parametric studies. Finally, we employ this methodology to study in particular member of an emerging material class (MXenes), *i.e.* thin crystals of the transition metal carbide α–Mo_2C.

1.4 Thesis Outline

This thesis consists of six chapters. In Chapter 1, the significance of atomic resolution imaging along with established, related techniques are introduced, followed by an overview of research objectives.

In Chapter 2, the operational principle of C-AFM is discussed first. This is followed by a demonstration of the *true* atomic-resolution direct, real-space surface imaging capability of C-AFM under ambient condition. In this chapter, we further investigate the mechanism behind the atomic-resolution capability of C-AFM by gathering clues from parametric studies.

In Chapter 3, we demonstrate that C-AFM robustly delivers true atomic-resolution maps on a variety of conductive material surfaces that have significant scientific and technological importance.

In Chapter 4, we present the potential of C-AFM to be employed for studying defects of low dimensional materials. Going one step further, we also demonstrate

that C-AFM can be employed for *in situ* electronic manipulation of defects.

In Chapter 5, we present an atomic-resolution study of defects and charge ordering on α-Mo_2C.

Finally, in Chapter 6, a brief summary of the thesis is presented with a concise outline for future work.

1.5 References

[1] G Binnig, H Rohrer, C Gerber, and E Weibel. Surface studies by scanning tunneling microscopy. *Physical Review Letters*, 49(1):57, 1982.

[2] G Binnig and H Rohrer. Scanning tunneling microscopy. *Surface Science*, 126(1-3):236–244, 1983.

[3] P K Hansma and J Tersoff. Scanning tunneling microscopy. *Journal of Applied Physics*, 61(2):R1–R24, 1987.

[4] J Tersoff and D R Hamann. Theory and application for the scanning tunneling microscope. *Physical Review Letters*, 50(25):1998, 1983.

[5] J Tersoff and D R Hamann. Theory of the scanning tunneling microscope. *Physical Review B*, 31(2):805, 1985.

[6] C J Chen. Origin of atomic resolution on metal surfaces in scanning tunneling microscopy. *Physical Review Letters*, 65(4):448, 1990.

[7] Z Zhang and C M Lieber. Characterization of complex materials by scanning tunneling microscopy: A look at superconductors with high critical temperatures. *Advances In Chemistry Series*, 245:479–479, 1995.

[8] G Binnig, H Rohrer, C Gerber, and E Weibel. 7×7 reconstruction on Si(111) resolved in real space. *Physical Review Letters*, 50(2):120, 1983.

[9] G Binnig, H Fuchs, C Gerber, H Rohrer, E Stoll, and E Tosatti. Energy-dependent state-density corrugation of a graphite surface as seen by scanning tunneling microscopy. *Europhysics Letters*, 1(1):31, 1986.

[10] S A Elrod, A Bryant, A L Delozanne, S Park, D Smith, and C F Quate. Tunneling microscopy from 300 to 4.2 K. *IBM Journal of Research and Development*, 30(4):387–395, 1986.

[11] M F Crommie, C P Lutz, and D M Eigler. Confinement of electrons to quantum corrals on a metal surface. *Science*, 262(5131):218–220, 1993.

[12] C G Slough, W W McNairy, R V Coleman, B Drake, and P K Hansma. Charge-density waves studied with the use of a scanning tunneling microscope. *Physical Review B*, 34(2):994, 1986.

[13] M M Ugeda, A J Bradley, S-F Shi, F H Da Jornada, Y Zhang, D Y Qiu, W Ruan, S-K Mo, Z Hussain, Z-X Shen, et al. Giant bandgap renormalization and excitonic effects in a monolayer transition metal dichalcogenide semiconductor. *Nature Materials*, 13(12):1091–1095, 2014.

[14] Z-Y Jia, Y-H Song, X-B Li, K Ran, P Lu, H-J Zheng, X-Y Zhu, Z-Q Shi, J Sun, J Wen, et al. Direct visualization of a two-dimensional topological insulator in the single-layer 1T′-WTe_2. *Physical Review B*, 96(4):041108, 2017.

[15] M M Ugeda, A J Bradley, Y Zhang, S Onishi, Y Chen, W Ruan, C Ojeda-Aristizabal, H Ryu, M T Edmonds, H-Z Tsai, et al. Characterization of collective ground states in single-layer $NbSe_2$. *Nature Physics*, 12(1):92–97, 2016.

[16] Y Niimi, T Matsui, H Kambara, K Tagami, M Tsukada, and Hiroshi Fukuyama. Scanning tunneling microscopy and spectroscopy of the electronic local density of states of graphite surfaces near monoatomic step edges. *Physical Review B*, 73(8):085421, 2006.

[17] J Repp, G Meyer, F E Olsson, and M Persson. Controlling the charge state of individual gold adatoms. *Science*, 305(5683):493–495, 2004.

[18] G Binnig, C F Quate, and C Gerber. Atomic force microscope. *Physical Review Letters*, 56(9):930, 1986.

[19] A Schwarz, W Allers, U D Schwarz, and R Wiesendanger. Detection of doping atom distributions and individual dopants in InAs (110) by dynamic-mode scanning force microscopy in ultrahigh vacuum. *Physical Review B*, 62(20):13617, 2000.

[20] S E Cross, Y-S Jin, J Rao, and J K Gimzewski. Nanomechanical analysis of cells from cancer patients. In *Nano-Enabled Medical Applications*, pages 547–566. Jenny Stanford Publishing, 2020.

[21] J J Mazo, D Dietzel, A Schirmeisen, J G Vilhena, and E Gnecco. Time strengthening of crystal nanocontacts. *Physical Review Letters*, 118(24):246101, 2017.

[22] Q Li, T E Tullis, D Goldsby, and R W Carpick. Frictional ageing from interfacial bonding and the origins of rate and state friction. *Nature*, 480(7376):233–236, 2011.

[23] Y Gan, E J Wanless, and G V Franks. Lattice-resolution imaging of the sapphire (0 0 0 1) surface in air by AFM. *Surface Science*, 601(4):1064–1071, 2007.

[24] M Z Baykara. Noncontact atomic force microscopy for atomic-scale characterization of material surfaces. In *Surface Science Tools for Nanomaterials Characterization*, pages 273–316. Springer, 2015.

[25] F J Giessibl. Atomic resolution of the Silicon (111)-(7 $\times$ 7) surface by atomic force microscopy. *Science*, 267(5194):68–71, 1995.

[26] H Ueyama, M Ohta, Y Sugawara, and S Morita. Atomically resolved InP (110) surface observed with noncontact ultrahigh vacuum atomic force microscope. *Japanese Journal of Applied Physics*, 34(8B):L1086, 1995.

[27] Y Sugimoto, P Pou, M Abe, P Jelinek, R Pérez, S Morita, and O Custance. Chemical identification of individual surface atoms by atomic force microscopy. *Nature*, 446(7131):64–67, 2007.

[28] L Gross, F Mohn, N Moll, P Liljeroth, and G Meyer. The chemical structure of a molecule resolved by atomic force microscopy. *Science*, 325(5944):1110–1114, 2009.

[29] L Gross, F Mohn, N Moll, G Meyer, R Ebel, W M Abdel-Mageed, and M Jaspars. Organic structure determination using atomic-resolution scanning probe microscopy. *Nature Chemistry*, 2(10):821–825, 2010.

[30] T Fukuma, K Kobayashi, K Matsushige, and H Yamada. True atomic resolution in liquid by frequency-modulation atomic force microscopy. *Applied Physics Letters*, 87(3):034101, 2005.

[31] P Eaton and P West. *Atomic force microscopy.* Oxford university press, 2010.

[32] T Schimmel, H Fuchs, S Akari, and K Dransfeld. Nanometer-size surface modifications with preserved atomic order generated by voltage pulsing. *Applied Physics Letters*, 58(10):1039–1041, 1991.

[33] R García. Atomic-scale manipulation in air with the scanning tunneling microscope. *Applied Physics Letters*, 60(16):1960–1962, 1992.

[34] K Miyata, J Tracey, K Miyazawa, V Haapasilta, P Spijker, Y Kawagoe, A S Foster, K Tsukamoto, and T Fukuma. Dissolution processes at step edges of calcite in water investigated by high-speed frequency modulation atomic force microscopy and simulation. *Nano Letters*, 17(7):4083–4089, 2017.

[35] D S Wastl, M Judmann, A J Weymouth, and F J Giessibl. Atomic resolution of calcium and oxygen sublattices of calcite in ambient conditions by atomic force microscopy using qPlus sensors with sapphire tips. *ACS Nano*, 9(4):3858–3865, 2015.

[36] A J Weymouth, D Wastl, and F J Giessibl. Advances in AFM: seeing atoms in ambient conditions. *e-Journal of Surface Science and Nanotechnology*, 16:351–355, 2018.

[37] H Ibach. Adsorbate-induced surface stress. *Journal of Vacuum Science & Technology A: Vacuum, Surfaces, and Films*, 12(4):2240–2245, 1994.

[38] T O Wehling, K S Novoselov, S V Morozov, E E Vdovin, M I Katsnelson, A K Geim, and A I Lichtenstein. Molecular doping of graphene. *Nano Letters*, 8(1):173–177, 2008.

[39] R Imbihl, R J Behm, and R Schlögl. Bridging the pressure and material gap in heterogeneous catalysis. *Physical Chemistry Chemical Physics*, 9(27):3459, 2007.

Chapter 2

Demonstration of True Atomic-Resolution Surface Imaging under Ambient Conditions

2.1 Conductive Atomic Force Microscopy

Conductive atomic force microscopy (C-AFM) is an important AFM-based technique where a conductive AFM tip is employed to investigate the electronic properties of a given sample. C-AFM is frequently utilized in both imaging and spectroscopic modes. In the imaging mode, a conductive tip scans the sample surface in contact mode, *i.e.* in the repulsive regime under the application of a bias voltage between the tip and the sample. Such scans provide both the topographic and conductivity maps of the sample surface with high spatial resolution, simultaneously. The two data maps are independently acquired as topographic information is obtained from cantilever deflection whereas conductivity information is recorded via the amount of current flow through the conductive tip. As such, C-AFM overcomes one of the major drawbacks associated with STM where both topographic and conductivity information, in a convoluted fashion, are acquired from tunneling current. Moreover, in C-AFM, the tip can be fixed at a given position on the sample surface and current can be recorded as a function of the applied bias, which is known as current-voltage (I-V) spectroscopy. A schematic of C-AFM is shown in Fig. 2.1. The method of C-AFM has been extensively used to study a multitude of sample systems since its first demonstration in the early 1990s [1, 2]. One of the first C-AFM studies was performed to measure local dielectric properties of silica/silicon oxide, a vital component of very large-scale integration (VLSI) devices [3]. C-AFM had significant contributions to the development of nanoelectronics. For example, C-AFM has been used not only for electrical characterization of carbon nano-tube (CNT) transistors but also

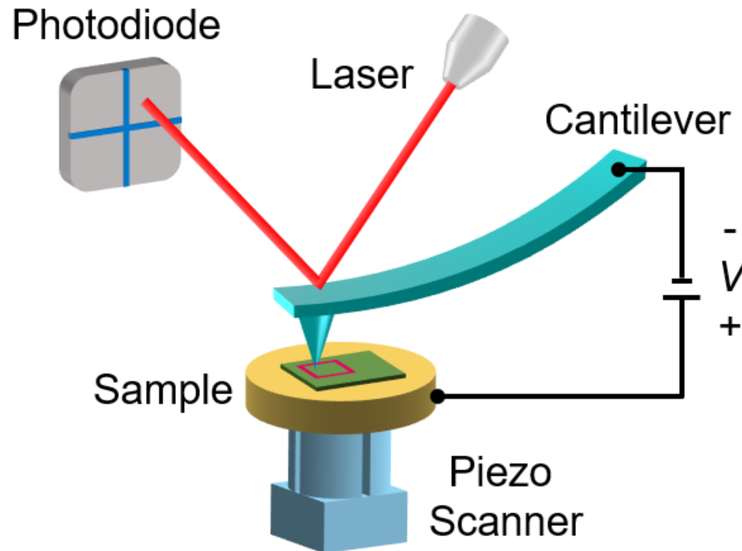

Figure 2.1: Schematic describing the operation of a typical C-AFM set-up.

to induce defects on CNTs and study the resulting changes in electrical properties [4, 5]. Furthermore, it has been employed to study layer-by-layer dielectric break down of 2D materials [6], perform local photolithography via anodic oxidation [7], and study resistive switching behavior of metal-insulator-metal junctions [8]. Other nanostructures that have been studied via C-AFM include quantum dots, nanowires, nanowire-based transistors etc. [9–12]. With C-AFM, one can also probe mechanical and electrical properties simultaneously by recording force-distance (F-d) and I-V curves [13]. Such studies can provide information about the nanoscale physical characteristics of the contact formed between the tip and the sample. Finally, C-AFM has also been extensively utilized to study the electrical properties of molecular tunnel junctions in the last decade with the underlying hope of developing nanoscale circuits based on the nonlinear I-V characteristics of molecules [14].

The key component of a C-AFM experiment is the conductive tip. In general, different types of conductive tips are commercially available such as metal coated tips, conductive-diamond-coated tips, whole metal body tips etc. C-AFM experiments are highly sensitive to the structure and chemistry of the tips and different tips are suitable for different types of experiments. While metallic tips can be made with sharp apexes (< 25 nm), conductive-diamond-coated tips typically have larger radii of curvature. Diamond-coated tips also have higher resistivity compared to metal coated tips. Even though metallic tips have low resistivity which can be a desirable property for most C-AFM experiments, exposure to ambient conditions usually leads to the

formation of an oxide on top of the tip apex. It also should be considered that metallic tips wear out much faster than diamond tips and that they tend to mechanically deform during the course of most measurements. Therefore, it is essential to choose the proper tip for a given C-AFM experiment.

2.2 History of Atomic Resolution Imaging via C-AFM

Well before the term C-AFM was coined, imaging based on conduction through a contact between tip and sample were performed via an SPM-based technique, the so called point contact microscopy (PCM) [1, 15, 16]. In case of PCM, the tip "touches" the sample surface. As a result, the potential barrier for conduction is greatly reduced and the tip-sample interaction is repulsive. The pioneering work on imaging with lattice resolution via PCM as opposed to tunneling through a tip-sample gap as in regular STM, was performed by Smith *et al.* [15]. Even though they claim to have achieved atomic resolution on highly oriented pyrolytic graphite (HOPG), what they observed was simply periodic bright spots separated by 2.46 Å which does not correspond to the interatomic distance of carbon atoms on HOPG surface (*i.e.* 1.42 Å). Instead, the observed bright spots can be the α-carbon atoms that have neighbors in the underlying layer or β-carbon atoms that do not have neighbors in the underlying layer, or simply the hollow sites of the graphite lattice. Smith *et al.* used an STM setup for their PCM measurement on HOPG under UHV conditions. However, they were only able to achieve lattice resolution at very low temperatures maintained with liquid helium. They speculated that at low temperature, the stiffer or hardened state of tip and sample, and longer electron mean free paths facilitate the acquisition of lattice resolution through the point contact. They further hypothesized that conduction from a single atom at the tip apex may be responsible for the obtained lattice resolution which is nowadays considered unlikely to happen as contact areas are known to be much broader than a single atom in contact mode AFM operation.

As a step forward, Enachescu *et al.* were able to achieve lattice resolution on HOPG at room temperature via PCM under UHV conditions (see, Fig. 2.2(a)) [17]. They demonstrated simultaneous recording of lattice resolution in topography, friction and conductivity maps. Since there were instances when they were able to achieve lattice resolution in the conductivity channel but not in topography or friction channel, they ruled out that the atomic stick-slip mechanism is responsible for the lattice resolution in the conductivity map. Rather, they attributed it to a collective effect between a broad tip and the sample such as the Pethica effect [20]. Enachescu *et al.* applied large loads of ~100-300 nN while imaging and treated their conductive tips via voltage pulsing before measurements. They used tungsten carbide coated tips for

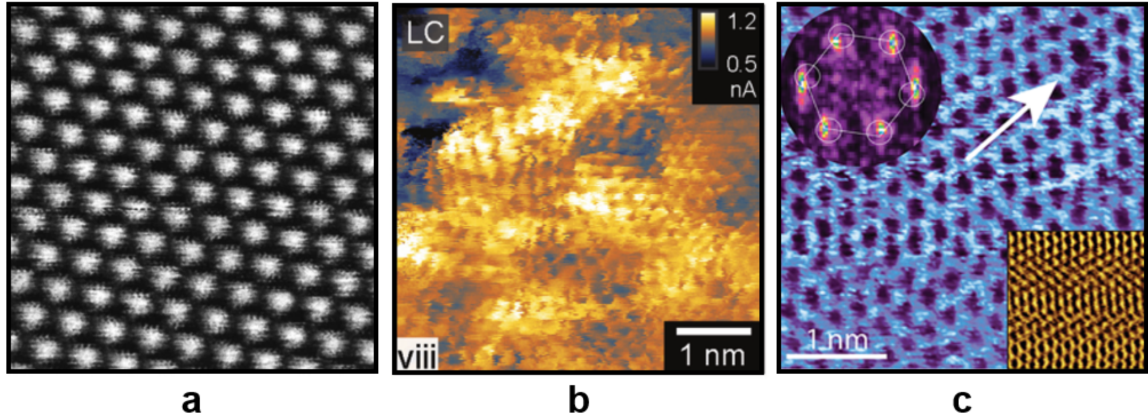

Figure 2.2: High resolution conductivity mapping through contact microscopy as opposed to STM under controlled environments. (a) Lattice resolution current map obtained on HOPG via PCM under UHV. (b) High resolution current map obtained on TiO_2 via C-AFM under UHV. (c) Atomic-resolution current map obtained on WS_2 via C-AFM under inert N_2 environment with a S vacancy indicated by the white arrow. Images (a), (b), and (c) taken from Refs. [17], [18], and, [19] respectively.

their measurements and speculated that the tips may have a poorly conducting layer which partially breaks during voltage pulsing or scanning. They further speculated that this phenomenon can be limited only to the tungsten carbide tips.

Later on, it was demonstrated for different tip materials that the electrically conductive area at a tip apex can be orders of magnitude smaller than the physical/mechanical contact area [21, 22]. Specifically, Celano *et al.* showed that for a physical contact area of 100 nm^2 between the tip and the sample (as calculated via continuum-based contact mechanics models), the electrical contact area can be less than 10 nm^2 [22]. They attributed this discrepancy to the micro-roughness of tip apices employed in their experiments.

In 2018, Rodenbucher *et al.* used C-AFM under optimized measurement conditions, in particular, under UHV on clean surfaces with low bias and a sensitive I/V converter, for high resolution imaging of transition metal oxide surfaces to observe the spatial variation in local conductivity due to phase transitions [18]. At first, they imaged HOPG as a prototypical sample to demonstrate atomic resolution imaging. But again, they observed a periodicity of 2.45 Å which corresponds to lattice resolution, not true atomic resolution (as would be proven by the presence of single, atomic defects or the imaging of both types of carbon atoms in the HOPG lattice). Even though they claim to image metal oxide surfaces such as TiO_2, $SrTiO_3$ etc. with true atomic resolution (see, Fig. 2.2(b)), they did not compare their periodicity values

with the actual periodicities of their samples nor did they allocate atomic positions on their periodic conductivity maps. Therefore, there remains questions whether the observed resolution (which is of rather limited quality) is truly atomic resolution or lattice resolution. In particular, while they attributed some of the features in the C-AFM images to defects or vacancies, these are not clearly resolved in the images.

True atomic resolution imaging via C-AFM was first reported by Bampoulis *et al.* in 2018 [23]. They imaged WSe_2 and $Mo_xW_{1-x}Se_2$ under a dry nitrogen atmosphere. Later on, Nowakowski *et al.* also reported true atomic resolution imaging via C-AFM under nitrogen environment [19]. They reported atomic vacancies, adatoms and periodic modulation due to electronic effects on WS_2 (see, Fig. 2.2(c)).

Based on the discussion above, even though it has been demonstrated that C-AFM is capable of imaging with true atomic-resolution under certain, controlled measurement conditions, this capability is yet to be demonstrated under uncontrolled, ambient conditions. Motivated by this line of thought, in the present work, we aim to perform atomic-resolution imaging via C-AFM under ambient conditions and explore the robustness and reliability of the methodology.

2.3 Methods

2.3.1 Sample Preparation

ZYB-quality HOPG samples were sourced from Ted Pella, and cleaved mechanically following the scotch tape method [24] prior to C-AFM imaging. As a substrate for the transition metal dichalcogenide (TMD) samples such as molybdenum disulfide (MoS_2, sourced from 2D Semiconductors), we used Si/SiO_2 chips coated consecutively with a $\sim$2 nm thick adhesion layer of Ti and a $\sim$50 nm thick Au film. TMD flakes were mechanically exfoliated on top of the Au-coated substrate via the scotch tape method as shown in Fig. 2.3. Finally, silver paint was applied on one side, bridging the conductive specimen holder and the Au film on which the TMD flakes are located.

2.3.2 C-AFM Measurements

The C-AFM measurements were performed using a commercial AFM (Asylum Research, Cypher VRS) under ambient conditions (Temperature: 22–23 °C; Relative humidity: 20–50%). Samples were inserted inside the AFM chamber without any prior treatment for surface cleaning. Commercially available, doped-diamond-coated conductive tips (NanoSensors, CDT-CONTR, normal stiffness: 0.6 ± 0.1 N/m and Adama Innovations, AD-2.8-SS, normal stiffness: 1.3 ± 0.1 N/m) were used for imaging. Initially, imaging of large areas (*e.g.* 10×10 μm) was performed without any bias to find regions of interest on the sample surface. For atomic-resolution imaging,

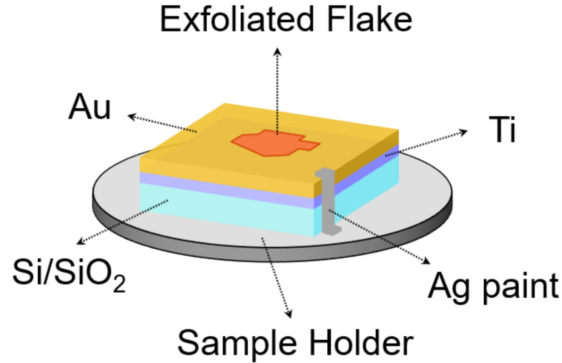

Figure 2.3: Schematic of the sample configuration used for C-AFM measurements on TMD samples.

small areas such as 5 × 5 nm were scanned in contact mode with an applied bias. Imaging was usually performed under only the snap-in force (*i.e.* the minimum observed in the F-d curve during tip approach) acting between the tip and the sample, with no normal load applied in addition. The magnitude of the snap-in force between the tip and different samples was on the order of a few nN. A representative force-distance curve is shown in Fig. 2.4. The bias voltage was always applied to the sample. An additional resistance of 10 MΩ was used in series occasionally to limit the current. The average periodicities of the atomic features observed in the images were calculated using the software Gwyddion by way of Fourier Transform (FT) and line profiles.

2.4 Demonstration of True Atomic-Resolution Surface Imaging

Initial measurements were first performed on the (0001) surface of HOPG, a prototypical benchmark sample. An atomic model of the HOPG (0001) surface is shown in Fig. 2.5(a). The HOPG crystal has three types of atomic sites: the carbon atoms that have neighbours in the layer underneath, the carbon atoms that do not have neighbours in the layer underneath, and the hollow sites at the center of the unit cells (blue, red and gray spheres in Fig. 2.5(a), respectively). Our measurement results are summarized by the current map in Fig. 2.5(b), where we are able to detect three types of atomic sites on the HOPG crystal characterized by low, high, and moderate current, separated by ∼1.4 Å. This observation is in strong contrast to previous works in the literature that predominantly feature lattice resolution, whereby only one type

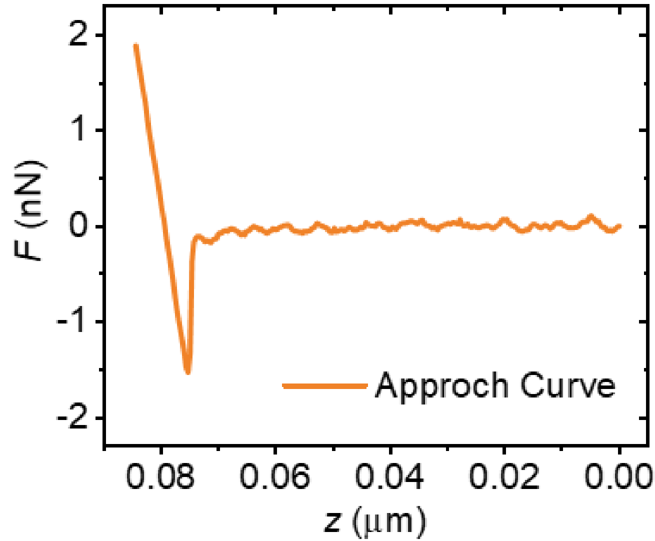

Figure 2.4: A representative force-distance (F-z) curve obtained with a conductive diamond coated tip on HOPG. The curve yields a snap-in force of ∼1.5 nN.

of atomic site, with a periodicity of ∼2.5 Å, is imaged as bright [17]. In our case, the reproducible imaging of three atomic sites separated by ∼1.4 Å (which corresponds to the interatomic distance of 1.42 Å between carbon atoms that is expected on an HOPG (0001) surface) demonstrates that we are indeed able to resolve all carbon atoms on the HOPG surface, as well as the hollow sites that exist at the center of the hexagons formed by them. Another point to note is that the topographic image (inset of Fig. 2.5(b)) that was simultaneously recorded with the current map does not comprise any atomic scale features, proving that in C-AFM the topographic and electronic information are recorded independently and the mechanism related to those channels are different.

Despite the promising result above, the key signature of true atomic-resolution imaging remains as the capability of identifying single atomic defects such as individual vacancies. We therefore turned our attention to MoS_2, a 2D semiconductor from the family of TMDs, which is (i) of significant electronic relevance [25] and (ii) expected to feature a higher density of defects than HOPG. An atomic model of MoS_2 is shown in Fig. 2.6(a). A current map obtained on MoS_2 is shown in Fig. 2.6(b), together with the simultaneously recorded topography map in the inset. There are distinct differences between the two channels: while we observe clearly-resolved, individual protrusions (separated by ∼3.2 Å, the distance between individual S as well as Mo atoms on MoS_2) in the current map, the topography map comprises vaguely

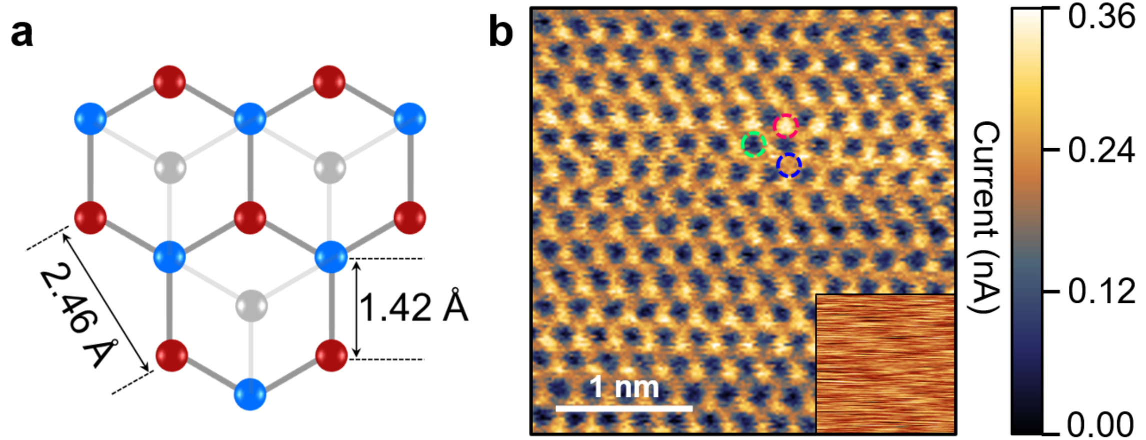

Figure 2.5: Resolving the true crystal structure of HOPG under ambient conditions via C-AFM. (a) Atomic model of the HOPG (0001) surface with red and blue spheres representing two types of carbon atoms, and the gray spheres representing carbon atoms in the layer below. (b) Current image obtained on HOPG showing three types of atomic sites characterized by low, high, and intermediate current (see the corresponding green, pink, and blue circles, respectively). The simultaneously recorded topography map (height range: 0–3.1 Å is shown in the inset, exhibiting no atomic-scale features.The current image was obtained with an applied normal load of 0.0 nN and at a scanning frequency of 15.62 Hz. Bias voltages: (b) 0.04 V.

resolved stripes of 0.2–0.6 Å in height. The observation of a much sharper contrast in the current channel in comparison with the topographic one once again indicates that the mechanism that results in high resolution in the current map is fundamentally different from that responsible for atomic-scale stick–slip patterns in the topography image [17]. On the other hand, the absence of any defects in the current map precludes us from claiming true atomic-resolution capabilities. As such, in order to demonstrate the key benchmark for the capability of true atomic-resolution imaging, another current map recorded on MoS_2 is shown in Fig. 2.6(c), where a cluster of multiple atomic-scale defects is imaged, in the form of missing bright spots. On the other hand, the corresponding topography map does not show the defects, proving that the averaging of interaction forces across the blunt tip–sample interface indeed precludes the imaging of atomic-scale defects in the topography channel. Taking one step further, another current map on MoS_2 is shown in Fig. 2.6(d), where we are able to demonstrate ultimate spatial resolution under ambient conditions. In particular, three types of atomic sites (see the green, purple, and pink circles in Fig. 2.6(d)) with the expected periodicity of $\sim$3.2 Å that feature low, high, and intermediate cur-

rent are simultaneously resolved. More importantly, we can clearly identify a single atomic defect in our image, manifesting as a missing “bright spot” that is indicated by the white arrow. This latter observation unequivocally proves that we are able to achieve true atomic-resolution imaging via the method of C-AFM under ambient conditions. Comparing our results to what has been achieved on MoS_2 via STM under UHV conditions, we tentatively assign the single atomic defect in our image to an S vacancy, due to the rather isolated effect it has on the local conductivity, in contrast to electronic effects extending over several nanometers expected for Mo vacancies and various dopants [26, 27].

2.5 Effect of Different Tip Materials

Despite its potential, the C-AFM technique has traditionally suffered from poor reproducibility. A key reason behind this limitation is the wear of the conducting tip coating [28]. During our studies, we explored different types of commercially available conductive tips, including PtSi, Ti/Ir, and doped- diamond-coated conductive tips. We could only achieve lattice resolution on an HOPG sample with PtSi tips (please see Fig. 2.7(a)) *i.e.* we only observed one maxima per unit cell rendering the image to feature lattice resolution instead of atomic-resolution. While we were able to achieve atomic resolution with Ti/Ir tips (please see Fig. 2.7(b)), the imaging was not robust and lacked reproducibility. Additionally, the longevity of both of these categories of tips were poor, as metal-coated tips tend to wear/melt easily. On the other hand, we found that doped-diamond-coated conductive tips are highly wear-resistant such that a single tip could be used to reproduce atomic-resolution images for more than a week of measurements recording over several hundreds of scans with true atomic-resolution. That’s why we ultimately used diamond-coated tips to achieve the results reported in this thesis.

2.6 Speed Dependence

To explore how different imaging parameters affect the atomic-resolution imaging capability of C-AFM, we performed parametric studies. At first, we investigated the effect of scanning speed on the quality of the images acquired. In particular, Fig. 2.8 and 2.9 showcase the effects of different scanning speeds on C-AFM imaging of MoS_2 under ambient conditions. Specifically, as one can see in Fig. 2.8, the spatial resolution gradually degrades with decreasing scanning speed. Conversely, Fig. 2.9 shows that resolution improves when the scanning speed is ramped up. The same doped-diamond-coated conductive tip was used for recording all the images in Fig. 2.8 and 2.9. These results show that i) the observed trends are not due to irreversible

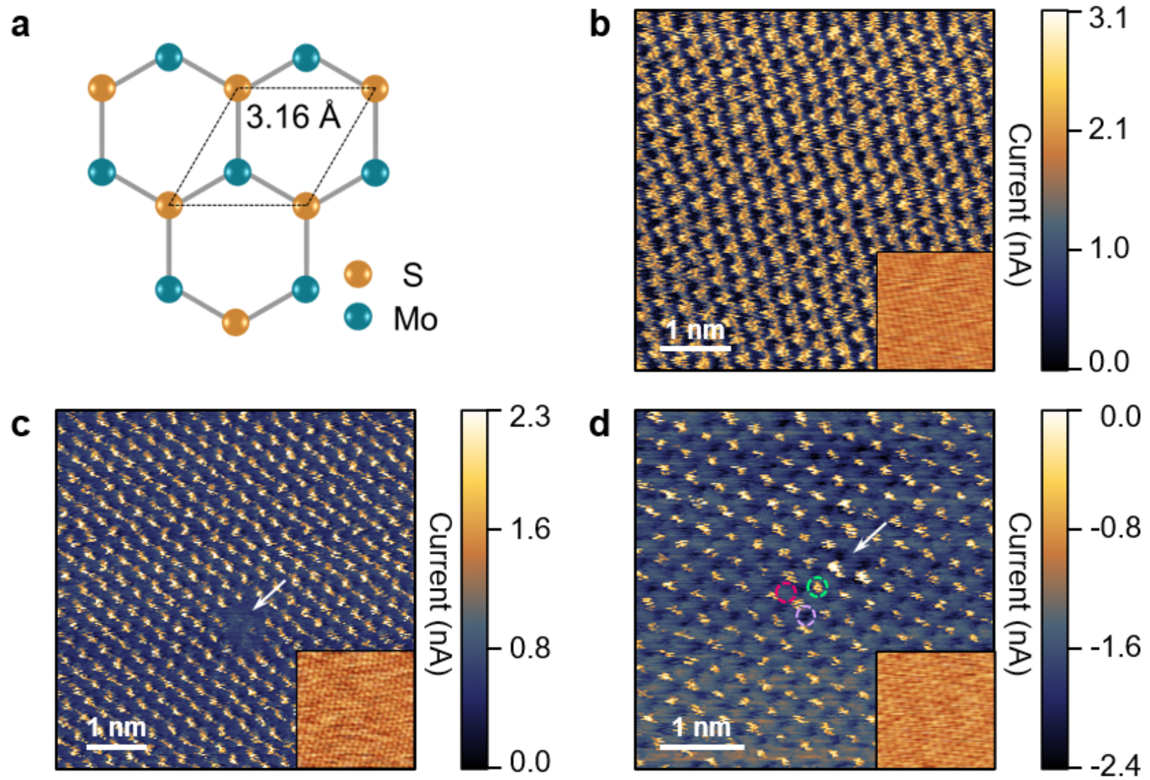

Figure 2.6: Demonstration of true atomic-resolution imaging under ambient conditions via C-AFM. (a) Atomic model of the MoS_2 (001) surface. (b) Current image obtained on MoS_2 showing well-defined protrusions separated by ∼3.2 Å. The simultaneously obtained topography map, with a stripe-like pattern, is shown in the inset (height range: 0–6.8 Å). (c) Current image obtained on MoS_2 showing multiple atomic-scale defects. The simultaneously obtained topography map is shown in the inset, with no trace of the defects (height range: 0–3.4 Å). (d) Current image obtained on MoS_2 exhibiting three types of atomic sites characterized by low, high, and intermediate current (see the corresponding green, purple, and pink circles, respectively). This image clearly captures a single atomic defect, as indicated by the white arrow. The corresponding topography map is shown in the inset (height range: 0–5.4 Å). All images were obtained with an applied normal load of 0.0 nN and at a scanning frequency of 15.62 Hz. Bias voltages: (b) 0.1 V; (c) 1.8 V; (d) -1.2 V.

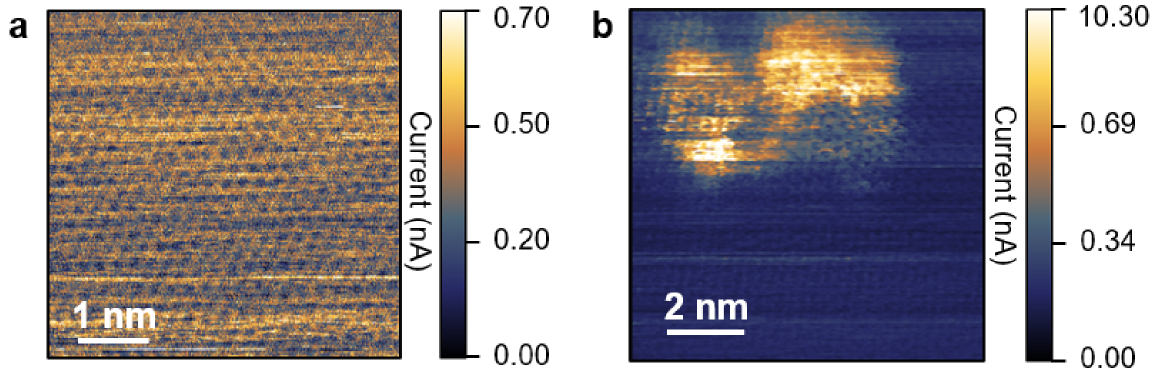

Figure 2.7: Effect of different tip materials on C-AFM imaging. (a) Representative current image obtained on HOPG with a PtSi tip. This image features a periodicity of ∼2.5 Å, indicating that it is not a true atomic-resolution image; it rather represents lattice resolution. (b) Representative current image obtained on MoS_2 with a Ti/Ir coated tip. Even though this image features atomic resolution, we typically do not observe true atomic resolution with this category of tip in a robust and reproducible manner. All images were obtained with an applied normal load of 0.0 nN, and at a scanning frequency of 15.62 Hz. Bias voltages: (a) 1.5 V, (b) 2.5 V.

modifications of the structure and/or chemistry of the tip apex during imaging, and ii) scanning speed has significant impact on obtaining atomic-resolution such that we obtain atomic-resolution only at high scanning speed. Furthermore, such speed dependence of resolution is also in contrast with what is typically observed in NC-AFM, where slow scanning provides higher signal-to-noise ratio and thereby, provides better resolution.

2.7 Load Dependence

We also performed C-AFM imaging at different normal loads while keeping the scanning speed fixed. In particular, Fig. 2.10 shows the effects of different normal loads, ranging from 0 nN to 60 nN, on C-AFM imaging of MoS_2 under ambient conditions. One can observe that even at 60 nN scanning load, atomic-resolution sustains, suggesting that within the range of 0–60 nN, the applied normal load did not seem to have an appreciable effect on imaging quality. Such a load dependence behavior is unusual, particularly, in case of contact mode operation where with increasing normal load, the tip-sample contact area is expected to increase [29]. Such bluntening of tip-sample contact is conventionally expected to degrade the imaging resolution,

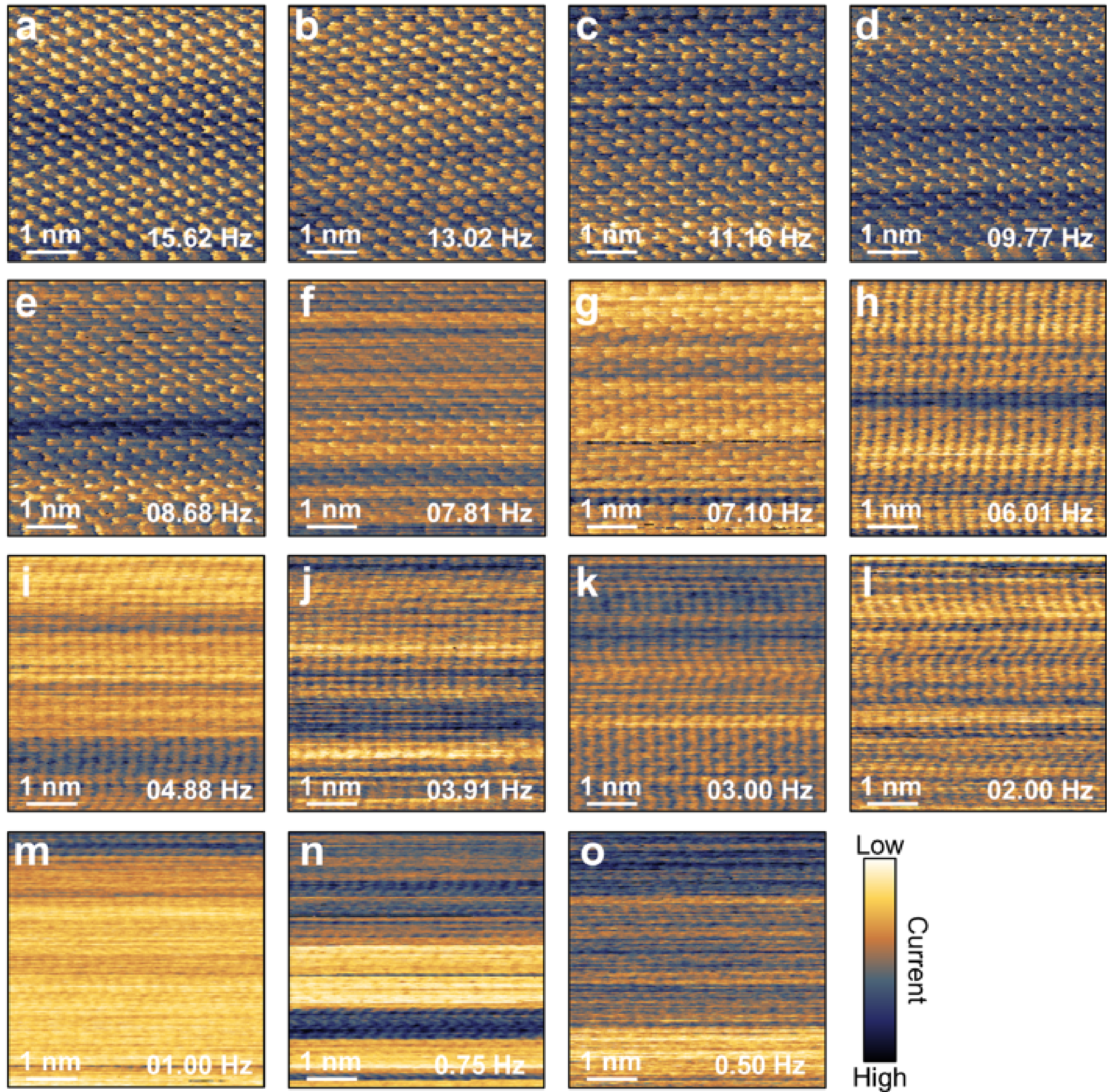

Figure 2.8: Speed dependence of atomic-resolution C-AFM imaging, with decreasing scanning speed. A series of images recorded on MoS_2 with decreasing scanning frequency (from 15.62 Hz to 0.50 Hz) showing a degradation in spatial resolution.

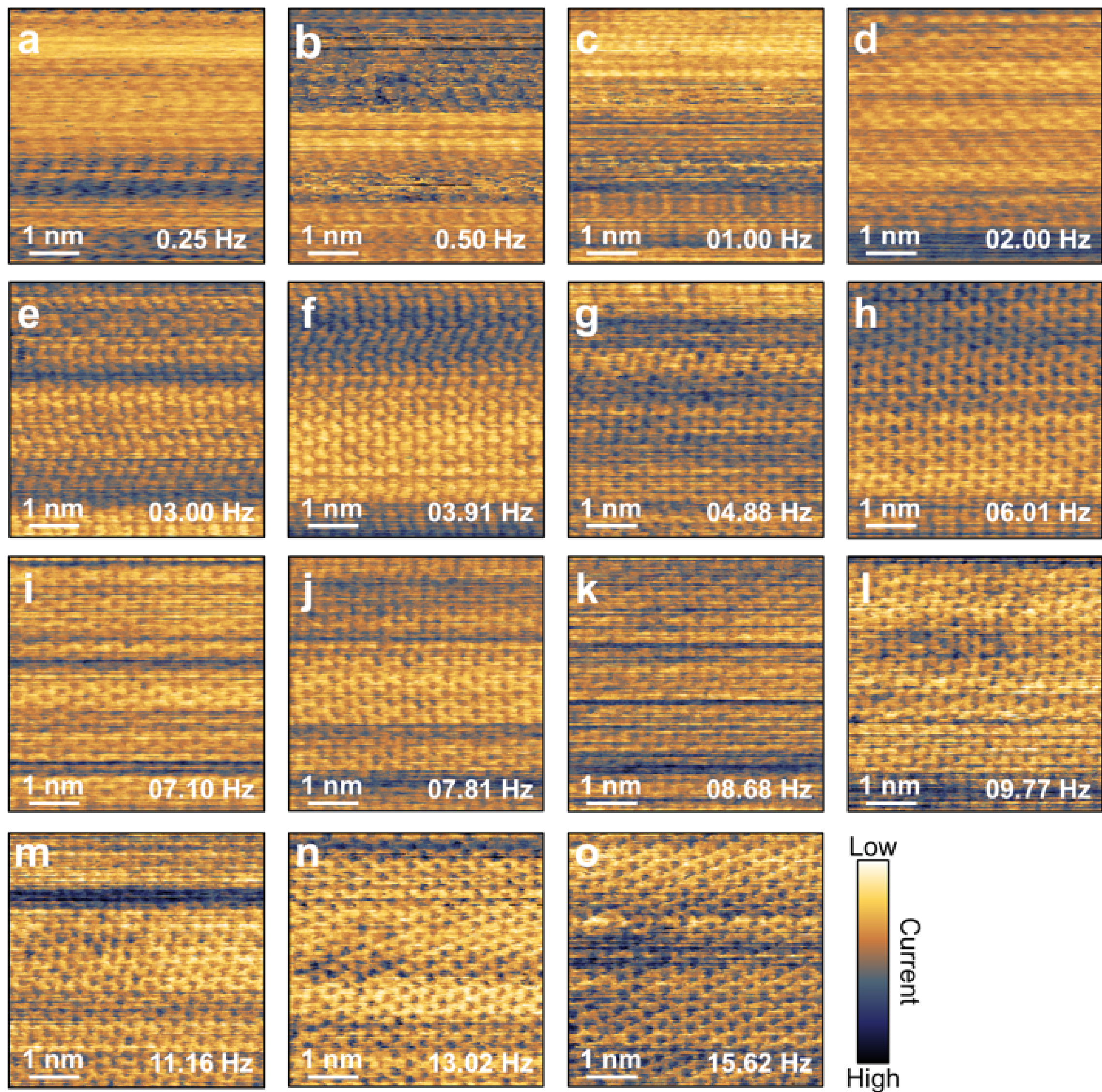

Figure 2.9: Speed dependence of atomic-resolution C-AFM imaging, with increasing scanning speed. A series of images obtained on MoS_2 with the same conductive tip used in Fig. 2.8, with increasing scanning frequency (from 0.25 Hz to 15.62 Hz), showing that atomic resolution emerges at higher scanning speeds.

which is not observed in our experiments.

2.8 Effect of Applied Bias

During our measurements, the applied bias voltage had be to tuned during each session to achieve / optimize atomic resolution. First of all, larger voltage values will result in higher C-AFM current output but also potentially undesirable effects (surface electrochemical reactions, electrostatic breakdown, field-assisted tunneling, etc.). On the other hand, the lower current values recorded under lower voltages will often result in poor C-AFM contrast for distinguishing atomic features. Therefore, there is typically an optimal voltage range for true atomic-resolution imaging. This ranges can be different for different experiments, for instance due to the following reasons:

1. The voltage required to observe atomic resolution can vary from tip to tip even if the same type of tip is being used, *e.g.* doped-diamond-coated tips. It can be due to the fact that different amount of voltages may be required to break down the different amount of contamination layers that may accumulate on different tip apexes.

2. With the same type of tip, the electrical conductivity as well as the junction state (*e.g.*, Ohmic or Schottky, surface state effects, etc.) between the tip and surface vary from sample to sample. Therefore, the optimized voltage value to achieve best atomic resolution is not universal for different samples.

3. Sometimes the applied voltage also has to be tuned over time to get clearer atomic-resolution images in a given session. This can be due to dynamic changes happening at the tip-sample contact amidst the contaminant molecules present under ambient conditions.

2.9 Robustness and Repeatability

The atomic-resolution C-AFM imaging is highly robust and reproducible in the sense that we could routinely image different conductive material surfaces with true atomic-resolution. We were also able to use a single tip to image different material surfaces (over several hundreds of scans) with true atomic-resolution without the need of any special tip preparation. Similarly, scanning repeatedly over the same defect resulted in consistent images, with the presence of some thermal drift. For instance, Fig. 2.11 shows two current maps recorded on MoS_2 featuring two extended defects. The two images were recording by way of continuous imaging. The time lapse between the two images is $\sim$4.3 minutes. The defect structures in both Fig. 2.11(a) and (b)

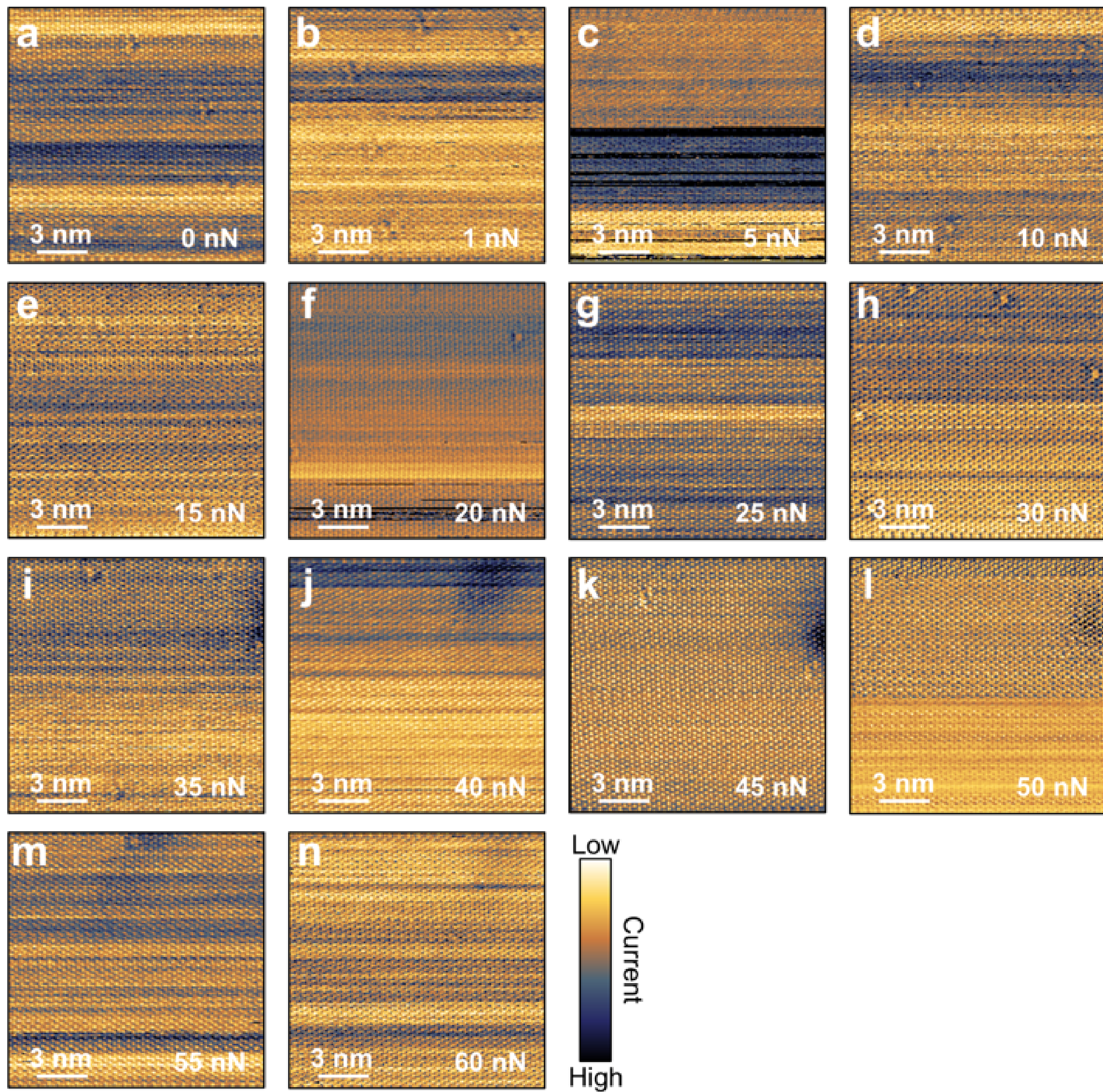

Figure 2.10: Load dependence of atomic-resolution C-AFM imaging. A series of images recorded on MoS_2 where the applied normal load varied from 0 to 60 nN during scanning. These images show that the capability of atomic-resolution imaging via C-AFM is not lost due to changes in normal load at the tip-sample junction.

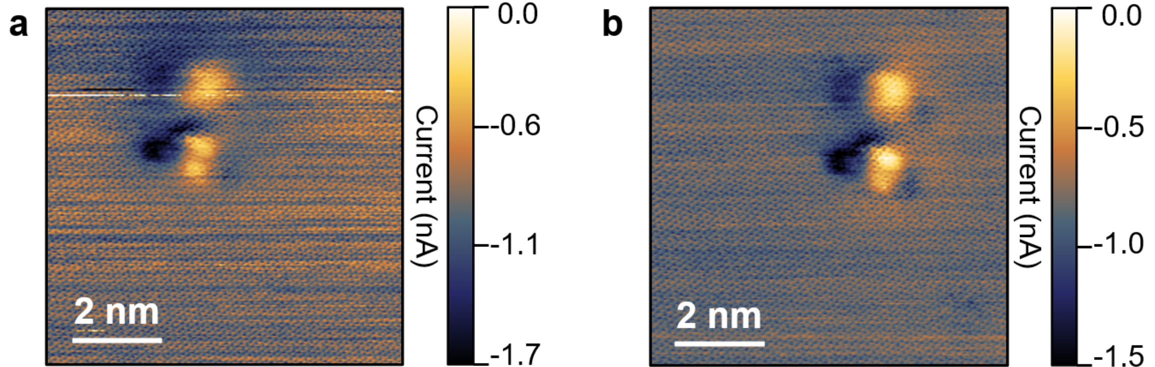

Figure 2.11: Reproducibility of defect imaging. (a) Current image obtained on MoS_2 featuring two extended defects. (b) Current image obtained upon continuous/repeated imaging of the same area shown in (a). The defect structures in both (a) and (b) appear similar, despite the presence of noticeable thermal drift. There were 15 images recorded between (a) and (b) by way of continuous scanning, corresponding to ~4.3 minutes. All images were obtained with an applied normal load of 0.0 nN, and at a scanning frequency of 15.62 Hz. Bias voltages: (a) -1.2 V, (b) -1.2 V.

appear similar. However, we observe noticeable presence of thermal drift between the two images.

2.10 Potential Mechanisms of True Atomic-Resolution Imaging

The fact that C-AFM is able to routinely achieve true atomic-resolution is unexpected, mainly because imaging is performed under contact mode operation, whereby the physical area of contact between the tip and the sample consists of multiple atoms (see Fig. 2.12). This should in principle lead to an averaging effect and the inability to resolve atomic-scale defects, as is the case for topographic imaging [30, 31]. We identify two primary factors that result in true atomic-resolution imaging capabilities for C-AFM under ambient conditions: (1) an atomically sharp conductive pathway as illustrated in Fig. 2.12, and (2) high-speed imaging. To investigate the first point, one can contrast the physical contact area formed between the AFM tip and the sample surface as estimated by continuum contact mechanics models, and the electrical contact area as estimated by contact resistance models. Considering the fact that the Hertz contact model does not take into account the adhesion force between tip and

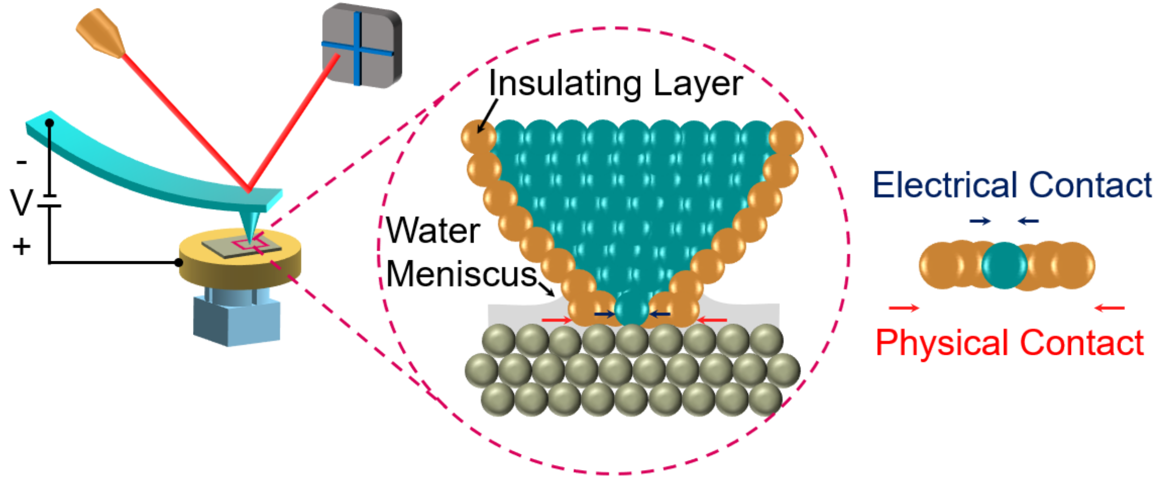

Figure 2.12: Schematic showing the discrepancy between the physical and electrical contact formed between the tip and the sample, as one of the possible explanations that can enable atomic-resolution C-AFM imaging.

sample, and our sample (in this case HOPG) has high elastic modulus, we used the Derjaguin-Muller-Toporov (DMT) model [32] to estimate the physical contact area. A schematic comparing the Hertz and the DMT model is shown in Fig. 2.13(a). The DMT model is expressed as:

$$a_m = \sqrt[3]{\frac{r}{E_{red}}(F + F_{ad})} \tag{2.1}$$

where a_m is the physical radius of the contact between the tip and the sample, r is the tip radius, F is the applied normal load, and E_{red} is the reduced Young's modulus which can be calculated as follows:

$$\frac{1}{E_{red}} = \frac{3}{4}(\frac{1 - {\nu_s}^2}{E_s} + \frac{1 - {\nu_t}^2}{E_t}) \tag{2.2}$$

where ν_s and ν_t are the Poisson's ratios of the sample and tip, respectively, and E_s and E_t are the Young's moduli of the sample and the tip, respectively.

On the other hand, we used Sharvin's model which is valid in the case of ballistic transport to estimate the electrical contact area [33]. Ballistic transport of electrons happens when the contact radius is smaller than the electron mean free path (λ) as depicted in Fig. 2.13(b). Considering that the contact radius in our experiments is expected to be much smaller compared to the electron mean free path in HOPG (200

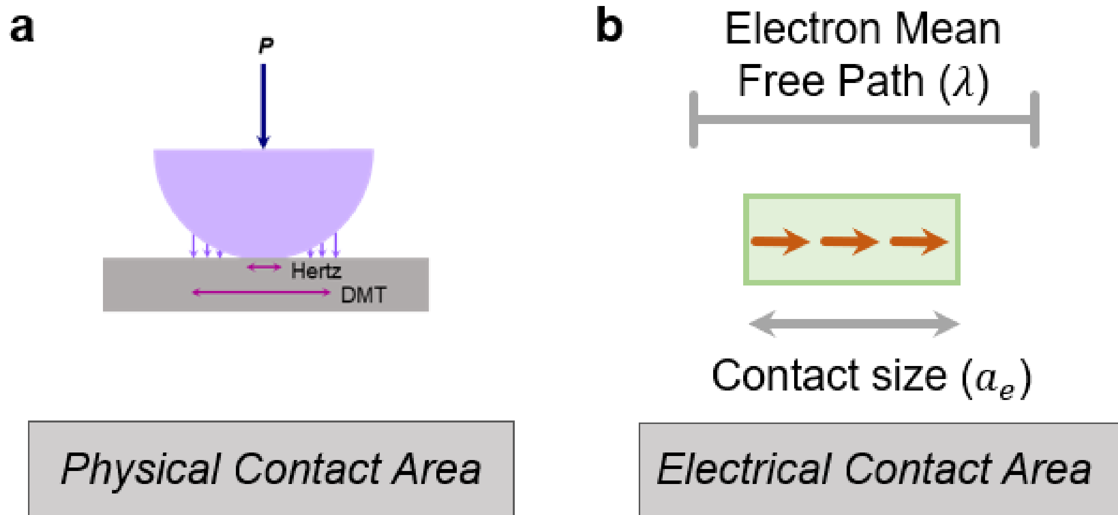

Figure 2.13: Schematic of models used to estimate physical and electrical contact areas. (a) A schematic showing the difference between the Hertz and DMT contact mechanics models. As opposed to the Hertz model, the DMT model takes into account the adhesion between the surfaces. (b) A schematic of the Sharvin model used to estimate electrical contact area for ballistic electron transport.

nm) [34], we used Sharvin's contact resistance model which is given by the following equation.

$$R = \frac{4\rho\lambda}{3\pi a_e^2} \tag{2.3}$$

where R is the electrical contact resistance between the tip and the sample, ρ is the effective electrical resistivity, λ is the effective electron mean free path and a_e is the radius of the electrical contact area.

To infer the physical contact radius established in our experiments from the DMT model, we recorded 189 force-distance curves on HOPG and extracted the magnitude of the average pull-off force (F_{ad}). A representative F-z curve is shown in Fig. 2.14(a). Parameters used in the DMT contact model were as follows; tip radius: 72.18 nm (extracted from scanning electron microscopy imaging), Young's modulus of HOPG: 25 GPa [35], Young's modulus of conductive diamond tip: 1200 GPa [36], Poisson's ratio of HOPG: 0.2440 [35], and Poisson's ratio of conductive diamond tip: 0.241 [36]. A histogram showing the distribution of the estimated physical contact radius between the tip and the HOPG sample, utilizing the 189 F-z curves is shown in Fig. 2.14(b). The estimated physical contact radius was found to be 2.68 ± 0.11

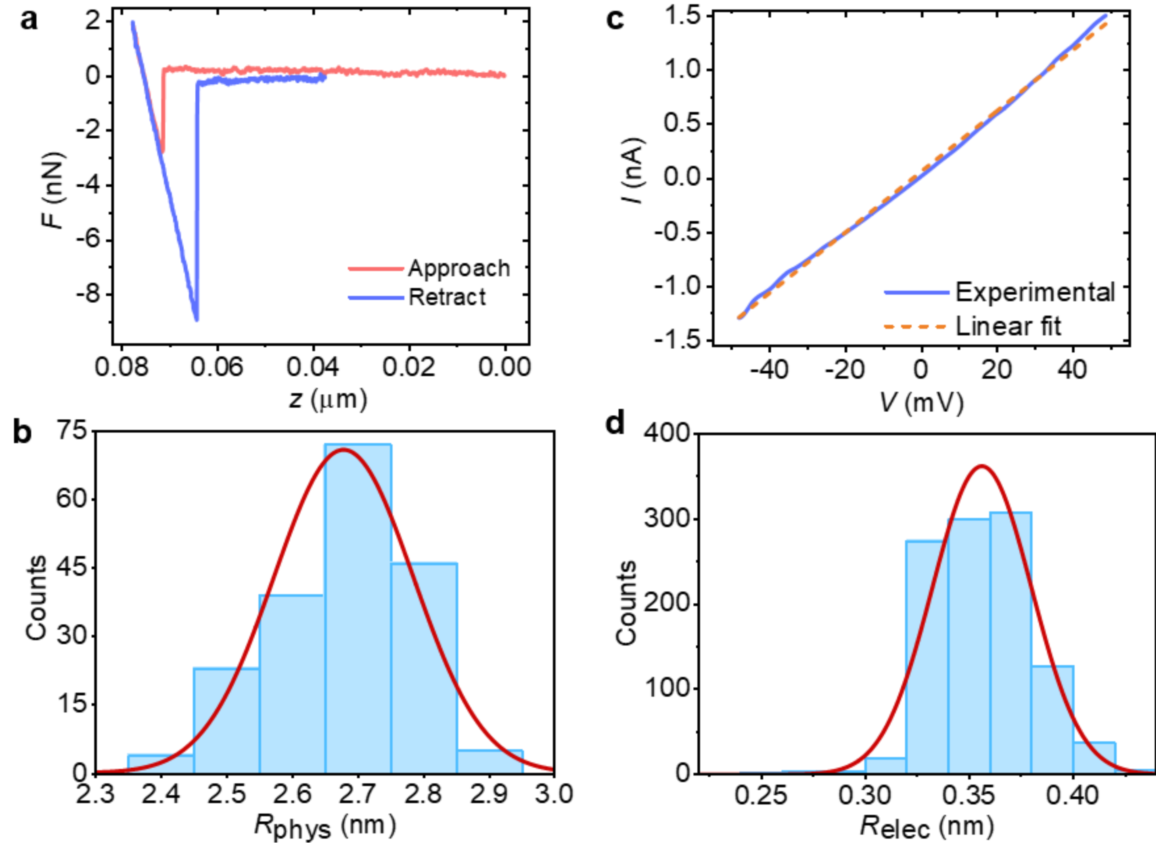

Figure 2.14: Discrepancy between physical and electrical contact areas at the tip-sample junction. (a) A representative force-distance (F-z) curve obtained with a conductive diamond tip on HOPG. The curve yields an adhesion force of ∼9.0 nN, which was plugged into the DMT contact model to estimate the physical contact radius between the tip and HOPG sample. (b) A histogram showing the distribution of the estimated physical contact radius between the tip and the HOPG sample, utilizing 189 F-d curves. (c) A representative current vs. voltage (I-V) curve (solid blue) recorded with a conductive diamond tip on HOPG. The slope of the I-V curve was extracted by a linear fit (dotted orange) of the data. (d) A histogram showing the distribution of electrical contact radius formed between the conductive diamond tip and HOPG, calculated from 1076 I-V curves using Sharvin's equation.

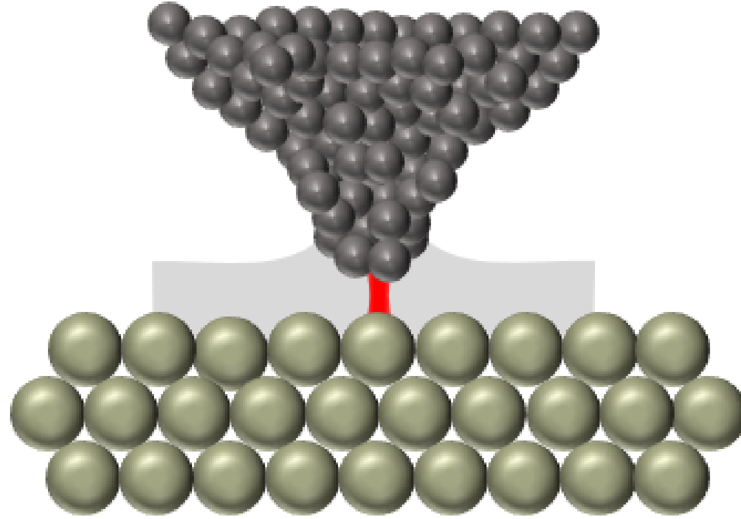

Figure 2.15: Schematic showing tunneling happening through hydrodynamic lift between tip and sample at high speed scanning, as another potential explanation behind atomic-resolution imaging capability of C-AFM.

nm (avg. ± s.d.). To estimate the electrical contact radius, we recorded 1076 *I*-*V* curves on HOPG using the same tip that was used to record Fig. 2.5(b). A representative *I*-*V* curve is shown in 2.14(c). Inverse of the slope of the linear fit to the *I*-*V* curve provides local electrical contact resistance between the tip and HOPG. The electrical contact resistance value was plugged into Equation 2.3 to estimate the electrical contact radius between the tip and the HOPG sample. Parameters used in Sharvin's equation were as follows; electrical resistivity: 9.5×10^{-11} MΩm (arithmetic average of the conductive diamond tip and HOPG), electron mean free path: 100.7 nm (arithmetic average of the conductive diamond tip and HOPG) [34, 37–39]. A histogram of the electrical contact radius values extracted from 1076 *I*-*V* curves is shown in Fig. 2.14(d). The estimated electrical contact radius was found to be 0.36 ± 0.11 nm (avg. ± s.d.) which is one order of magnitude smaller than the estimated physical contact radius. This estimation suggests the AFM tip essentially acts as an atomically sharp electrical probe as it scans on the sample surface. The related mechanism can be explained by acknowledging that AFM tips exposed to ambient conditions are often covered by a poorly conducting layer of atmospheric adsorbates and potentially a thin layer of oxide [40]. When the tip scans the sample surface under repulsive load and a bias voltage, a small portion of the poorly conducting layer may break down, resulting in a very small, electrically conductive area (*i.e.* a very sharp electrical probe) that is able to distinguish between individual atoms even though a

much larger portion of the tip is in physical contact with the sample [22, 40].

On the other hand, the discrepancy between estimated physical and electrical contact area does not explain the speed and load dependence results described earlier. Therefore, we have an alternative hypothesis that may explain those trends. Since all our measurements were performed under ambient conditions, we anticipate that the sample surfaces are covered with a thin layer of condensed water film [41]. We hypothesize that when the tip rasters over the sample surface at high speeds, hydrodynamic lift takes place between the tip and the sample as depicted by the schematic in Fig. 2.15 [42]. The confined water layer can also undergo *dynamic solidification* under high speed scanning and act as an elastic solid-like material [43]. Under such condition, upon the application of a bias, tunneling can happen through the water film. We further hypothesize that at low speeds, such hydrodynamic lift or dynamic solidification does not happen and the tip relaxes through the water film and forms a blunt contact with the sample. As a result, the atomic-resolution imaging capability degrades at low scanning speeds. This hypothesis may also explain why atomic-resolution seems to be resistant to increases in normal load, as the applied normal load has to work against the hydrodynamic lift to make the tip-sample contact blunt and degrade the image quality. This hypothesis presents promising avenues for future work aimed at exploring the mechanisms that enable atomic-resolution C-AFM imaging under ambient conditions.

2.11 Conclusions

In this chapter, we have demonstrated that C-AFM is capable of imaging surfaces with true atomic-resolution, under ambient conditions (i) without operational and instrumentational complications of STM/NC-AFM, (ii) with comparable resolution, and (iii) with the ability to decouple electronic and structural effects thanks to the separate recording of the current and topography channels. We hypothesize that atomic resolution can be enabled by either a confined, electrically conductive pathway or through a hydrodynamic lift effect at high-speed scanning.

2.12 References

[1] P De Wolf, J Snauwaert, T Clarysse, W Vandervorst, and L Hellemans. Characterization of a point-contact on silicon using force microscopy-supported resistance measurements. *Applied Physics Letters*, 66(12):1530–1532, 1995.

[2] C Shafai, D J Thomson, M Simard-Normandin, G Mattiussi, and P J Scanlon. Delineation of semiconductor doping by scanning resistance microscopy. *Applied Physics Letters*, 64(3):342–344, 1994.

[3] M P Murrell, M E Welland, S J O'Shea, T M H Wong, J R Barnes, A W McKinnon, M Heyns, and S Verhaverbeke. Spatially resolved electrical measurements of SiO_2 gate oxides using atomic force microscopy. *Applied Physics Letters*, 62(7):786–788, 1993.

[4] Y Yaish, J-Y Park, S Rosenblatt, V Sazonova, M Brink, and P L McEuen. Electrical nanoprobing of semiconducting carbon nanotubes using an atomic force microscope. *Physical Review Letters*, 92(4):046401, 2004.

[5] J-Y Park. Electrically tunable defects in metallic single-walled carbon nanotubes. *Applied Physics Letters*, 90(2):023112, 2007.

[6] Y Hattori, T Taniguchi, K Watanabe, and K Nagashio. Layer-by-layer dielectric breakdown of hexagonal boron nitride. *ACS Nano*, 9(1):916–921, 2015.

[7] J M P Alaboson, Q H Wang, J A Kellar, J Park, J W Elam, M J Pellin, and M C Hersam. Conductive atomic force microscope nanopatterning of epitaxial graphene on SiC (0001) in ambient conditions. *Advanced Materials*, 23(19):2181–2184, 2011.

[8] W Lu, L-M Wong, S Wang, and K Zeng. Effects of oxygen and moisture on the IV characteristics of TiO_2 thin films. *Journal of Materiomics*, 4(3):228–237, 2018.

[9] M T Woodside and P L McEuen. Scanned probe imaging of single-electron charge states in nanotube quantum dots. *Science*, 296(5570):1098–1101, 2002.

[10] P Birjukovs, N Petkov, J Xu, J Svirksts, J J Boland, J D Holmes, and D Erts. Electrical characterization of bismuth sulfide nanowire arrays by conductive atomic force microscopy. *The Journal of Physical Chemistry C*, 112(49):19680–19685, 2008.

[11] S V Kalinin, J Shin, S Jesse, D Geohegan, A P Baddorf, Y Lilach, M Moskovits, and A Kolmakov. Electronic transport imaging in a multiwire SnO_2 chemical field-effect transistor device. *Journal of Applied Physics*, 98(4):044503, 2005.

[12] D Erts, B Polyakov, B Daly, M A Morris, S Ellingboe, J Boland, and J D Holmes. High density germanium nanowire assemblies: contact challenges and electrical characterization. *The Journal of Physical Chemistry B*, 110(2):820–826, 2006.

[13] S J O'shea, R M Atta, and M E Welland. Characterization of tips for conducting atomic force microscopy. *Review of Scientific Instruments*, 66(3):2508–2512, 1995.

[14] J M Beebe, B Kim, J W Gadzuk, C D Frisbie, and J G Kushmerick. Transition from direct tunneling to field emission in metal-molecule-metal junctions. *Physical Review Letters*, 97(2):026801, 2006.

[15] D P E Smith, G Binnig, and C F Quate. Atomic point-contact imaging. *Applied Physics Letters*, 49(18):1166–1168, 1986.

[16] J K Gimzewski and R Möller. Transition from the tunneling regime to point contact studied using scanning tunneling microscopy. *Physical Review B*, 36(2):1284, 1987.

[17] M Enachescu, D Schleef, D F Ogletree, and M Salmeron. Integration of point-contact microscopy and atomic-force microscopy: Application to characterization of graphite/Pt (111). *Physical Review B*, 60(24):16913, 1999.

[18] C Rodenbücher, G Bihlmayer, W Speier, J Kubacki, M Wojtyniak, M Rogala, Dominik Wrana, Franciszek Krok, and K Szot. Local surface conductivity of transition metal oxides mapped with true atomic resolution. *Nanoscale*, 10(24):11498–11505, 2018.

[19] K Nowakowski, H J W Zandvliet, and P Bampoulis. Barrier inhomogeneities in atomic contacts on WS_2. *Nano Letters*, 19(2):1190–1196, 2018.

[20] J B Pethica. Comment on "Interatomic forces in scanning tunneling microscopy: Giant corrugations of the graphite surface". *Physical Review Letters*, 57(25):3235, 1986.

[21] W Frammelsberger, G Benstetter, J Kiely, and R Stamp. C-AFM-based thickness determination of thin and ultra-thin SiO_2 films by use of different conductive-coated probe tips. *Applied Surface Science*, 253(7):3615–3626, 2007.

[22] U Celano, T Hantschel, G Giammaria, R C Chintala, T Conard, H Bender, and W Vandervorst. Evaluation of the electrical contact area in contact-mode scanning probe microscopy. *Journal of Applied Physics*, 117(21):214305, 2015.

[23] P Bampoulis, K Sotthewes, M H Siekman, and H J W Zandvliet. Local conduction in $Mo_xW_{1-x}Se_2$: The role of stacking faults, defects, and alloying. *ACS Applied Materials & Interfaces*, 10(15):13218–13225, 2018.

[24] K S Novoselov, A K Geim, S V Morozov, D Jiang, Y Zhang, S V Dubonos, I V Grigorieva, and A A Firsov. Electric field effect in atomically thin carbon films. *Science*, 306(5696):666–669, 2004.

[25] S B Desai, S R Madhvapathy, A B Sachid, J P Llinas, Q Wang, G Ho Ahn, G Pitner, M J Kim, J Bokor, C Hu, et al. MoS_2 transistors with 1-nanometer gate lengths. *Science*, 354(6308):99–102, 2016.

[26] R Addou, L Colombo, and R M Wallace. Surface defects on natural MoS_2. *ACS Applied Materials & Interfaces*, 7(22):11921–11929, 2015.

[27] P Bampoulis, R van Bremen, Q Yao, B Poelsema, H J W Zandvliet, and K Sotthewes. Defect dominated charge transport and fermi level pinning in MoS_2/metal contacts. *ACS Applied Materials & Interfaces*, 9(22):19278–19286, 2017.

[28] S A Sumaiya, A Martini, and M Z Baykara. Improving the reliability of conductive atomic force microscopy-based electrical contact resistance measurements. *Nano Express*, 1(3):030023, 2020.

[29] R W Carpick, D F Ogletree, and M Salmeron. A general equation for fitting contact area and friction vs load measurements. *Journal of Colloid and Interface Science*, 211(2):395–400, 1999.

[30] P Eaton and P West. *Atomic force microscopy.* Oxford university press, 2010.

[31] M Z Baykara and U D Schwarz. Atomic force microscopy: Methods and applications. In *Encyclopedia of Spectroscopy and Spectrometry.* Elsevier, 2017.

[32] B V Derjaguin, V M Muller, and Y P Toporov. Effect of contact deformations on the adhesion of particles. *Journal of Colloid and Interface Science*, 53(2):314–326, 1975.

[33] P G Slade. *Electrical contacts: principles and applications.* CRC press, 2017.

[34] N García, P Esquinazi, J Barzola-Quiquia, B Ming, and D Spoddig. Transition from ohmic to ballistic transport in oriented graphite: Measurements and numerical simulations. *Physical Review B*, 78(3):035413, 2008.

[35] J R Eskelsen, Y Qi, S Schneider-Pollack, S Schmitt, K W Hipps, and U Mazur. Correlating elastic properties and molecular organization of an ionic organic nanostructure. *Nanoscale*, 6(1):316–327, 2014.

[36] A C Normand, A M Charrier, O Arnould, and A L Lereu. Influence of force volume indentation parameters and processing method in wood cell walls nanomechanical studies. *Scientific Reports*, 11(1):1–14, 2021.

[37] S Banerjee, M Sardar, N Gayathri, A K Tyagi, and B Raj. Conductivity landscape of highly oriented pyrolytic graphite surfaces containing ribbons and edges. *Physical Review B*, 72(7):075418, 2005.

[38] L Kogut and K Komvopoulos. Electrical contact resistance theory for conductive rough surfaces separated by a thin insulating film. *Journal of Applied Physics*, 95(2):576–585, 2004.

[39] B Sacépé, C Chapelier, C Marcenat, J Kačmarčik, T Klein, M Bernard, and E Bustarret. Tunneling spectroscopy and vortex imaging in boron-doped diamond. *Physical Review Letters*, 96(9):097006, 2006.

[40] M A Lantz, S J O'Shea, and M E Welland. Characterization of tips for conducting atomic force microscopy in ultrahigh vacuum. *Review of Scientific Instruments*, 69(4):1757–1764, 1998.

[41] C M Mate and R W Carpick. *Tribology on the small scale: a modern textbook on friction, lubrication, and wear.* Oxford University Press, USA, 2019.

[42] C C Glover, J P Killgore, and R C Tung. Scanning speed phenomenon in contact-resonance atomic force microscopy. *Beilstein Journal of Nanotechnology*, 9(1):945–952, 2018.

[43] S H Khan, G Matei, S Patil, and P M Hoffmann. Dynamic solidification in nanoconfined water films. *Physical Review Letters*, 105(10):106101, 2010.

Chapter 3

Imaging Surfaces of Different Materials under Ambient Conditions with Atomic Resolution

3.1 Introduction

Following the demonstration of the true atomic-resolution surface imaging capability of C-AFM under ambient conditions on prototypical samples such as HOPG and MoS_2 in Chapter 2, in this chapter we focus on establishing the methodology as a general one. In particular, we aim to demonstrate that the method is capable of imaging different types of surfaces with atomic-resolution, as opposed to being limited to only a few materials. Hence, we study various types of conductive material surfaces including semiconductor, semimetal, and close-packed metal surfaces. All these classes of materials play crucial roles in a multitude of scientifically and technologically important fields including but not limited to nano-scale electronic/optoelectronic device development, surface reactions, thin film coatings etc. Besides the chemical composition, atomic arrangement of the involved materials on the surface has been proved to be one of the crucial factors that determine film properties and device performance. Therefore, if one can robustly image these material surfaces with atomic-level spatial resolution directly under ambient conditions, the corresponding methodology will have important potential to be employed in variety of fields. For instance, it will allow many researchers to perform catalysis, defect chemistry, surface electronic studies in a less costly, straightforward, and more meaningful manner for applications. Motivated by this line of thought, in this chapter, we report direct, real-space, atomic-resolution images of WSe_2, WS_2 as 2D multi-element semiconductors, black phosphorus as an elemental 2D material with semiconducting properties, $PtSe_2$ as a 2D semimetal, and Au as a close-packed metal surface obtained via high speed C-AFM scanning under

ambient conditions.

3.2 Two-Dimensional Transition Metal Dichalcogenide Semiconductors

Since the isolation of graphene from its bulk form (graphite) in 2004 through the seminal work of Novoselov *et al.* [1], there has been great progress in exploring new properties and developing new applications of 2D materials. Among the different classes of 2D materials, TMDs are the most widely studied. TMDs are layered 2D materials where each layer consists of a sheet of transition metal (M) atoms sandwiched between two sheets of chalcogen (X) atoms. While strong covalent bonds exist among the atoms in each X-M-X layer, the different X-M-X layers are bonded to each other via weak van der Waals bonds. Unlike graphene, TMDs do have a bandgap and typically exhibit semiconducting properties. TMDs possess promising applications in high-end electronics, flexible electronics, photonics and energy storage due to their unique combination of excellent electronic and mechanical characteristics [2]. There are many successful demonstrations of novel electronic devices using semiconducting TMDs [3–5]. The performance of these devices are heavily determined by the charge carrier mobility. Even though the theoretically reported charge mobility of 2D semiconducting TMDs are very promising [6, 7], in reality the mobility is often affected negatively to a great extent by the presence of defects and disorder. Therefore, atomic-scale studies of these semiconducting TMDs to probe the types, density, and electronic effects of defects is crucial. TMDs are also a promising platform to study exotic physical phenomena; for instance, some of the group V TMDs have exhibited charge density wave (CDW) states in both bulk and monolayer form [8, 9]. Furthermore, some of these TMDs also exhibit superconducting properties [10]. SPM techniques are heavily used to study these properties [11, 12]. Other than the significance of 2D TMDs as individual materials, there is a strong focus in the scientific community nowadays to develop heterostructures by stacking different TMDs together [13]. Different heterostructures have been reported to exhibit unique electronic/photonic characteristics and can be tailored towards targeted applications [14]. SPM techniques are also widely employed to study these heterostructures, in particular to study the Moiré patterns generated a result of vertical stacking [15, 16].

In Chapter 2, we have demonstrated the true atomic-resolution imaging capability of C-AFM on a 2D TMD semiconductor, MoS_2. In order to demonstrate that C-AFM is capable of imaging 2D TMD semiconductors in general, we imaged more materials of the same class, such as WSe_2 and WS_2. Both these materials have exhibited thickness-dependent electronic properties and have potential applications in electronics and optoelectronics [17]. Both these materials were sourced from the

same company as for MoS_2 and were prepared for C-AFM measurements following the same methodology described in Section 2.3.

3.2.1 WSe_2

WSe_2 is a promising 2D semiconductor from the family of TMDs. Similar to MoS_2, WSe_2 also exhibits drastically different properties when thinned from bulk to monolayer. In the bulk form, WSe_2 has an indirect bandgap of ∼1.2 eV. However, the monolayer WSe_2 has a direct bandgap of ∼1.6 eV. Exfoliated WSe_2 has been used to fabricate a variety of electronic and optoelectronic devices such as field effect transistors, photodetectors, light emitting diodes, photovoltaic devices etc. [18, 19]. The most thermodynamically stable phase of WSe_2 is the 2H (trigonal prismatic) polytype which corresponds to a hexagonal lattice structure as shown in Fig.3.1(a). The 2H phase corresponds to an ABA stacking in which the Se atoms in different atomic planes occupy the same positions and are located on top of each other in the direction perpendicular to the layer. Addou *et al.* studied the topography and electronic properties of both exfoliated and chemical vapor deposited WSe_2 by means of STM under pristine UHV conditions [20]. Such studies not only reveal the surface electronic landscape of WSe_2, but also provide important insight regarding bottom-up synthesis of the material which in turn can be used as feedback to fine-tune the synthesis procedure. In this context, we attempted to image WSe_2 directly under ambient conditions following our high-speed C-AFM methodology. Fig. 3.1(b) shows a current image recorded on WSe_2 (001) exhibiting a defect free area with atomic-resolution. The corresponding FT of the current image is shown in Fig. 3.1(c). The FT corresponds to an average periodicity of 3.2 Å. The average periodicity was calculated by taking into account the periodicities found along the three symmetry directions. We notice some discrepancy between the measured and expected periodicity which can be caused by thermal drift (considering we are working under ambient conditions), piezo creep or tip asymmetry [21]. Previously, STM studies performed under UHV have been proven to be an effective and valid way to explore dopant distribution on WSe_2 surfaces [22]. With the C-AFM methodology, one can now perform similar studies directly under ambient conditions, without the requirement of costly and complicated vacuum equipment.

3.2.2 WS_2

WS_2 is another remarkable tungsten based 2D TMD semiconductor that exhibits high in-plane carrier mobility and electrostatic modulation of conductance [23]. It also exhibit distinctive properties such as strong spin-orbit coupling [24], tunable light-matter interaction [25], enhanced Coulomb interaction [26], many-body effects [27] and so on. WS_2 also exhibits lower defect density compared to other 2D TMD

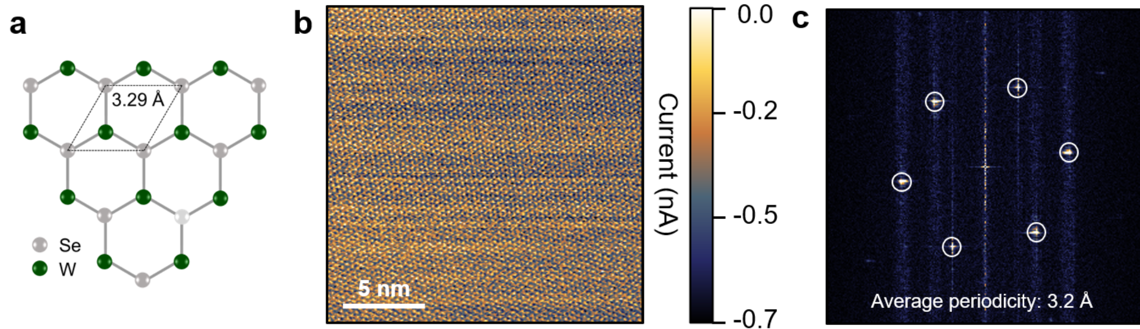

Figure 3.1: (a) Atomic model of the WSe_2 (001) surface. (b) Current image recorded on WSe_2 via C-AFM under ambient conditions showing the atomic-scale crystal structure. (c) The Fourier Transform (FT) of the current map shown in (b) that corresponds to an average periodicity of 3.2 Å.

semiconductors [26]. As such, WS_2 is a preferred candidate for photoelectronic devices such as light emitters, photodetectors etc. Before the isolation of monolayer, thin films of WS_2 were studied to be used as active absorbing layers in thin film solar cells [28]. Similar to MoS_2 and WSe_2, WS_2 also manifests a transition from indirect to direct bandgap upon its isolation from bulk to monolayer. The most stable phase of WS_2 has a similar crystal structure to that of WSe_2 *i.e.* the 2H polytype with a slightly lower lattice periodicity of 3.18 Å. An atomic model of WS_2 (001) surface is shown in Fig. 3.2(a). Studies of WS_2 (001) surface with high spatial resolution, in particular via STM under UHV, allowed the exploration of the effect of individual dopants on the conductivity landscape [22]. Atomic-level adsorption of Sn atoms on WS_2 were also studied via STM [29]. Our measurements demonstrate that the WS_2 surface can now be studied with atomic-level spatial resolution directly under ambient conditions via high speed C-AFM scanning which in turn facilitates the opportunity to study defects, dopants, impurities, and dynamic changes on WS_2 surface directly under ambient conditions. Fig. 3.2(b) shows a current image recorded on WS_2 under ambient conditions. It shows a defect free area on WS_2 with atomically-resolved crystal structure. The corresponding FT shown in Fig. 3.2(c) verifies that the measured lattice periodicity matches quite well with the expected periodicity.

3.3 Two-Dimensional Elemental Semiconductor

Unlike graphene, TMDs are multi-element 2D materials. Similar to graphene, black phosphorus (BP) is an elemental 2D material. However, unlike graphene, BP has an intrinsic bandgap of $\sim$0.3 eV in its thin film form which makes it a semicon-

ductor [30]. The moderate bandgap of BP also bridges the gap between graphene that has zero bandgap and TMDs that have relatively large bandgaps. As such, it allows the fabrication of transistors using BP with high on-off current ratios and high mobilities [31]. Other than electronic applications, BP is also a suitable candidate for solid lubrication [32] and as such, its atomic-scale friction characteristic are studied via SPM-based techniques. Riffle *et al.* studied the effect of defects such as vacancies on the conductivity landscape of BP via STM under UHV [33]. One of the major challenges of studying BP is that it is highly air-sensitive and oxidizes rapidly under ambient exposure. As a result, the majority of atomic-scale studies of BP are typically performed under UHV environment [34]. Considering its emerging significance in the scientific research, we imaged BP with our high-speed C-AFM methodology. Towards this purpose, bulk BP was sourced from the company 2D Semiconductors, and few-layer thick BP flakes were exfoliated in air on Au covered Si/SiO_2 substrates following the same methodology as described in Section 2.3. However, considering the fact that BP degrades rapidly under ambient conditions, the C-AFM measurements were performed under dry N_2 environment to slow down the degradation. Nevertheless, such flow of N_2 does not completely rule out the presence of some air inside the AFM chamber.

BP has an orthorhomic crystal structure with a puckered honeycomb lattice as shown in Fig. 3.3(a) and (b). The puckered structure incorporates mechanical and electronic anisotropy into the BP lattice. Similar to the 2D TMDs, BP has strong in-plane bonds among the atoms and weak van der Waals bonds between the layers. A current map recorded on BP via C-AFM under N_2 flow is shown in Fig. 3.3(c). The current map features alternate columns of crests and troughs in the form of current maxima and minima. The current map also features two defective locations. The corresponding FT shown in Fig. 3.3(d) confirms that we are able to image the top-most phosphorus atoms of the puckered BP lattice highlighted as dark blue spheres in the atomic models in Fig. 3.3(a) and (b). It is also worth noting that we were able to image atomic-scale crystal structure of BP within the relatively short period of time (roughly 3 hours) before it degrades. Since BP is hydrophillic [31], our results demonstrate that we are able to image both hydrophobic (*e.g.* HOPG) and hydrophicllic 2D material surfaces with our C-AFM methodology.

3.4 Two-Dimensional Semimetal

Group-10 noble transition metal chalcogenides (NTMDCs) have recently attracted particular attention because of their electronic properties such as carrier mobility in the intermediate regime between metals and semiconductors; they are thus regarded as semimetals [35]. Their electronic properties are widely tunable comparted to TMD semiconductors and they exhibit excellent air stability. They have stimulated appli-

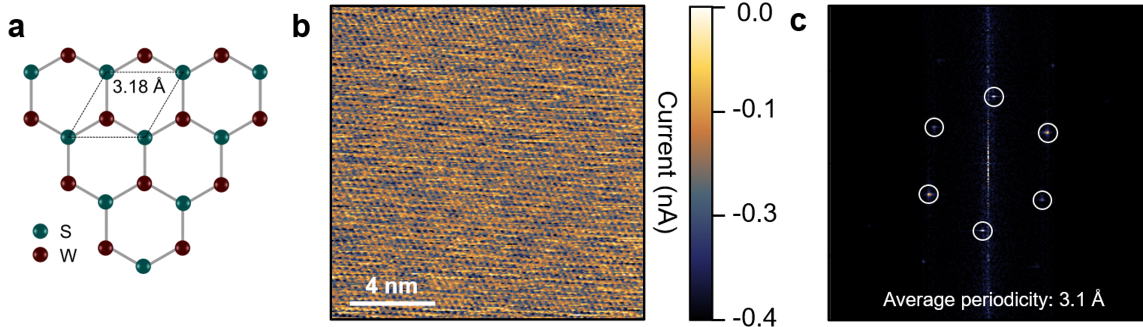

Figure 3.2: (a) Atomic model of the WS_2 (001) surface. (b) Current image recorded on WS_2 via C-AFM under ambient conditions showing the atomic level crystal structure. (c) The FT of the current map in (b) that corresponds to an average periodicity of 3.1 Å.

cations in the fields of electronics, optoelectronics, catalysis, sensors etc. As such, investigating these materials at the atomic scale holds crucial scientific importance. One material from this category that is widely studied is $PtSe_2$. For instance, Zheng *et al.* studied various types of point defects of the 1T-$PtSe_2$ and their corresponding local density of states via STM under UHV environment and at a temperature of 77 K [36]. Wang *et al.* studied the atomic-structure of an epitaxially-grown monolayer $PtSe_2$ on Pt(111) [37]. Tong *et al.* also employed low temperature STM to study the atomic structure of $PtSe_2$ grown via an alternative approach, in particular, via direct selenization of Pt(111) by liquid phase immersion in a Na_2Se solution, followed by annealing under UHV. They observed that depending on variations in annealing treatment, the $PtSe_2$ film can undergo different types of phase transition on the atomic-scale [38]. These reports suggest that true atomic-resolution imaging of $PtSe_2$ via C-AFM could prove the applicability of the method for not only cutting-edge electronic materials research but also understanding and/or fine-tuning bottom-up synthesis of this material. Motivated as such, we imaged few-layers-thick samples of $PtSe_2$ via C-AFM with atomic-resolution under ambient conditions. Towards this purpose, bulk $PtSe_2$ was sourced from the company 2D Semiconductors. Few-layer-thick $PtSe_2$ flakes were exfoliated on Au covered Si/SiO_2 substrates following the same methodology described in Section 2.3. It is worth noting that while monolayer $PtSe_2$ is semiconducting, few-layer $PtSe_2$ is semimetal in nature. Fig. 3.4(a) shows an atomic model of 1T-$PtSe_2$ (001) surface that has a lattice periodicity of 3.7 Å. A current image recorded on $PtSe_2$ via C-AFM under ambient conditions is shown in Fig. 3.4(b). Considering only one contrast in the form of current maxima is apparent in the current image, we conclude that in this image we most likely observe the top

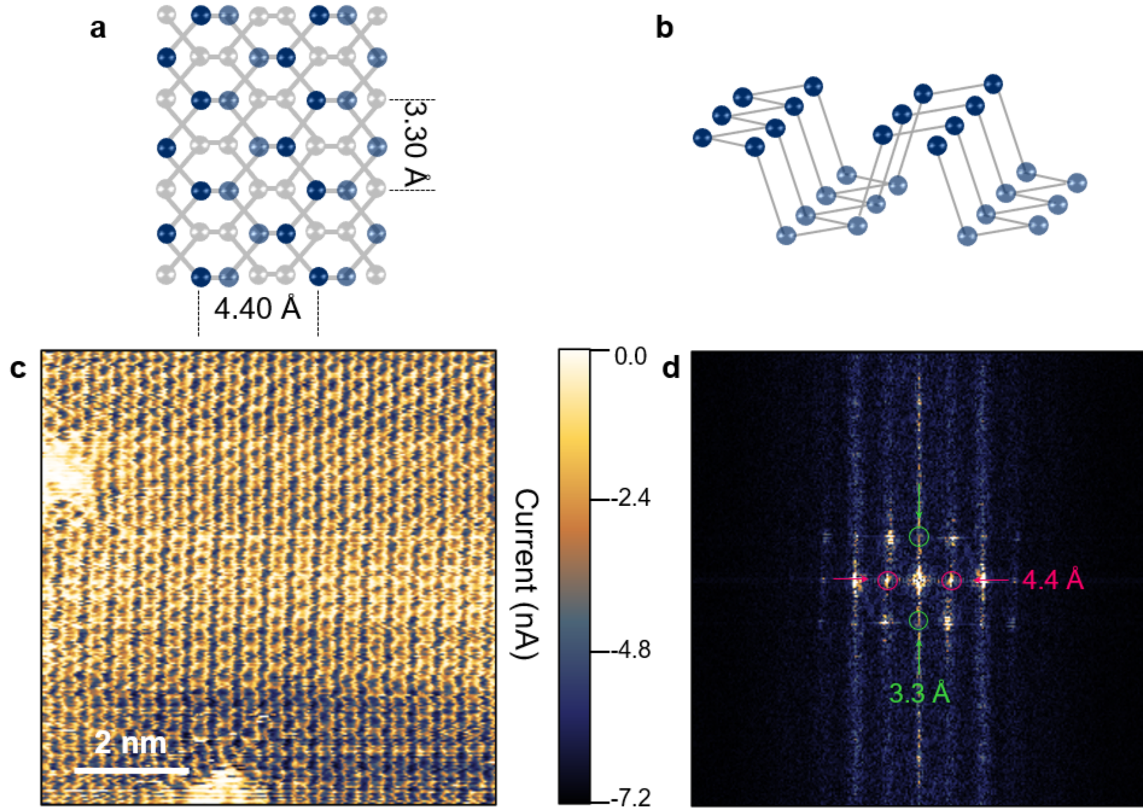

Figure 3.3: (a) Atomic model of the black phosphorus (BP) (001) surface. (b) Isometric projection of the puckered crystal structure of BP. (c) Current image recorded on BP via C-AFM under N_2 flow that was initiated after the sample was inserted inside the AFM chamber, following the exfoliation in air. The current image shows alternate columns of crests and troughs in the form of current maxima and minima. Two defective regions, at the edges of the image, are also observed. (d) The corresponding FT of the current map shown in (c). The periodicities calculated from the FT verify that the current map captures the atomic arrangement of the top most phosphorus atoms of the puckered BP lattice as represented by the dark blue spheres in the atomic models (a) and (b).

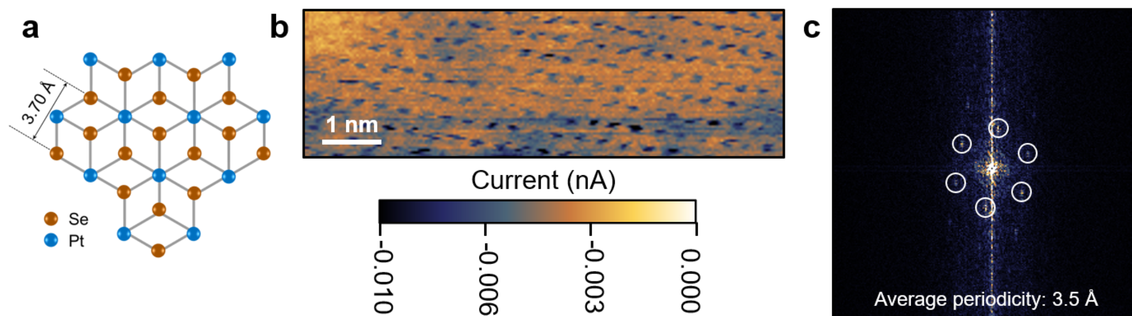

Figure 3.4: (a) Atomic model of the $PtSe_2$ (001) surface. (b) Current image recorded on $PtSe_2$ via C-AFM under ambient conditions showing the atomic-scale crystal structure. (c) The FT of the current map in (b) that corresponds to an average periodicity of 3.5 Å.

Se atoms of the $PtSe_2$ crystal. The corresponding FT of the current image is shown in Fig. 3.4(c) which suggests that we have ∼5% discrepancy between the measured and expected periodicity. As mentioned earlier, this discrepancy can be caused by thermal drift, piezo creep, tip asymmetry etc.

3.5 Metal

Successfully imaging close-packed metal surfaces and related surface reconstructions would strengthen the argument for C-AFM as an ideal tool for atomic-resolution imaging, as the imaging of such surfaces is challenging via methods such as NC-AFM, even under well-controlled UHV conditions [39]. As such, we aim to image a prototypical metal surface, Au(111), which is of particular interest in surface science due to its potential in catalysis and other applications [40]. The Au(111) surface has been extensively studied via both STM and NC-AFM. An STM study performed by Smith *et al.* first revealed the atomic structure of Au(111) [41]. Later on, the work of Barth *et al.* revealed the herringbone reconstruction of the Au(111) surface via STM [42]. The interaction of Au(111) with molecules has also been extensively studied. In particular, deposition of a variety of self-assembled monolayers on Au(111) have been investigated via SPM with high spatial resolution [43–45].

To perform the C-AFM measurements, we utilized commercially available ultra-flat Au films deposited on silicon (Platypus Technologies). Silver paint was applied to bridge the Au film with the conductive specimen holder. It is worth noting that compared to the 2D materials imaged so far in Chapters 2 and 3, the Au surface has a much higher degree of roughness. For instance, a topographic image recorded

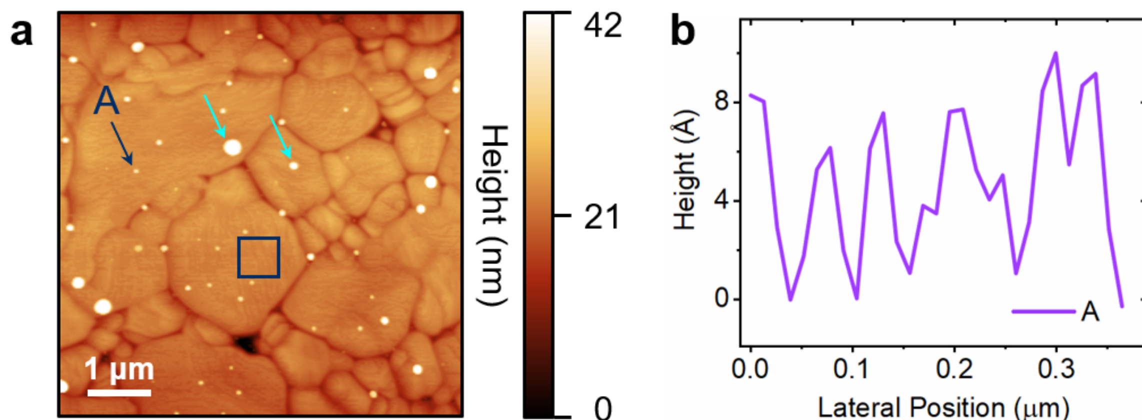

Figure 3.5: (a) A micron-scale topographic image recorded on the Au(111) surface showing the rough and grainy structure of the surface. The root mean square (RMS) roughness of the area highlighted by the blue rectangle is ∼6 Å. (b) Line profile drawn along the direction A shown in (a) by blue arrow. The cyan arrows point towards accumulation of contamination on the Au(111) surface upon extended exposure to ambient conditions.

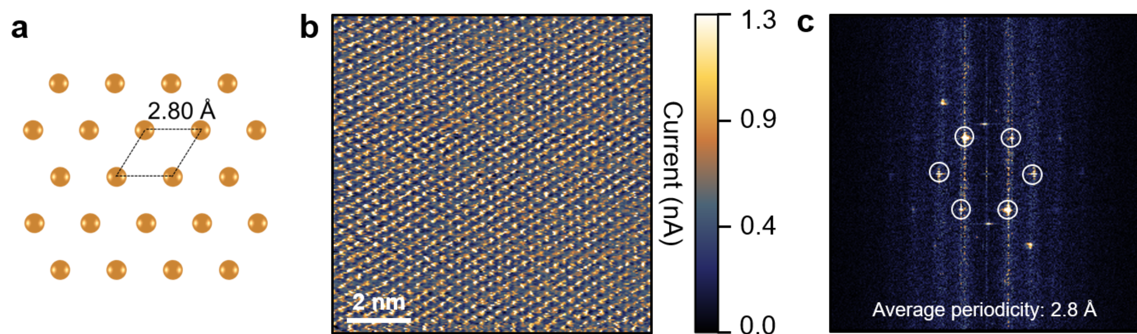

Figure 3.6: (a) Atomic model of the Au(111) surface.(b) Current image recorded on Au via C-AFM under ambient conditions showing the atomic level crystal structure. (c) The FT of the current map shown in (b) that corresponds to an average periodicity of 2.8 Å.

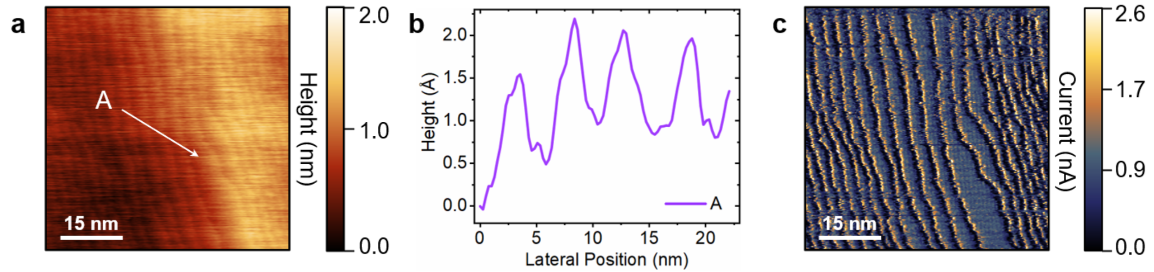

Figure 3.7: (a) A relatively large scale topography map recorded on the Au(111) surface showing stripe-like features. (b) Line profile drawn along the direction A shown in (a). The line profile assigns a height of ∼1 Å to the stripe-like features in (a). (c) The corresponding current map recorded simultaneously with (a). The current map also exhibit similar features as that of (a) but with better resolution.

on Au(111) surface is shown in Fig. 3.5(a) that shows the rough and grainy nature of the surface. The area highlighted by the blue rectangle features a root mean square (RMS) roughness value of ∼6 Å. Additionally, a line profile drawn along the blue arrow A as shown in Fig. 3.5(b) reveals the highly corrugated nature of the Au surface. It is also worth noting that the bright features highlighted by cyan arrows in Fig. 3.5(a) most likely represent accumulated contamination on the Au surface due to extended atmospheric exposure [46]. An atomic model of the Au(111) surface is shown in Fig. 3.6(a). An atomic-resolution current image recorded on the Au(111) via C-AFM under ambient conditions is shown in 3.6(b) that exhibit a homogeneous conductivity landscape. The corresponding FT of the current image is shown in Fig. 3.6(c) verifying good agreement between the measured and expected lattice periodicities. The absence of the herringbone reconstruction of Au(111) in Fig. 3.6(b) can mean that the vertical resolution of our system in that particular measurement was not good enough to capture those subtle surface features. On the other hand, when we image a relatively large area in another experimental run, we see some interesting features. For instance, the ∼60 × 60 nm topographic image of Au(111) shown in Fig. 3.7(a) exhibits some stripe-like features. A line profile drawn along the direction A as shown in Fig. 3.7(b) shows that the height of the stripe-like features is ∼1 Å which rules out the potential origin of these features as atomic step edges. On the other hand, the corresponding current map shown in Fig. 3.7(c) exhibits these features but with much higher resolution. There is a discrepancy between the measured corrugations in our work (∼1 Å) and those from UHV-STM experiments (∼0.3 Å) in the literature [47]. This discrepancy may arise from the fact that STM images are convolutions of topography and electronic effects; which we don't have in our topography channel in C-AFM. Following such comparison,

we tentatively assign these features to the herringbone reconstruction, although a definitive conclusion would require the collection of more data.

3.6 Conclusions

In this Chapter, we have demonstrated that high-speed C-AFM scanning can resolve the atomic-scale crystal structure of a variety of conductive material surfaces, directly under ambient conditions. Results reported in this chapter further demonstrate that high-speed C-AFM is capable of imaging not only hydrophillic and hydrophobic surfaces, but also atomically flat (*e.g.* TMDs) as well as grainy, rough (*e.g.* Au) surfaces with atomic-resolution. The capabilities outlined in this Chapter lead to promising avenues for studying the effects of defects on the surface conductivity landscape and dynamic surface changes of scientifically and technologically important materials, directly under ambient conditions.

3.7 References

[1] K S Novoselov, A K Geim, S V Morozov, D Jiang, Y Zhang, S V Dubonos, I V Grigorieva, and A A Firsov. Electric field effect in atomically thin carbon films. *Science*, 306(5696):666–669, 2004.

[2] S Manzeli, D Ovchinnikov, D Pasquier, O V Yazyev, and A Kis. 2d transition metal dichalcogenides. *Nature Reviews Materials*, 2(8):1–15, 2017.

[3] B Radisavljevic, A Radenovic, J Brivio, V Giacometti, and A Kis. Single-layer MoS_2 transistors. *Nature Nanotechnology*, 6(3):147–150, 2011.

[4] D Ovchinnikov, A Allain, Y-S Huang, D Dumcenco, and A Kis. Electrical transport properties of single-layer WS_2. *ACS Nano*, 8(8):8174–8181, 2014.

[5] D Krasnozhon, D Lembke, C Nyffeler, Y Leblebici, and A Kis. MoS_2 transistors operating at gigahertz frequencies. *Nano Letters*, 14(10):5905–5911, 2014.

[6] K Kaasbjerg, K S Thygesen, and K W Jacobsen. Phonon-limited mobility in n-type single-layer MoS_2 from first principles. *Physical Review B*, 85(11):115317, 2012.

[7] W Zhang, Z Huang, W Zhang, and Y Li. Two-dimensional semiconductors with possible high room temperature mobility. *Nano Research*, 7(12):1731–1737, 2014.

[8] X Xi, L Zhao, Z Wang, H Berger, L Forró, Jie Shan, and K F Mak. Strongly enhanced charge-density-wave order in monolayer $NbSe_2$. *Nature Nanotechnology*, 10(9):765–769, 2015.

[9] C-S Lian, C Si, and W Duan. Unveiling charge-density wave, superconductivity, and their competitive nature in two-dimensional $NbSe_2$. *Nano Letters*, 18(5):2924–2929, 2018.

[10] B Sipos, A F Kusmartseva, A Akrap, H Berger, L Forró, and E Tutiš. From Mott state to superconductivity in 1T-TaS_2. *Nature Materials*, 7(12):960–965, 2008.

[11] M M Ugeda, A J Bradley, Y Zhang, S Onishi, Y Chen, W Ruan, C Ojeda-Aristizabal, H Ryu, M T Edmonds, H-Z Tsai, et al. Characterization of collective ground states in single-layer $NbSe_2$. *Nature Physics*, 12(1):92–97, 2016.

[12] I Guillamón, H Suderow, S Vieira, L Cario, P Diener, and P Rodiere. Superconducting density of states and vortex cores of 2H-NbS_2. *Physical Review Letters*, 101(16):166407, 2008.

[13] K E Aretouli, D Tsoutsou, P Tsipas, J Marquez-Velasco, S Aminalragia Giamini, N Kelaidis, V Psycharis, and A Dimoulas. Epitaxial 2D $SnSe_2$/2D WSe_2 van der waals heterostructures. *ACS Applied Materials & Interfaces*, 8(35):23222–23229, 2016.

[14] Q Zeng and Z Liu. Novel optoelectronic devices: transition-metal-dichalcogenide-based 2D heterostructures. *Advanced Electronic Materials*, 4(2):1700335, 2018.

[15] H M Hill, A F Rigosi, K T Rim, G W Flynn, and T F Heinz. Band alignment in MoS_2/WS_2 transition metal dichalcogenide heterostructures probed by scanning tunneling microscopy and spectroscopy. *Nano Letters*, 16(8):4831–4837, 2016.

[16] D M Kennes, M Claassen, L Xian, A Georges, A J Millis, J Hone, C R Dean, D N Basov, A N Pasupathy, and A Rubio. Moiré heterostructures as a condensed-matter quantum simulator. *Nature Physics*, 17(2):155–163, 2021.

[17] G R Bhimanapati, Z Lin, V Meunier, Y Jung, J Cha, S Das, D Xiao, Y Son, M S Strano, V R Cooper, et al. Recent advances in two-dimensional materials beyond graphene. *ACS Nano*, 9(12):11509–11539, 2015.

[18] J-K Huang, J Pu, C-L Hsu, M-H Chiu, Z-Y Juang, Y-H Chang, W-H Chang, Y Iwasa, T Takenobu, and L-J Li. Large-area synthesis of highly crystalline WSe_2 monolayers and device applications. *ACS Nano*, 8(1):923–930, 2014.

[19] D J Groenendijk, M Buscema, G A Steele, S Michaelis de Vasconcellos, R Bratschitsch, H S J van der Zant, and A Castellanos-Gomez. Photovoltaic and photothermoelectric effect in a double-gated WSe_2 device. *Nano Letters*, 14(10):5846–5852, 2014.

[20] R Addou and R M Wallace. Surface analysis of WSe_2 crystals: spatial and electronic variability. *ACS Applied Materials & Interfaces*, 8(39):26400–26406, 2016.

[21] M Z Baykara and U D Schwarz. Atomic force microscopy: Methods and applications. In *Encyclopedia of Spectroscopy and Spectrometry*. Elsevier, 2017.

[22] T W Matthes, C Sommerhalter, A Rettenberger, P Bruker, J Boneberg, M C Lux-Steiner, and P Leiderer. Imaging of dopants in surface and sub-surface layers of the transition metal dichalcogenides WS_2 and WSe_2 by scanning tunneling microscopy. *Applied Physics A*, 66(1):1007–1011, 1998.

[23] W Zhao, Z Ghorannevis, L Chu, M Toh, C Kloc, P-H Tan, and G Eda. Evolution of electronic structure in atomically thin sheets of uppercaseWS_2 and WSe_2. *ACS Nano*, 7(1):791–797, 2013.

[24] Z Y Zhu, Y C Cheng, and U Schwingenschlögl. Giant spin-orbit-induced spin splitting in two-dimensional transition-metal dichalcogenide semiconductors. *Physical Review B*, 84(15):153402, 2011.

[25] J Kern, A Trügler, I Niehues, J Ewering, R Schmidt, R Schneider, S Najmaei, A George, J Zhang, J Lou, et al. Nanoantenna-enhanced light–matter interaction in atomically thin WSe_2. *ACS Photonics*, 2(9):1260–1265, 2015.

[26] L Yuan and L Huang. Exciton dynamics and annihilation in WS_2 2D semiconductors. *Nanoscale*, 7(16):7402–7408, 2015.

[27] L Wang, A Kutana, and B I Yakobson. Many-body and spin-orbit effects on direct-indirect band gap transition of strained monolayer MoS_2 and WS_2. *Annalen der Physik*, 526(9-10):L7–L12, 2014.

[28] C Ballif, M Regula, and F Levy. Optical and electrical properties of semiconducting WS_2 thin films: From macroscopic to local probe measurements. *Solar Energy Materials and Solar Cells*, 57(2):189–207, 1999.

[29] M Mohan, V K Singh, S Reshmi, S Roy Barman, and K Bhattacharjee. Adsorption of Sn on UHV cleaved WS_2 surface: Signature of nearly commensurate growth. In *AIP Conference Proceedings*, volume 2265, page 030405. AIP Publishing LLC, 2020.

[30] X Ling, H Wang, S Huang, F Xia, and M S Dresselhaus. The renaissance of black phosphorus. *Proceedings of the National Academy of Sciences*, 112(15):4523–4530, 2015.

[31] A Castellanos-Gomez, L Vicarelli, E Prada, J O Island, K L Narasimha-Acharya, S I Blanter, D J Groenendijk, M Buscema, G A Steele, J V Alvarez, et al. Isolation and characterization of few-layer black phosphorus. *2D Materials*, 1(2):025001, 2014.

[32] Y Zhang, D Zhang, Y Wang, Q Liu, Q Li, and M Dong. Atomic-scale friction of black and violet phosphorus crystals: implications for phosphorus-based devices and lubricants. *ACS Applied Nano Materials*, 4(9):9932–9937, 2021.

[33] J V Riffle, C Flynn, B St. Laurent, C A Ayotte, C A Caputo, and S M Hollen. Impact of vacancies on electronic properties of black phosphorus probed by STM. *Journal of Applied Physics*, 123(4):044301, 2018.

[34] A Kumar, F Telesio, S Forti, A Al-Temimy, C Coletti, M Serrano-Ruiz, M Caporali, M Peruzzini, F Beltram, and S Heun. STM study of exfoliated few layer black phosphorus annealed in ultrahigh vacuum. *2D Materials*, 6(1):015005, 2018.

[35] L Pi, L Li, K Liu, Q Zhang, H Li, and T Zhai. Recent progress on 2D noble-transition-metal dichalcogenides. *Advanced Functional Materials*, 29(51):1904932, 2019.

[36] H Zheng, Y Choi, F Baniasadi, D Hu, L Jiao, K Park, and C Tao. Visualization of point defects in ultrathin layered 1T-$PtSe_2$. *2D Materials*, 6(4):041005, 2019.

[37] Y Wang, L Li, W Yao, S Song, J T Sun, J Pan, X Ren, C Li, Ei Okunishi, Y-Q Wang, et al. Monolayer $PtSe_2$, a new semiconducting transition-metal-dichalcogenide, epitaxially grown by direct selenization of Pt. *Nano Letters*, 15(6):4013–4018, 2015.

[38] Y Tong, M Bouaziz, H Oughaddou, H Enriquez, K Chaouchi, F Nicolas, S Kubsky, V Esaulov, and A Bendounan. Phase transition and thermal stability of epitaxial $PtSe_2$ nanolayer on Pt(111). *RSC Advances*, 10(51):30934–30943, 2020.

[39] H Mönig. Copper-oxide tip functionalization for submolecular atomic force microscopy. *Chemical Communications*, 54(71):9874–9888, 2018.

[40] R Meyer, Lemire, S K Shaikhutdinov, and H-J Freund. Surface chemistry of catalysis by gold. *Gold Bulletin*, 37(1):72–124, 2004.

[41] D P E Smith, G Binnig, and C F Quate. Atomic point-contact imaging. *Applied Physics Letters*, 49(18):1166–1168, 1986.

[42] J V Barth, H Brune, G Ertl, and R J Behm. Scanning tunneling microscopy observations on the reconstructed Au(111) surface: Atomic structure, long-range superstructure, rotational domains, and surface defects. *Physical Review B*, 42(15):9307, 1990.

[43] T Fukuma, K Kobayashi, T Horiuchi, H Yamada, and K Matsushige. Alkanethiol self-assembled monolayers on Au(111) surfaces investigated by non-contact AFM. *Applied Physics A*, 72(1):S109–S112, 2001.

[44] K Biswas, J I Urgel, K Xu, J Ma, A Sánchez-Grande, P Mutombo, A Gallardo, K Lauwaet, B Mallada, B de la Torre, et al. On-surface synthesis of a dicationic diazahexabenzocoronene derivative on the Au(111) surface. *Angewandte Chemie*, 133(48):25755–25760, 2021.

[45] S Clair, S Pons, A P Seitsonen, H Brune, K Kern, and J V Barth. STM study of terephthalic acid self-assembly on Au(111): Hydrogen-bonded sheets on an inhomogeneous substrate. *The Journal of Physical Chemistry B*, 108(38):14585–14590, 2004.

[46] N Turetta, F Sedona, A Liscio, M Sambi, and P Samorì. Au(111) surface contamination in ambient conditions: Unravelling the dynamics of the work function in air. *Advanced Materials Interfaces*, 8(10):2100068, 2021.

[47] Pk Han, B A Mantooth, E C H Sykes, Z J Donhauser, and Paul S Weiss. Benzene on Au{111} at 4 K: Monolayer growth and tip-induced molecular cascades. *Journal of the American Chemical Society*, 126(34):10787–10793, 2004.

Chapter 4

Atomically-Resolved Defects and Disorder

4.1 Introduction

Atomic-scale defects play a crucial role in a multitude of scientific fields. For example, channel length of most modern semiconductor devices is only a few nanometers wide. The presence of defects in the semiconductor crystals used in these devices can drastically alter carrier mobility, carrier lifetime etc. and thereby, affect the device performance to a great extent [1, 2]. Point defects present in semiconductor crystals can act as scattering source or trap charges, and result in lower than expected carrier mobility. On the other hand, defects present in the substrate can heavily influence growth of crystals or thin films by acting as nucleation sites [3, 4]. Furthermore, a great amount of scientific efforts have been dedicated towards bottom-up synthesis of different types of 2D materials. Defects such as vacancies or impurity atoms in these 2D crystals can act as acceptors or donors and affect the applications for which these crystals are being developed [5]. In fact, due to the electron transport confinement in 2D, the electronic structure of defects in 2D materials play a much more pronounced role compared to their bulk counterpart. Moreover, knowledge of defect distribution and role can provide important insights to synthesize materials with tailored defect configuration by way of "defect engineering". Therefore, it is of utmost importance to study the quality of these materials in terms of identifying defects and associated characteristics such as their density as well as the extent of their influence on the electronic landscape. As such, one of the major applications of atomic-resolution imaging is to study atomic-scale defects and disorder. Motivated in this fashion, in this chapter we demonstrate the imaging of a variety of atomic-scale defects on different types of material surfaces via high-speed C-AFM scanning under ambient conditions. Going beyond imaging, we also demonstrate the capability of *in*

situ electronic *i.e.* charge state manipulation of defects on MoS_2.

4.2 A Variety of Defects on Different TMD Surfaces

At first, we focused on imaging defects on MoS_2 which is the most widely studied TMD for its promising applications in electronics and optoelectronics. We have already presented images showing defects such as single S vacancies and clusters of S vacancies on MoS_2 in Chapter 2 (see Fig. 2.6(c) and (d)). Here, we report additional types of defects on MoS_2 as summarized in Fig. 4.1. In particular, Fig. 4.1(a) shows an atomically resolved large-scale (23.75×23.75 nm^2) current image on MoS_2 that exhibits concentrated dark defects (indicated by the blue arrow) as well as diffuse, large-area bright (indicated by pink and white arrows) and dark defects (indicated by the green arrow) that extend over a few nanometers. The contrast seen in such current maps can be associated with localized variations in the density of states (DOS) and/or charged regions [6–8]. This image additionally demonstrates that we are routinely able to image areas of several 100 nm^2 with atomic resolution, a feat that is challenging to perform with methods such as NC-AFM. An enlargement on the type of defects indicated by the blue arrow in Fig. 4.1(a) reveals multiple atomic vacancies (similar to the case in 2.6(c)). Fig. 4.1(b) shows an enlarged image on the diffuse defects in Fig. 4.1(a). The uninterrupted continuation of the lattice structure over these extended defects indicates that their physical origin likely lies in the subsurface region: *e.g.*, in the form of subsurface Mo vacancies or substitutionals [9]. We also observe individual faint dark spots, as highlighted by the pink dashed circle in Fig. 4.1(c), in contrast to regular dark spots highlighted by the blue dashed circle. Due to the fact that these defects are concentrated to single atomic sites but provide a relatively weaker contrast in current, we attribute them to subsurface S vacancies [9, 10], demonstrating that our approach can detect minute disturbances in the atomic structure, even below the surface. Finally, another extended type of defect is shown in 4.1(d) with a lateral span of $\sim$6 nm. This defect features a bright region surrounded by a dark region, corresponding to enhanced and attenuated conductivities, respectively. These may be caused by local charging due to defects in the subsurface or generated during imaging due to local band bending by Coulomb repulsion [11]. It is crucial to note that all defects observed here on MoS_2 were imaged earlier with STM, under UHV conditions [11]. Our results, which provide comparable images, now prove that it is indeed possible to conduct atomic-resolution studies of defects in a 2D semiconductor such as MoS_2 simply by employing C-AFM under ambient conditions.

We are also able to image different types of defects on other TMD surfaces as

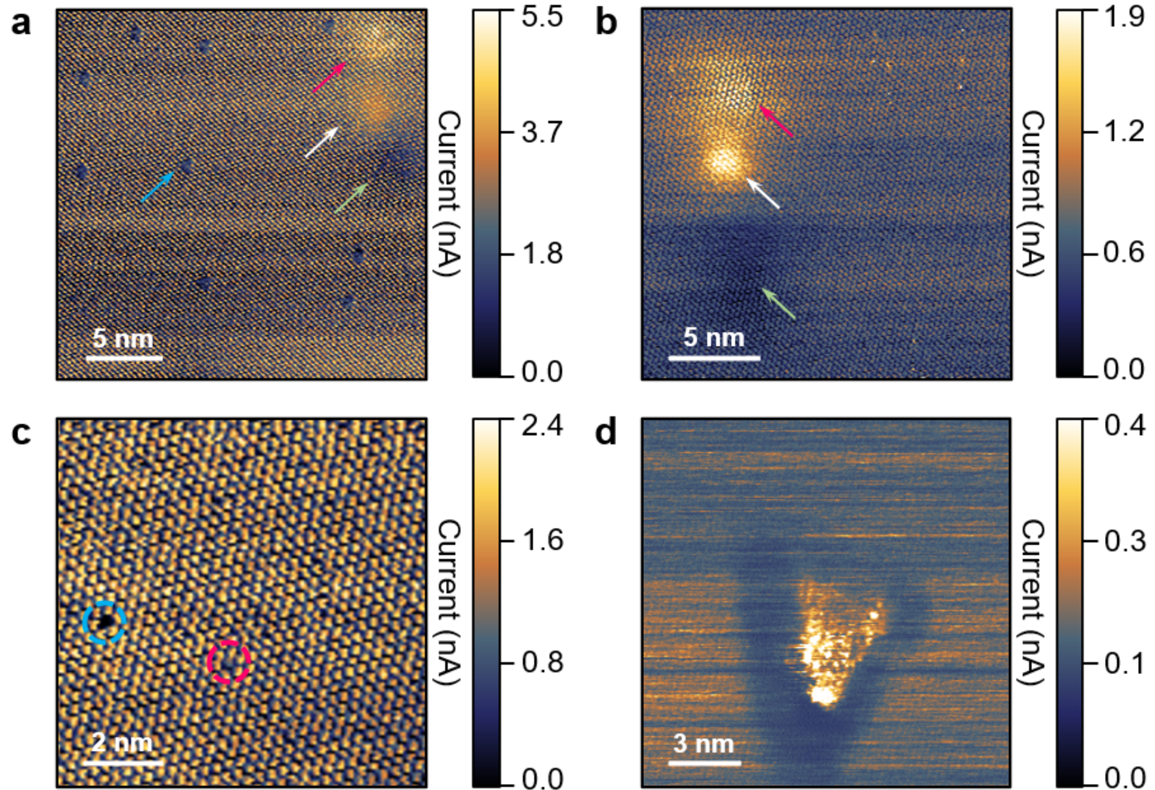

Figure 4.1: Imaging of different types of defects on MoS_2 (001) under ambient conditions via C-AFM. (a) Current image featuring dark, concentrated defects (blue arrow) as well as diffuse, large-area bright (pink and white arrows) and dark (green arrow) defects. (b) Enlarged current image on the diffuse defects in (a). (c) Current image exhibiting a faint, atomic-scale dark defect (pink circle) and a regular, atomic- scale dark defect (blue circle). (d) Current image showing an extended defect, with a central, bright region (enhanced conductivity) surrounded by a dark region (attenuated conductivity). All images were obtained with an applied normal load of 0.0 nN and at a scanning frequency of 15.62 Hz. Bias voltages: (a) 1.8 V; (b) 1.8 V; (c) 0.7 V; (d) 0.9 V.

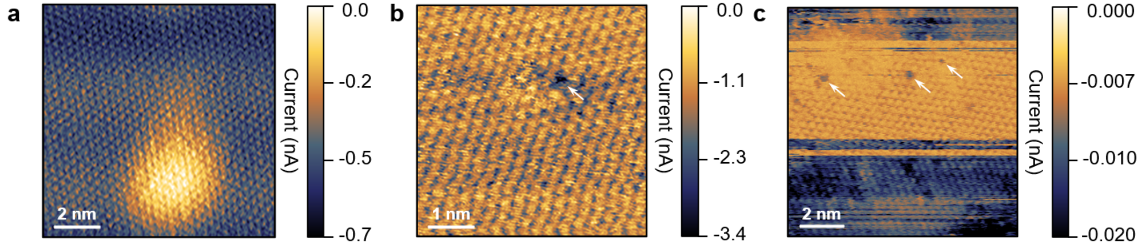

Figure 4.2: Imaging defects on different TMDs.(a) Current image recorded on WSe_2, a 2D TMD semiconductor, showing a diffuse bright defect overlaid on a continuous atomic lattice. (b) Current image recorded on WS_2, another 2D TMD semiconductor, showing a single top surface S vacancy (white arrow). (c) Current image recorded on $PtSe_2$, a 2D TMD semimetal, showing several atomic-scale defects (white arrows) and frequent contrast changes. All images were obtained with an applied normal load of 0.0 nN and at a scanning frequency of 15.62 Hz. Bias voltages: (a) -1.8 V; (b) -1.8 V; (c) -0.014 V.

summarized in Fig. 4.2. In particular, Fig.4.2(a) shows a current image recorded on WSe_2 (001), exhibiting a diffuse bright defect superimposed on a continuous atomic lattice similar to the diffuse defects imaged on MoS_2 (see Fig. 4.1(b)). Fig. 4.2(b) shows a current image recorded on WS_2 (001). Along with the atomically-resolved crystal structure, this image captures a single S vacancy on the top surface, in the form of a confined dark spot as indicated by the white arrow. Finally, Fig. 4.2(C) shows a current image recorded on $PtSe_2$ (001), where the atomic surface structure together with several atomic-scale defects (indicated by white arrows) can be resolved. Much like early NC-AFM images recorded on Si (111)-7 $\times$ 7 [12], this image features frequent changes in contrast that can be attributed to minute alterations in the tip apex that occur during scanning: *e.g.*, by transfer of atoms or molecules to/from the sample surface [13].

4.3 Charge State Manipulation

Going beyond imaging, we also investigated the capability of our method to electronically manipulate defects under ambient conditions. In particular, Fig. 4.3(a) shows a current image of MoS_2 with two extended defects that exhibit higher conductivity than their surroundings. Magnified images on the defects allow their study with high spatial resolution (Fig. 4.3(b)). By performing current vs voltage (I–V) sweeping for multiple cycles (Fig. 4.3(c)), we found an emerging peak in the I–V curves at a bias voltage of about -1.7 V, which is first attenuated and then re-emerges

during the I–V cycles. This is accompanied by a side peak appearing between -1.1 and -1.5 V. After the I–V sweeps, the high-conductivity region associated with the defect disappears, in favor of a low-conductivity region (see Fig. 4.3(d) and (e), to be compared with Fig. 4.3(a) and (b)). The possibility of surface contamination can be ruled out, as roughness fluctuations are not observed in the corresponding topography images (Fig. 4.3(f-i)). The negative differential resistance in Fig. 4.3(c), characterized by a decrease in current with increasing voltage, may be related to localized surface charging/discharging behavior. According to the passive sign convention, more electrons may flow out of the defect location, indicating a pre-existing negatively charged region. After I–V sweeping, more positive charge will accumulate in the region to compensate the nonuniform charge states, which may explain the slightly lower current detected on the defect location after the I–V sweeps (Fig. 4.3(e)). The modified charge state of the defective location showed stability by exhibiting the same structure for at least 8 minutes. As such, we refer to such manipulation of charge state as irreversible manipulation. These experiments demonstrate that our method may provide a feasible strategy for localized manipulation/elimination of electrical surface defects on 2D materials under ambient conditions.

As opposed to the irreversible manipulation of charge state associated with defects described above, some manipulation attempts showed a reversible effect as summarized in Fig. 4.4. In particular, the current image in Fig. 4.4(a) shows a defect structure on MoS_2 in the form of a paired halo. To manipulate the defect structure, I–V sweeping was performed (Fig. 4.4(b)) on the location indicated by the red dot in Fig. 4.4(a). The comparison of the first I–V curve with the following ones indicates the occurrence of charge compensation. This is based on the observation that the first I-V curve features flow of current in the bias regime ∼-0.5 to -1V, but no flow of current is observed in this bias regime for the second and third I-V curves. One possible explanation can be that the defective area had pre-existing charge. During the first I-V curve it accumulated opposite charge to become neutral, and that's why in that bias regime we do not observe flow of current for the second and third I-V curves again. This observation is also in agreement with the current image recorded after the I–V sweeps as shown in Fig. 4.4(c) where we can see that the charge state associated with the defect structure has almost disappeared and appears neutral. However, following a series of current images obtained by way of continued scanning (as shown in Fig. 4.4(d-h)), the original charge state associated with the defect structure reemerges. Due to presence of thermal drift, the area of scanning was adjusted in Fig. 4.4(g), then again in Fig. 4.4(h) so that the defect structure is within the imaging frame. Such reversible manipulation of defect structures suggests the involvement of temporal charge migration mechanisms, the fundamental understanding of which would nevertheless require further experiments and theoretical modeling.

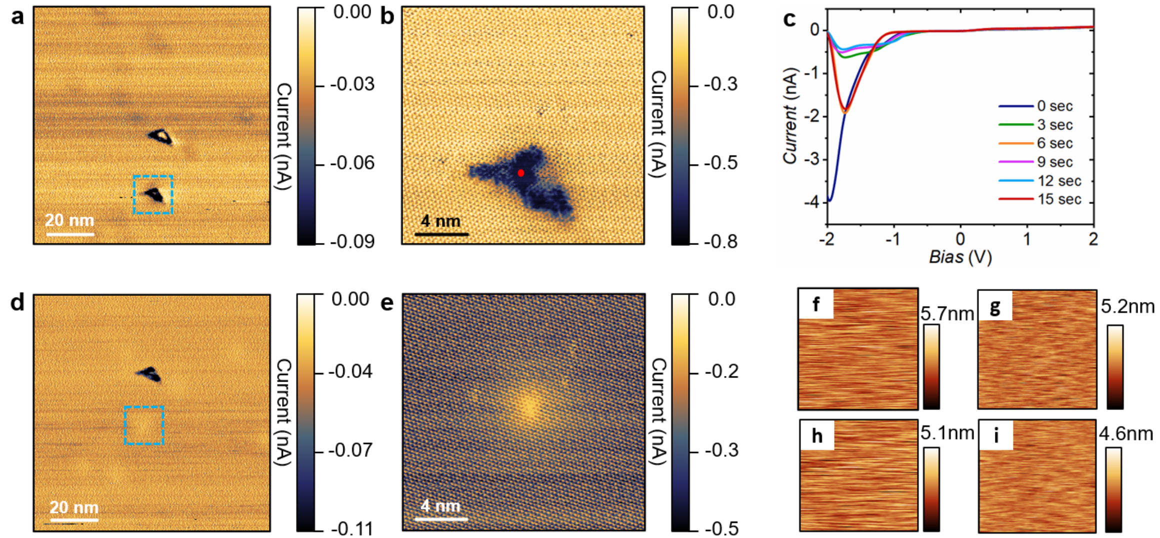

Figure 4.3: Electronic manipulation of a defect on MoS_2 via C-AFM under ambient conditions. (a) Large-scale current image showing two defects. (b) Enlarged current image on the defect highlighted by the blue dashed square in (a). The defect features enhanced conductivity compared to its surroundings. (c) I–V curves recorded on top of the defect location marked with the red dot in (b). (d) Current image of area (a) after the I–V sweeps. (e) Current image capturing the same defect in (b) after the I–V sweeps. The defect now features a slightly lower conductivity compared to its surroundings, with the uninterrupted atomic lattice overlaid on top of it. (f–i) Corresponding topographic images for (a), (b), (d), and (e), respectively. All images were obtained with an applied normal load of 0.0 nN and at a scanning speed 15.62 Hz. Bias voltages: (a) -1.0 V; (b) -1.3 V; (d) -0.8 V; (e) -0.8 V.

4.4 Imaging Disorder on HOPG

HOPG surfaces are highly crystalline, and generally have a low density of defects such as vacancies, impurities etc. However, cleaving HOPG surfaces with an adhesive tape to expose a fresh surface, generates different types of disorder on the surface such as step-edges, ribbons etc. These disorders or discontinuities can act as active sites (due to for example, dangling bonds) for dynamic surface processes such as adsorption of molecules [14, 15] . As such, a number of SPM studies focused on the electronic nature of these step edges and ribbons on HOPG [16, 17]. Motivated by that, we employed our high-speed C-AFM imaging methodology to observe different types of disorders or discontinuities on HOPG with high spatial resolution under ambient conditions. In this context, Fig. 4.5(a) shows a topographic image recorded

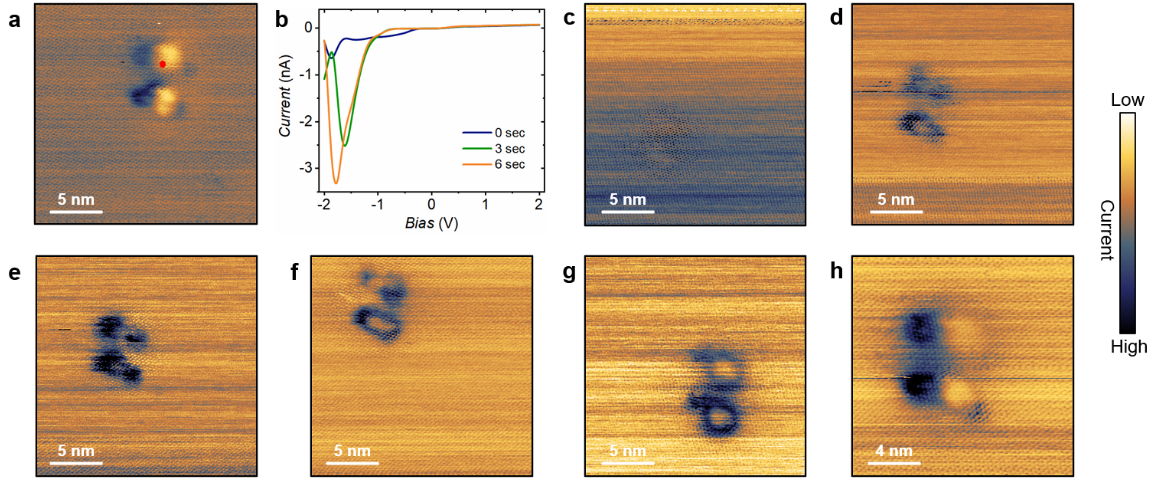

Figure 4.4: Reversible manipulation of a defect on MoS_2. (a) Current image recorded on MoS_2 showing a defective area in the form of two halos. (b) I–V curves recorded on top of the defect location marked with the red dot in (a). (c) Current image of area (a) after the I–V sweeps. (d-h) A series of current images showing the gradual re-emergence of the original defect structure. Due to noticeable thermal drift observed between (d) to (f), the area of scanning was adjusted in (g), and then again in (h) to have the defect structure within the imaging frame. All images were obtained with an applied normal load of 0.0 nN and at a scanning speed 15.62 Hz. Bias voltages: (a) -1.2 V; (c-f) -1.2 V; (g) -1.7 V; (h) -1.3 V.

on HOPG featuring very vaguely what appears to be another step-edge. A height profile drawn along the arrow A in Fig. 4.5(a) corresponds to a height difference in the range of 8-10 Å (Fig. 4.5(b)) which in turn refers to multiple HOPG atomic steps. The corresponding current image shown in Fig. 4.5(c) reveals the structure of the step-edge with atomic-resolution. It clearly shows multiple HOPG steps with distinctly resolved boundaries.

Going one step further, we observe another type of disorder on the HOPG surface as shown by the current image in Fig. 4.6(a). Along with the true atomically-resolved crystal structure (highlighted by the simultaneous imaging of the three atomic sites of HOPG crystal), this image also reveals another periodic feature, in particular a "superstructure" on the atomic lattice. The corresponding FT shown in Fig. 4.6(b) also confirms the presence of this periodic feature with a periodicity of $\sim$1.5 nm. Similar periodic features have previously been reported on cleaved HOPG surfaces imaged via STM [18–20]. Comparing our results with those reported in the literature, we assign this superstructure to a Moiré pattern. This Moiré superlattice can be

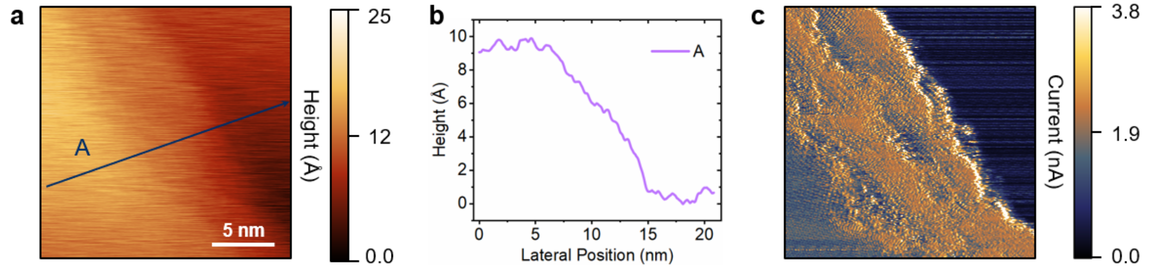

Figure 4.5: Imaging step-edge of HOPG. (a) Topographic image recorded on a cleaved HOPG surface showing vaguely the presence of a step-edge. (b) Height profile recorded along the arrow A in (a). The height profile shows a height difference of ∼8-10 Å. (c) The corresponding current image reveals more details of the step-edge with well-defined boundaries, showing potentially multiple graphite layers torn during the cleaving process. Scanning speed: 15.62 Hz. Bias voltages: (c) 0.01 V.

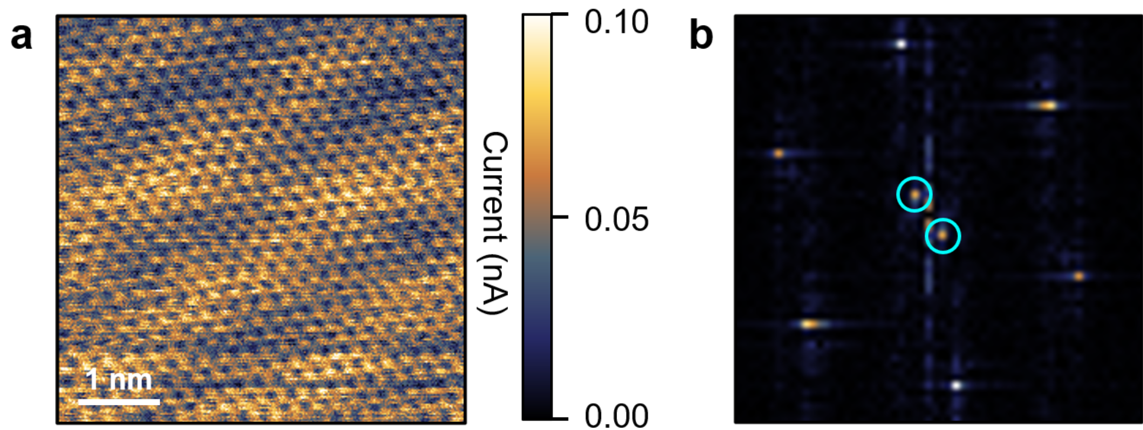

Figure 4.6: Superstructure imaged on HOPG. (a) Current image recorded on cleaved HOPG surface revealing the presence of a superstructure along with the atomically-resolved crystal structure. (b) The corresponding FT of the current image in (a). The bright spots highlighted by cyan circles represent the superstructure with a periodicity of ∼1.5 nm. Scanning speed: 15.62 Hz. Bias voltages: (a) 0.013 V.

created due to misorientation of the top layer of HOPG with respect to the underlying layer induced by the cleaving process [19, 20]. The periodicity of Moiré superlattice is given by the following equation.

$$D = \frac{a_0}{2sin\frac{\theta}{2}} \tag{4.1}$$

where a_0 is the crystal lattice constant, in this case of HOPG *i.e.* 0.246 nm, θ is misalignment angle, D is the Moiré periodicity. By plugging the experimentally determined Moiré periodicity of 1.5 nm in to Equation 4.1, we find a misalignment angle between the top and underlying HOPG layer of $\sim 9.4^{\circ}$.

4.5 Conclusions

The study of atomic-scale defects and disorder of material surfaces so far have been heavily dependent upon UHV operated SPM or electron microscopy techniques. The results presented in this chapter clearly demonstrate that the high speed C-AFM scanning possesses huge potential to be employed to study variety of surface defects, discontinuities and disorders directly under ambient conditions with atomic-level spatial resolution, that too in a cost-effective, straightforward way.

4.6 References

[1] S Manzeli, D Ovchinnikov, D Pasquier, O V Yazyev, and A Kis. 2d transition metal dichalcogenides. *Nature Reviews Materials*, 2(8):1–15, 2017.

[2] B Schuler, J-H Lee, C Kastl, K A Cochrane, C T Chen, S Refaely-Abramson, S Yuan, E van Veen, R Roldán, N J Borys, et al. How substitutional point defects in two-dimensional WS_2 induce charge localization, spin–orbit splitting, and strain. *ACS Nano*, 13(9):10520–10534, 2019.

[3] J Achard, F Silva, A Tallaire, X Bonnin, G Lombardi, K Hassouni, and A Gicquel. High quality MPACVD diamond single crystal growth: high microwave power density regime. *Journal of Physics D: Applied Physics*, 40(20):6175, 2007.

[4] X Zhang, F Zhang, Y Wang, D S Schulman, T Zhang, A Bansal, N Alem, S Das, V H Crespi, M Terrones, et al. Defect-controlled nucleation and orientation of WSe_2 on hBN: a route to single-crystal epitaxial monolayers. *ACS Nano*, 13(3):3341–3352, 2019.

[5] R Addou and R M Wallace. Surface analysis of WSe_2 crystals: spatial and electronic variability. *ACS Applied Materials & Interfaces*, 8(39):26400–26406, 2016.

[6] P Bampoulis, K Sotthewes, M H Siekman, and H J W Zandvliet. Local conduction in $Mo_xW_{1-x}Se_2$: The role of stacking faults, defects, and alloying. *ACS Applied Materials & Interfaces*, 10(15):13218–13225, 2018.

[7] K Nowakowski, H J W Zandvliet, and P Bampoulis. Barrier inhomogeneities in atomic contacts on WS_2. *Nano Letters*, 19(2):1190–1196, 2018.

[8] C Rodenbücher, G Bihlmayer, W Speier, J Kubacki, M Wojtyniak, M Rogala, Dominik Wrana, Franciszek Krok, and K Szot. Local surface conductivity of transition metal oxides mapped with true atomic resolution. *Nanoscale*, 10(24):11498–11505, 2018.

[9] P Bampoulis, R van Bremen, Q Yao, B Poelsema, H J W Zandvliet, and K Sotthewes. Defect dominated charge transport and fermi level pinning in MoS_2/metal contacts. *ACS Applied Materials & Interfaces*, 9(22):19278–19286, 2017.

[10] M Yankowitz, D McKenzie, and B J LeRoy. Local spectroscopic characterization of spin and layer polarization in WSe_2. *Physical Review Letters*, 115(13):136803, 2015.

[11] R Addou, L Colombo, and R M Wallace. Surface defects on natural MoS_2. *ACS Applied Materials & Interfaces*, 7(22):11921–11929, 2015.

[12] F J Giessibl. Atomic resolution of the Silicon (111)-(7 $\times$ 7) surface by atomic force microscopy. *Science*, 267(5194):68–71, 1995.

[13] M Z Baykara. Noncontact atomic force microscopy for atomic-scale characterization of material surfaces. In *Surface Science Tools for Nanomaterials Characterization*, pages 273–316. Springer, 2015.

[14] M P Zach, J T Newberg, L Sierra, J C Hemminger, and R M Penner. Chemical vapor deposition of silica micro-and nanoribbons using step-edge localized water. *The Journal of Physical Chemistry B*, 107(23):5393–5397, 2003.

[15] S Yang, E S Kooij, B Poelsema, D Lohse, and H J W Zandvliet. Correlation between geometry and nanobubble distribution on HOPG surface. *Europhysics Letters*, 81(6):64006, 2008.

[16] S Banerjee, M Sardar, N Gayathri, A K Tyagi, and B Raj. Conductivity landscape of highly oriented pyrolytic graphite surfaces containing ribbons and edges. *Physical Review B*, 72(7):075418, 2005.

[17] Y Niimi, T Matsui, H Kambara, K Tagami, M Tsukada, and Hiroshi Fukuyama. Scanning tunneling microscopy and spectroscopy of the electronic local density of states of graphite surfaces near monoatomic step edges. *Physical Review B*, 73(8):085421, 2006.

[18] M Flores, E Cisternas, J D Correa, and P Vargas. Moiré patterns on STM images of graphite induced by rotations of surface and subsurface layers. *Chemical Physics*, 423:49–54, 2013.

[19] J Xhie, K Sattler, M Ge, and N Venkateswaran. Giant and supergiant lattices on graphite. *Physical Review B*, 47(23):15835, 1993.

[20] J M Campanera, G Savini, Irene Suarez-Martinez, and M I Heggie. Density functional calculations on the intricacies of Moiré patterns on graphite. *Physical Review B*, 75(23):235449, 2007.

Chapter 5

Atomically-Resolved Study of Thin Crystals of a Transition Metal Carbide (MXene): α–Mo_2C

5.1 Introduction

Thin transition metal carbides (TMCs), a member of the growing family of MXenes, garnered significant attention in recent years due to their attractive combination of mechanical and electrical properties with chemical and thermal stability. On the other hand, a complete picture of how defects affect the physical properties and application potential of this emerging class of materials, is lacking. In this chapter, we present an atomic-resolution study of defects on thin crystals of molybdenum carbide (α–Mo_2C) grown via chemical vapor deposition (CVD), by way of C-AFM measurements under ambient conditions. Defects are characterized based on the type (enhancement / attenuation) and spatial extent (compact / extended) of the effect they have on the conductivity landscape of the crystal surfaces. Additionally, we report on our observation of an exotic electronic effect: room-temperature charge ordering on the surface conductivity landscape of α–Mo_2C, with signatures of rotational symmetry breaking with respect to the underlying atomic lattice.

5.2 Thin Crystals of CVD-Grown α–Mo_2C

While traditionally used in bulk form as cutting tools and refractory structural materials thanks to their exceptional hardness and thermal resistance [1], transition metal carbides and nitrides in nanoscale form (from a single layer up to a few tens of nanometer, collectively referred to as MXenes) have been the focus of accelerating research over the past decade [2]. This intense interest arises from a favorable

combination of physical properties and chemical as well as thermal resistance, which results in exceptional potential for applications ranging from energy storage [3] and electromagnetic shielding [4], all the way to catalysis [5] and next-generation electronics [6]. While the great majority of the scientific effort so far has been directed at the first-discovered MXene, Ti_3C_2 [7], the family of materials includes tens of different members, which presents opportunities for various applications. In particular, the alpha phase of molybdenum carbide (α–Mo_2C) in thin form exhibits exciting electronic properties including thickness-dependent critical temperatures for superconductivity [8], as well as negative magnetoresistance [9]. Remarkably, using CVD approaches, it is possible to grow thin crystals of α–Mo_2C (with lateral sizes on the order of 10 μm, and down to thicknesses of a few up to a few tens of nm) with clean surfaces that are devoid of issues related to the presence of functional groups and fluorination that are common with wet-chemistry-etched MXenes [8, 10]. This presents an opportunity to experimentally investigate the intrinsic structure and properties of the bare α–Mo_2C surface.

An important question involving MXenes in general, and α–Mo_2C in particular, revolves around surface defects. In particular, the formation of an atomic-scale understanding of the types and densities of defects present at or near thin α–Mo_2C crystal surfaces, as well as their effect on the electronic surface landscape, is crucial for engineering materials toward tailored applications. Despite this point, the literature includes only a limited number of experimental [11–13] and computational [14] studies of defects on α–Mo_2C. As the focus of the experimental work has mostly been superconductivity, experiments (based on STM) have been typically performed under pristine conditions of ultrahigh vacuum and low temperature. On the other hand, no atomic-resolution imaging has been performed under ambient conditions, for which the majority of potential applications would be designed. The high-speed C-AFM under ambient conditions approach discussed in earlier chapters is suited well to achieve this goal.

Motivated as above, we present here an experimental study aimed at investigating defects on the (100) surface of thin α–Mo_2C crystals. Towards this purpose, the thin crystals of α–Mo_2C were synthesized via CVD on copper foils by the group of Prof. Goknur Cambaz Buke at the TOBB University of Economics and Technology, supported by the Air Force Office of Scientific Research under Award Numbers FA9550-19-1-7048 and FA9550-22-1-0358. Atomic-resolution C-AFM measurements (following the same methodology described in Section 2.3) reveal different types of "compact" defects that either attenuate or enhance the local conductivity, up to lateral spans of a few nm. Extended defects, hypothesized to be dislocations, are also imaged with detail. Furthermore, we also observe a periodic modulation of charge in the surface conductivity landscape that does not follow the rotational symmetry of the underlying the lattice. Details associated with these observations are provided in the rest of the Chapter.

5.3 Atomically-Resolved Structure of α–Mo_2C

A representative topographic image of an α–Mo_2C crystal, recorded via tapping-mode AFM is shown in Fig. 5.1(a). The crystal in this image laterally extends ~10-15 μm, with a thickness of ~20 nm. Fig. 5.1(b) shows the phase image that is simultaneously recorded with the topography map in Fig. 5.1(a) during imaging. As opposed to the topographic image, the phase image reveals two different contrasts on top of the α–Mo_2C crystal labeled as I and II, indicative of materials with different mechanical properties [15]. Previous studies in the literature report that during the CVD-based synthesis of α–Mo_2C, graphene layers can grow on the crystal surfaces [16, 17]. Consequently, our initial hypothesis is that the α–Mo_2C crystal shown in Fig. 5.1 is partially covered by graphene. To further investigate this idea, Fig. 5.1(c) presents the topography of a smaller area on the crystal surface (highlighted by white rectangle in Fig. 5.1(b)) which includes both Regions I and II. Studying Fig. 5.1(c), one can observe that (i) II appears to be draped over I and (ii) I features well-resolved terraces separated by steps. The height difference between I and II, as measured via profile A in Fig. 5.1(d), is ~8 Å which can be assigned to monolayer graphene [18]. On the other hand, the height difference across a step within I as indicated by profile B in Fig. 5.1(d) is ~5 Å which is reasonably close to the lattice constant of 4.75 Å, corresponding to the height of one unit cell of α–Mo_2C crystal along the [100] direction, indicative of terraces separated by single steps. It should be noted that Fig. 5.1(c) also reveals a regular topographic undulation on material II, with ripples of height ~5 Å separated by ~45 nm. While one could tentatively assign the formation of these ripples to thermal-relaxation-induced strain during cool-down of crystals [19], we do not further investigate this observation here as the focus of the current work is on the bare α–Mo_2C surface.

Following the large-scale analysis of the α–Mo_2C crystals above, we turn our attention to the atomic-resolution imaging of the bare crystal surfaces, in the form of small-scale (about 10 nm $\times$ 10 nm) current maps recorded via C-AFM under ambient conditions. A representative, atomically-resolved image of the crystal surface is provided in Fig. 5.2(a), with an average periodicity of ~2.2 Å as determined by the corresponding FT (Fig. 5.2(b)). The image is characterized by the presence of hexagonal features of high current, with well-defined current minima at their centers. A superposed current contrast on the hexagonal lattice with larger periodicity than the atomic-scale hexagons is also detectable, which we will study further in one of the later sections. α–Mo_2C has an orthorhombic crystal structure where the Mo atoms are positioned in a slightly distorted hexagonal close-packed arrangement and the C atoms occupy octahedral voids of the Mo lattice on the (100) surface (see Fig. 5.2(c) for an atomic model) [8]. The 2.2 Å periodicity observed in Fig. 5.2(a) matches well with the interatomic distance of the Mo-terminated surface (whereby every other Mo atom is on the surface plane and the rest are below), which also corresponds

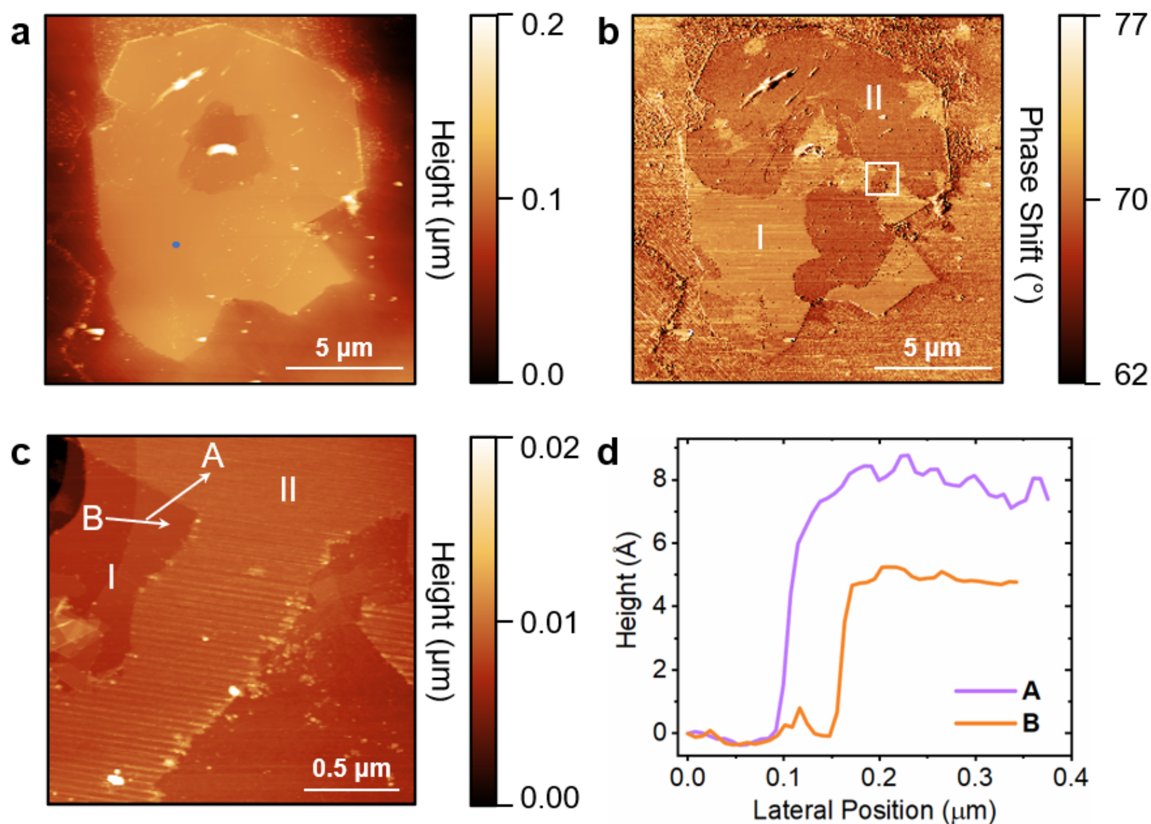

Figure 5.1: Large-scale AFM imaging of an α–Mo_2C crystal. (a) A large-scale topographical image acquired on a α–Mo_2C crystal on copper foil. (b) Phase image acquired simultaneously with the topographical image in (a). Two regions with distinct phase contrast are visible on the surface, indicative of different materials (I and II). (c) A zoomed-in topographical image on the region highlighted in (b), showing material II is "draped" over material I. (d) Height profiles recorded along the arrows A and B in (c). The profile along A shows a height difference of ∼8 Å between materials I and II, consistent with a monolayer of graphene. The profile along B shows two terraces separated by a step of height ∼5 Å on I, consistent with a single unit cell of α–Mo_2C.

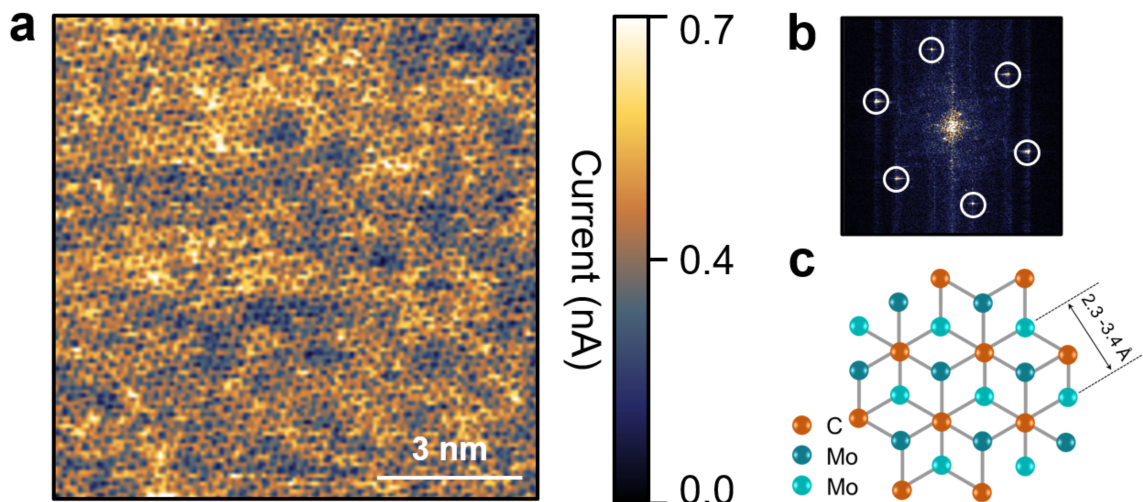

Figure 5.2: Atomic-resolution imaging of the α–Mo_2C (100) surface under ambient conditions via C-AFM. (a) Current map recorded on top of the α–Mo_2C crystal via C-AFM under ambient conditions by focusing on a small area similar to the one represented by the blue circle in 5.1(a). (b) FT corresponding to the current map shown in (a). The bright spots highlighted by white circles represent the lattice structure of α–Mo_2C (100) with a periodicity of ~2.2 Å. (d) Atomic model of the α–Mo_2C (100) surface. All images were obtained with an applied normal load of 0.0 nN, and at a scanning frequency of 15.62 Hz. Bias voltages: (a) 0.01 V.

to the lateral distance between C atoms. The recorded periodicity is also close to the value reported in the literature obtained via a transmission electron microscopy (TEM) study [20]. It should however be noted that different studies in the literature have reported different lattice periodicities for the Mo-terminated surface of α–Mo_2C, ranging for 2.3 to 3.4 Å [11, 17, 20]. This variation can be caused by the presence of different amounts of strain in the crystal, incorporated during synthesis of the material [11, 21]. On the other hand, in our C-AFM work, we routinely observe a lattice periodicity of 2.2 Å. While it is not possible from this analysis to definitively assign features in our C-AFM images to specific lattice sites, a plausible hypothesis could be that Mo atoms on the surface lead to the recording of current maxima in the form of hexagons.

5.4 Imaging A Variety of Defects on α–Mo_2C

Following the analysis of lattice structure above, we explored different types of defects on the α–Mo_2C surface and their effect on the conductivity landscape. Our atomic-resolution measurements routinely revealed the presence of various defects on the crystal surfaces, as exemplified by the large-scale (100 nm $\times$ 100 nm) current image provided in Fig. 5.3(a). Defects observed in this image can be distinguished based on the "sign" of their effect on local conductivity (in terms of whether they lead to an increase or decrease in current recorded by the C-AFM probe) as well as their lateral extent. With respect to the first point, we observe two types of defects on the crystal surface: bright and dark (leading to an increase or decrease in local conductivity, respectively). Another observation is that while some of these defects are "compact" in nature as highlighted by maroon and green circles (for bright and dark defects, respectively), some defects are "elongated/extended" in one direction as highlighted by the cyan ovals. The zoomed-in current image in Fig. 5.3(b) allows us to evaluate compact defects based on the effect of their lateral extent on surface conductivity. In particular, it is seen that the electronic modulation induced by the compact defects extend over a few nm, up to 5 nm. It should be noted that large-scale current images such as the one presented in 5.3(a) allow to calculate a defect density on the order of 10^{11} cm^{-2} for the α–Mo_2C surface, which is comparable to what has been reported for TMDs in the literature [22]. Of particular importance is the complete absence of these defects in the topographical images that are simultaneously recorded with the current data (see the corresponding topographical maps in Fig. 5.3(b) and (d)). Based on the fact that C-AFM records topography and current channels independently (as opposed to STM, which provides images that are a convolution of topographical and electronic effects [23]), our observation highlights the electronic nature of the observed defects and eliminates the possibility that the origins of the defects are contaminants / adsorbates on the crystal surfaces.

Following the overview investigation of defects on the α–Mo_2C (100) surface provided in Fig. 5.3, we explored the effects of different types of defects on the conductivity landscape with atomic resolution. Specifically, Fig. 5.4 provides a closer look at the compact defects. Along with the atomically-resolved crystal structure of α–Mo_2C (100) (similar to the image provided in Fig. 5.2(a)), Fig. 5.4(a) shows several compact defects with bright contrast, indicating increased local conductivity. Fig. 5.4(b) shows another, smaller current map that captures two compact bright defects. The continuity of the underlying atomic lattice appears to be broken on and near the bright defects indicated by the disturbed symmetry of the lattice in the current map. A similar observation was made before for certain point defects on WS_2, which led to patterns observed in the current channel that are significantly different from the structure of the regular continued lattice [22]. Fig. 5.4(c) shows a defect on the crystal that manifests as dark contrast, *i.e.* a reduction in local conductivity. In contrast to

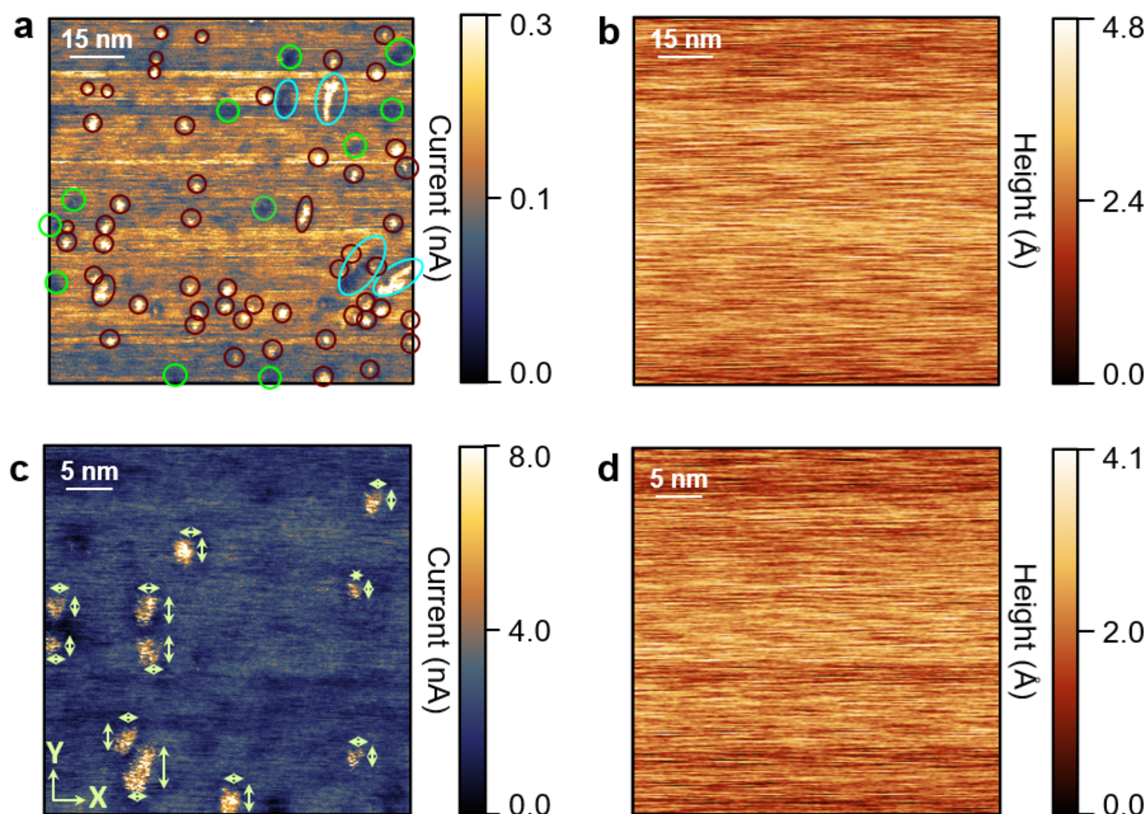

Figure 5.3: Imaging defects on α–Mo$_2$C under ambient conditions via C-AFM. (a) Current image showing different types of defects on α–Mo$_2$C, featuring relatively "compact" bright (maroon circles) and dark (green circles) defects, as well as elongated (cyan ovals) bright and dark defects. (b) The corresponding topographic image for the current map in (a) that shows no sign of the defects. (c) Zoomed-in current image on the compact defects reveal that they laterally extend ∼2-5 nm. (d) The corresponding topographic image for the current image shown in (c). All images were obtained with an applied normal load of 0.0 nN, and at a scanning frequency of 15.62 Hz. Bias voltages: (a) 0.5 V, (c) 0.7 V.

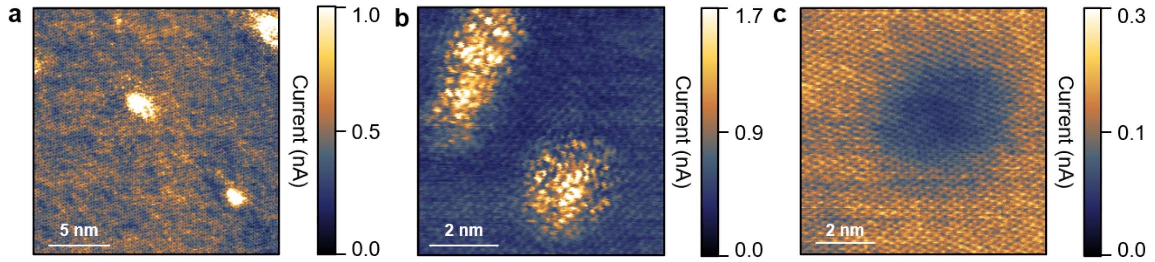

Figure 5.4: Atomic-resolution imaging of compact defects on α–Mo_2C under ambient conditions via C-AFM. (a) Current image showing the atomically-resolved surface structure along with multiple, compact bright defects. (b) A smaller current image featuring two compact bright defects. Note that the symmetry of the lattice appears to be disturbed near the defects. (c) Current image showing a compact, dark defect. Unlike the bright defects in (a) and (b), the lattice structure is uninterrupted over the dark, defective area. All images were obtained with an applied normal load of 0.0 nN, and at a scanning frequency of 15.62 Hz. Bias voltages: (a) 0.01 V, (b) 0.5 V, (c) 0.2 V.

the disrupted lattice structure in the current map observed for bright defects, one can observe here that the dark contrast associated with the defect is superimposed on the uninterrupted lattice of α–Mo_2C, suggesting that the origin of the defect most probably lies in the subsurface region. It is important to note here that the observation of bright defects having a more pronounced effect on the conductivity landscape (both in terms of modulation of current magnitude and also in terms of lattice continuity) when compared with dark defects (which seem to have a more diffuse effect whereby the atomic lattice of the surface appears as uninterrupted) highlighted by Fig. 4.4 is a common characteristic of all measurements we performed on α–Mo_2C.

Moving over from the study of compact defects, Fig. 5.5 provides a closer look at two elongated defects with bright contrast. As opposed to the compact defects, the elongated defects longitudinally extend $\sim$10-15 nm with a single preferred direction for the defect in Fig. 5.5(a) and two preferred directions for the one in Fig. 5.5(b). A closer look reveals certain characteristics: (i) the preferred directions for elongated defects are aligned with the crystallographic directions of the underlying lattice (indicated by blue and yellow dotted lines in Fig. 5.5, respectively) , (ii) the "width" of the defects (perpendicular to the longitudinal axes) span several unit cells, and (iii) "loops" are formed at the ends of the defects (resolved most clearly for the defect in Fig. 5.5(a)). Based on these observations, we propose mixed dislocations (of combined edge and screw character) and/or misfit dislocations [24] as the most likely identity for the observed defects, whereby the longitudinal features correspond to

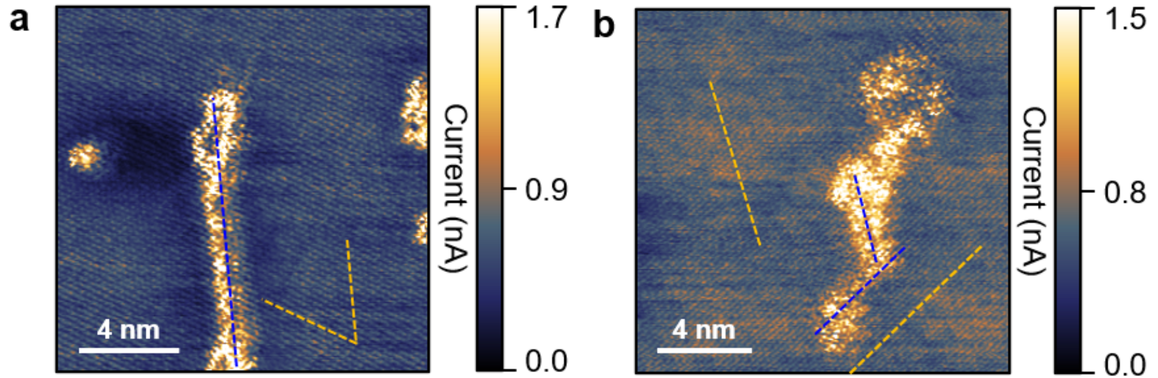

Figure 5.5: Atomic-resolution imaging of elongated defects on α–Mo_2C under ambient conditions via C-AFM. (a) Current map recorded on α–Mo_2C showing an elongated bright defect that extends up to $\sim$11 nm. (b) Current map recorded on α–Mo_2C showing another elongated bright defect that extends up to $\sim$12 nm. Yellow dotted lines indicate the crystallographic directions of symmetry of the underlying lattice, whereas the blue dotted lines indicate the longitudinal directions of the defects. All images were obtained with an applied normal load of 0.0 nN, and at a scanning speed 15.62 Hz. Bias voltages: (a) 0.2 V, (b) 0.5 V.

screw dislocations and the looped regions are characterized by edge dislocations that thread out of the surface. Interestingly, while the majority of the elongated defects seem to lead to enhanced local conductivity, the looped ends instead feature local attenuation of conductivity (in accordance with STM work performed previously on metal surfaces [24]), supporting the idea that the longitudinal parts and the looped ends of the defect are of different character. Besides the compact and elongated defects, we also observe another type of defect that is very confined, essentially confined to a single atomic site as shown in Fig. 5.6. In this current image, we observe a highly confined dark spot surrounded by enhanced charge density. Comparing this image with similar types of defects reported in the literature on other material systems via STM, we hypothesize that this defect can be a single Mo vacancy [25, 26]. Considering that the presence of structural defects (including dislocations) is expected to influence, *e.g.*, the thickness-dependent superconductive properties of α–Mo_2C crystals [27], local transport measurements such as those presented here have the potential to lead the way to defect engineering studies targeted at tailored electronic properties.

We note here that the defects observed here are significantly different in size and shape from those previously reported on α–Mo_2C samples grown via CVD [11, 12, 8]. In particular, Zhang *et al.* observed, by way of STM measurements, rhomboid- and triangular-shaped dark defects that were attributed to Mo vacancies, as well as

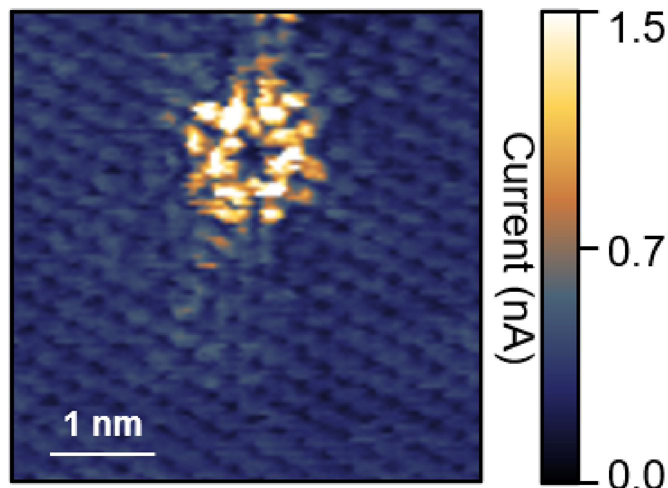

Figure 5.6: Current image recorded on α–Mo_2C, showing a concentrated dark defect surrounded by enhanced charge density. Scanning speed 15.62 Hz. Bias voltage: 0.05 V.

compact bright defects that were attributed to Mo adatoms, by way of topographic arguments (which are problematic for the interpretation of STM images which are convolutions of topographical and electronic information) [11]. In contrast to our observations, the defects reported in this particular work laterally extend ∼1 nm or smaller. Another study performed by Geng *et al.* reported bright defects that extend ∼5 nm and were attributed to Mo clusters on the crystal surfaces [21]. A promising avenue to understand the origin of the defects observed in our experiments is to perform *ab initio* calculations based on density functional theory, by way of collaborations with experienced research groups.

5.5 Room Temperature Charge Ordering on α–Mo_2C

Atomic-resolution C-AFM imaging under ambient conditions also revealed a periodic modulation (*i.e.*, ordering) of charge, superimposed on the atomic lattice structure of α–Mo_2C (Fig. 5.7(a)), in an area that includes two prominent defects. The corresponding FT shown in Fig. 5.7(b) corroborates this observation, whereby the bright spots highlighted by red circles (with a periodicity of ∼2.2 Å) represent the atomic structure of the α–Mo_2C surface, and the bright spots highlighted by green circles represent the periodic charge modulation with a periodicity of ∼11.4 Å. Even

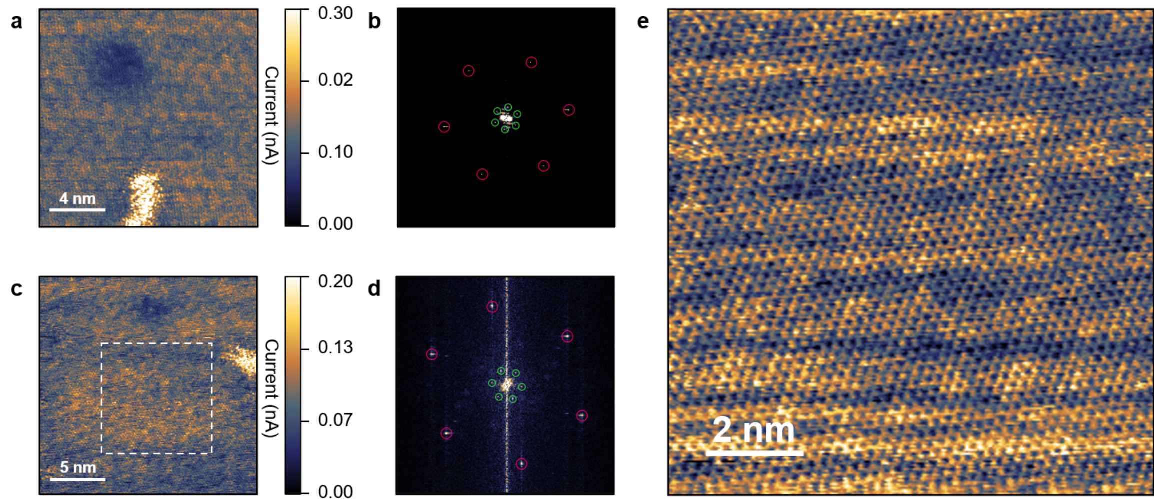

Figure 5.7: Observation of room-temperature charge ordering on α–Mo_2C via C-AFM. (a) Current image recorded on α–Mo_2C, showing periodic modulation of charge, along with two defects. (b) The corresponding FT of the image shown in (a). The bright spots highlighted by red circles represent the lattice structure of α–Mo_2C with a periodicity of ∼2.2 Å, while the bright spots highlighted by green circles represent the charge modulation with a periodicity of ∼11.4 Å. (c) Another current image recorded on α–Mo_2C exhibiting charge ordering. (d) The corresponding FT of the image shown in (c). The bright spots highlighted by red and green circles represent lattice structure of α–Mo_2C (periodicity ∼2.2 Å) and periodic modulation of charge (periodicity ∼11.1 Å), respectively. (e) Enlarged current image of the area highlighted by the white dotted square in (c), showing an ordering of charge superimposed on the atomic surface lattice. All images were obtained with an applied normal load of 0.0 nN and at a scanning frequency of 15.62 Hz. Bias voltages: (a) 0.1 V; (c) 1.3 V; (e) 1.3 V.

more interestingly, the FT clearly shows the broken rotational symmetry between these two periodicities with an angular difference of $\sim$13°. These results are supported by additional measurements on the material surface that show charge ordering (Fig. 5.7(c), (e)), with the corresponding FT again showing two periodicities corresponding to the lattice structure ($\sim$2.2 Å) and charge modulation ($\sim$11.1 Å), respectively, with an angular difference of $\sim 12°$ between the two (Fig. 5.7(d)). At this point, the question arises whether the superimposed modulations observed in the current maps can be caused by Moiré patterns that involve out-of-plane undulations of the material surface due to strain [11]. Unlike STM, the C-AFM method delivers two separate channels of data for the recording of topography and current, and the absence of any structural features in topography maps acquired simultaneously with the current data here allows us to unambiguously assign the observed modulations in the current images to electronic, not structural, origins. The discovery of room-temperature charge ordering in α–Mo_2C is important not only from a fundamental point of view, as such phenomena have been very rarely reported for other members of the 2D materials family [28], but also from a technological perspective, as it may lead to the possibility of exciting electronic device applications (e.g., for current switching) for MXenes.

5.6 Conclusions

In this chapter, we have presented atomic-resolution C-AFM experiments on the (100) surface of thin α–Mo_2C crystals grown via CVD, performed under ambient conditions. Imaging revealed the atomic-scale lattice structure characterized by hexagonal features, and the presence of various defects that locally affect surface conductivity. Charge ordering in the form of an electronic superstructure has also been observed, remarkably at room temperature. In general, it is projected that the local information provided by C-AFM on how the presence of defects affects local conductivity can be combined with larger-scale transport measurements, with the eventual goal of informing growth efforts for defect engineering toward tailored applications.

5.7 References

[1] S T Oyama. Introduction to the chemistry of transition metal carbides and nitrides. In *The chemistry of transition metal carbides and nitrides*, pages 1–27. Springer, 1996.

[2] A VahidMohammadi, J Rosen, and Y Gogotsi. The world of two-dimensional carbides and nitrides (MXenes). *Science*, 372(6547):eabf1581, 2021.

[3] B Anasori, M R Lukatskaya, and Y Gogotsi. 2D metal carbides and nitrides (MXenes) for energy storage. *Nature Reviews Materials*, 2(2):1–17, 2017.

[4] T Yun, H Kim, A Iqbal, Y S Cho, G S Lee, M-K Kim, S J Kim, D Kim, Y Gogotsi, S O Kim, et al. Electromagnetic shielding of monolayer MXenes assemblies. *Advanced Materials*, 32(9):1906769, 2020.

[5] A Morales-Garcia, F Calle-Vallejo, and F Illas. MXenes: new horizons in catalysis. *ACS Catalysis*, 10(22):13487–13503, 2020.

[6] H Kim, Z Wang, and H N Alshareef. MXetronics: Electronic and photonic applications of MXenes. *Nano Energy*, 60:179–197, 2019.

[7] M Naguib, M Kurtoglu, V Presser, J Lu, J Niu, M Heon, L Hultman, Y Gogotsi, and M W Barsoum. Two-dimensional nanocrystals produced by exfoliation of Ti_3AlC_2. *Advanced Materials*, 23(37):4248–4253, 2011.

[8] C Xu, L Wang, Z Liu, L Chen, J Guo, N Kang, X-L Ma, H-M Cheng, and W Ren. Large-area high-quality 2D ultrathin Mo_2C superconducting crystals. *Nature Materials*, 14(11):1135–1141, 2015.

[9] L Wang, C Xu, Z Liu, L Chen, X Ma, H-M Cheng, W Ren, and N Kang. Magnetotransport properties in high-quality ultrathin two-dimensional superconducting Mo_2C crystals. *ACS Nano*, 10(4):4504–4510, 2016.

[10] D Geng, X Zhao, L Li, P Song, B Tian, W Liu, J Chen, D Shi, M Lin, W Zhou, et al. Controlled growth of ultrathin Mo_2C superconducting crystals on liquid Cu surface. *2D Materials*, 4(1):011012, 2016.

[11] Z Zhang, H Gedeon, Z Cheng, C Xu, Z Shao, H Sun, S Li, Y Cao, X Zhang, Q Bian, et al. Layer-stacking, defects, and robust superconductivity on the Mo-terminated surface of ultrathin Mo_2C flakes grown by CVD. *Nano Letters*, 19(5):3327–3335, 2019.

[12] S Li, Z Zhang, C Xu, Z Liu, X Chen, Q Bian, H Gedeon, Z Shao, L Liu, Z Liu, et al. Magnetic doping induced superconductivity-to-incommensurate density waves transition in a 2D ultrathin Cr-doped Mo_2C crystal. *ACS Nano*, 15(9):14938–14946, 2021.

[13] C Xu, Z Liu, Z Zhang, Z Liu, J Li, M Pan, N Kang, H-M Cheng, and W Ren. Superhigh uniform magnetic Cr substitution in a 2D Mo_2C superconductor for a macroscopic-scale kondo effect. *Advanced Materials*, 32(38):2002825, 2020.

[14] J D Gouveia and J R B Gomes. Structural and energetic properties of vacancy defects in MXene surfaces. *Physical Review Materials*, 6(2):024004, 2022.

[15] R García. *Amplitude modulation atomic force microscopy.* John Wiley & Sons, 2011.

[16] F Turker, O R Caylan, N Mehmood, T S Kasirga, C Sevik, and G Cambaz Buke. CVD synthesis and characterization of thin Mo_2C crystals. *Journal of the American Ceramic Society*, 103(10):5586–5593, 2020.

[17] J-B Qiao, Y Gong, W-J Zuo, Y-C Wei, D-L Ma, H Yang, N Yang, K-Y Qiao, J-A Shi, L Gu, et al. One-step synthesis of van der waals heterostructures of graphene and two-dimensional superconducting α-Mo_2C. *Physical Review B*, 95(20):201403, 2017.

[18] K S Novoselov, A K Geim, S V Morozov, D Jiang, Y Zhang, S V Dubonos, I V Grigorieva, and A A Firsov. Electric field effect in atomically thin carbon films. *Science*, 306(5696):666–669, 2004.

[19] B Borca, F Calleja, J J Hinarejos, A L V de Parga, and R Miranda. Reactivity of periodically rippled graphene grown on Ru(0001). *Journal of Physics: Condensed Matter*, 21(13):134002, 2009.

[20] F Zhang, W Zheng, Y Lu, L Pabbi, K Fujisawa, A L Elías, A R Binion, T Granzier-Nakajima, T Zhang, Y Lei, et al. Superconductivity enhancement in phase-engineered molybdenum carbide/disulfide vertical heterostructures. *Proceedings of the National Academy of Sciences*, 117(33):19685–19693, 2020.

[21] D Geng, X Zhao, Z Chen, W Sun, W Fu, J Chen, W Liu, W Zhou, and K P Loh. Direct synthesis of large-area 2D Mo_2C on in situ grown graphene. *Advanced Materials*, 29(35):1700072, 2017.

[22] K Nowakowski, H J W Zandvliet, and P Bampoulis. Barrier inhomogeneities in atomic contacts on WS_2. *Nano Letters*, 19(2):1190–1196, 2018.

[23] C J Chen. *Introduction to Scanning Tunneling Microscopy Third Edition*, volume 69. Oxford University Press, USA, 2021.

[24] J de La Figuera, K Pohl, O R de La Fuente, A K Schmid, N C Bartelt, C B Carter, and R Q Hwang. Direct observation of misfit dislocation glide on surfaces. *Physical Review Letters*, 86(17):3819, 2001.

[25] R Addou, L Colombo, and R M Wallace. Surface defects on natural MoS_2. *ACS Applied Materials & Interfaces*, 7(22):11921–11929, 2015.

[26] R Addou and R M Wallace. Surface analysis of WSe_2 crystals: spatial and electronic variability. *ACS Applied Materials & Interfaces*, 8(39):26400–26406, 2016.

[27] Z Liu, C Xu, C Wang, S Song, L Wang, Y Wang, N Kang, X Ma, H-M Cheng, and W Ren. Grain boundaries and tilt-angle-dependent transport properties of a 2D Mo_2C superconductor. *Nano Letters*, 19(2):857–865, 2019.

[28] G Liu, B Debnath, T R Pope, T T Salguero, R K Lake, and A A Balandin. A charge-density-wave oscillator based on an integrated tantalum disulfide–boron nitride–graphene device operating at room temperature. *Nature Nanotechnology*, 11(10):845–850, 2016.

Chapter 6

Summary and Future Prospects

Surfaces play crucial roles in a great number of scientifically and technologically important fields, from friction, wear, corrosion; all the way to nanoscale electronic devices. To probe surface related physics or to study surface mediated processes, we need to have access to atomic-scale structure and properties of surfaces or in other words, to be able to image surfaces with atomic-level spatial resolution. The traditional techniques that are capable of direct, real-space surface imaging with true atomic resolution have some associated limitations. For example, they rely heavily on environmental conditions and are typically operated under UHV, also sometimes at low temperature which in turn makes these techniques expensive and exclusive. As such, not a lot of researchers have access to these tools. More importantly, studies performed under well controlled environments may not reveal relevant useful information for great number of processes that actually occur under ambient conditions. To fill this crucial gap, this thesis focused on true atomic-resolution imaging of surfaces under ambient conditions following the method C-AFM.

In Chapter 2, we demonstrated that C-AFM is capable of true atomic-resolution surface imaging under ambient conditions by resolving a single S vacancy on the MoS_2 surface. Subsequently, we gathered clues to understand the mechanism that enables C-AFM to image surfaces with atomic resolution. In particular, we found that scanning speed plays a crucial role such that atomic resolution is achieved only at high speeds. On the contrary, scanning load did not have an appreciable effect on imaging. Based on those clues, we hypothesized that during high-speed scanning the tip and the sample may be separated by a nanoscopic water layer (accumulated under ambient conditions) and tunneling may happen through this water layer. Alternatively, a discrepancy between the physical and electrical tip-sample contact areas can also explain the atomic-resolution C-AFM images. However, this hypothesis does not explain the speed and load dependence trends.

In Chapter 3, we demonstrated that high-speed C-AFM scanning is capable of imaging a variety of conductive material surfaces under ambient conditions. In par-

ticular, we reported atomic-resolution images for WSe_2, WS_2 as TMD semiconductors, BP as an elemental semiconductor, $PtSe_2$ as a TMD semimetal and finally Au as a closed-packed metal surface.

In Chapter 4, we employed the high-speed C-AFM methodology to study different types of defects on different types of material surfaces. Besides imaging defects on the top surface, we were also able to detect minute, atomic-scale disturbances in the subsurface. Going one-step further, we demonstrated the deliberate manipulation of charge states associated with defects on MoS_2.

Finally, in Chapter 5, we employed the high-speed C-AFM methodology to study a member of the emerging material class of MXene, namely thin crystals of α–Mo_2C. Along with studying the atomically-resolved crystal structure, we explored a panoply of defect structures on α–Mo_2C. Furthermore, we observed room-temperature charge ordering on the crystal surfaces.

A significant part of the results reported in this thesis have been recently published in the form of a journal article [1].

Looking forward, the work presented in this thesis provides multi-dimensional prospects for follow-up research. First of all, further studies need to be performed to definitively understand the mechanism behind the true atomic-resolution imaging capability of high-speed C-AFM. Within this context, humidity dependent imaging can provide important insights. On the other hand, the methodology presented here has huge potential to be employed in a variety of fields. Most importantly, it can be employed to study atomic-scale structure and properties of any conductive material surface, without the need for complicated vacuum equipment. It can additionally provide valuable inputs toward "defect engineering" by revealing the origin and role of a variety of defects and thus can help fine-tune/tailor the functionality of a given material surface. Our method has huge potential to be employed to study dynamic surface processes such as heterogeneous catalysis directly under ambient conditions. Perhaps most importantly, the method presented in this thesis will allow many researchers around the world to perform atomic-scale surface studies in a much less costly and straightforward fashion when compared with conventional surface science experiments.

6.1 References

[1] S A Sumaiya, J Liu, and M Z Baykara. True atomic-resolution surface imaging and manipulation under ambient conditions via conductive atomic force microscopy. *ACS Nano*, 2022.